Poster B

Ion and electron swarm studies of relevance to plasma processing: positive ion-molecule and electron-molecule studies of SF_6 and derivatives

Clair Atterbury,[a] Andrew D. J. Critchley,[b] Richard A. Kennedy[a] and Chris A. Mayhew[b]

[a]School of Chemical Sciences, [b]School of Physics and Astronomy, University of Birmingham, Edgbaston, Birmingham B15 2TT, UK

Many sequential and parallel chemical reactions involving charged species occur in a plasma. Data needed to model plasma's chemical and physical environment includes cross-sections, rate coefficients, and product ion distributions of electron-molecule and ion-molecule processes. Such reactions are studied by our group away from the complexity of the plasma environment, with experimental techniques that allow us to concentrate on a single process, where usually only one or two species are involved. A molecule commonly used in plasma etching applications is SF_6[1,2]. We have performed a series of positive ion-molecule and electron attachment studies on SF_6 and related molecules, including SeF_6, TeF_6 (*i.e.* XF_6 molecules), SF_5CF_3 and SF_5Cl (*i.e.* SF_5X molecules) [3-8]. The studies of ion reactions with and electron attachment to SF_6 and physically similar molecules are of value when seeking to understand the ion and electron chemistry occurring in SF_6 containing plasmas. The results of these studies are presented in this poster.

Ion-Molecule Reactions

Rate coefficients and ion product branching ratios have been determined with the Selected Ion Flow Tube (SIFT) at room temperature (300 K) for reactions of SF_5X with the following twenty-two cations; Ne^+, F^+, Ar^+, N_2^+, N^+, CO^+, CO_2^+, O^+, N_2O^+, H_2O^+, O_2^+, SF_4^+, CF_2^+, SF^+, SF_2^+, NO_2^+, SF_5^+, NO^+, CF^+, CF_3^+, SF_3^+, and H_3O^+ (listed in order of decreasing recombination energy). SF_2^+, NO_2^+, NO^+, SF_3^+, and H_3O^+ are found to be unreactive with both SF_5CF_3 and SF_5Cl. The majority of the other reactions proceed with rate coefficients that are close to the capture value. Those found to occur at rates significantly less than the capture mechanism value are the reactions of O_2^+, SF^+, SF_5^+, and CF_3^+ with SF_5CF_3, and SF_4^+ and SF_5^+ with SF_5Cl. Several distinct processes are observed among the large number of reactions studied, including dissociative charge transfer and various abstraction channels. Non-dissociative charge transfer is not observed, implying that the parent ion dissociates rapidly to the fragment ion and associated neutral(s). Figure 1 illustrates the reaction pathways accessible to the reagent ions either by dissociative charge transfer (simple fragmentation) and those involving migration of an F atom across the S-C bond.

Electron Attachment Studies

Electron attachment rate coefficients and anion product branching ratios have been measured for electron attachment to XF_6 (X = S, Se and Te) and SF_5X (X = Cl and CF_3), using an atmospheric pressure drift tube apparatus connected to a mass spectrometer. Results from these studies are presented. Electron attachment to XF_6 was observed to produce XF_6^- and XF_5^-. When extrapolated to zero attaching gas concentration, the branching ratios are found to be similar, with XF_6^- dominant in each case. Despite this similarity, the electron attachment rate coefficients are found to be markedly different: $k(SeF_6) \sim 10^{-2} \times k(SF_6)$; $k(TeF_6) \sim 10^{-3} \times k(SF_6)$. SF_5CF_3 and SF_5Cl are also found to attach electrons at a much slower rate than SF_6.

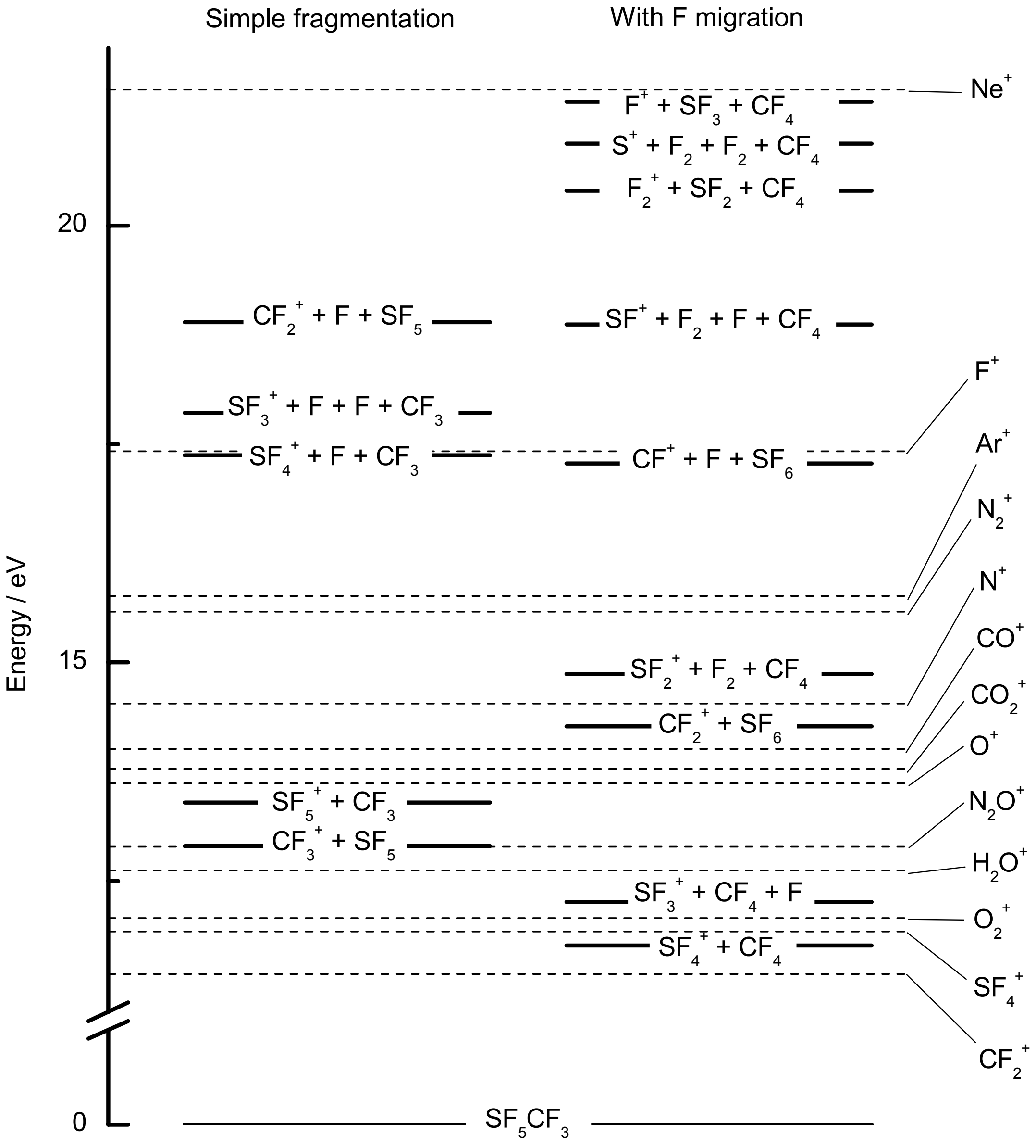

Figure 1. Adiabatic dissociative ionisation limits below 22 eV for SF_5CF_3. The limits are divided into those attained by simple fragmentation, and those involving the migration of an F atom across the S–C bond. The recombination energies of the reagent ions with *RE* > 11 eV are also presented in the figure. The electrons have been omitted from the labelling of the various limits.

Acknowledgements

We are grateful to the Technological Plasma Initiative Program, EPSRC, (Grant Reference: GR/L82083) for the financial support of this study. Miss Clair Atterbury thanks EPSRC for a research studentship.

References

---

[1] I. Sauers, L. G. Christophorou and S. M. Spyrou, "*Negative ion formation in compounds relevant to SF_6 decomposition in electrical discharges*" Plasma Chem.Plasma Processes **13** (1993) 17-35.

[2] H. X. Wan, J. H. Moore, J. K. Olthoff and R. J. Van Brunt, "*Electron scattering and dissociative attachment by SF_6*" Plasma Chem. Plasma Processes **13** (1993) 1-16.

[3] G. K. Jarvis, R. A. Kennedy and C. A. Mayhew, "Investigations of low energy electron attachment to ground state group 6B hexafluorides (SF_6, SeF_6, TeF_6)" Int. J. Mass Spectrom. **205** (2001) 253-270.

[4] R. A. Kennedy and C. A. Mayhew, “A study of low energy electron attachment to trifluoromethyl sulfur pentafluoride, SF_5CF_3, using an electron swarm mass spectrometric technique: atmospheric implications” Int. J. Mass Spectrom. **206** (2001) i-iv.

[5] C. Atterbury, R. A. Kennedy, C. A. Mayhew and R. P. Tuckett, “A study of the reactions of trifluoromethyl sulfur pentafluoride, SF_5CF_3, with several positive ions of atmospheric interest” Phys. Chem. Chem. Phys. **3** (2001) 1949-1953.

[6] R. A. Kennedy and C. A. Mayhew, “*Gas phase anion molecule chemistry of* SeF_6 *and* TeF_6” Phys. Chem. Chem.Phys. **3** (2001) 5511-5515.

[7] C. Atterbury, A. D. J. Critchley, R. A. Kennedy, C. A. Mayhew and R. P. Tuckett, “*A study of the gas phase reactions of various cations with two derivatives of* SF_6*;* SF_5CF_3 *and* SF_5Cl” Phys. Chem. Chem. Phys. (submitted November 2001)

[8] A. D. J. Critchley and C. A. Mayhew “*A study of low energy electron attachment to* SF_5CF_3 *and* SF_5Cl” (in preparation)

[9] R. Y. L. Chim, R. A. Kennedy, R. P. Tuckett, W. Zhou, G. K. Jarvis, D. J. Collins and P. A. Hatherly, “*Fragmentation of energy-selected* $SF_5CF_3^+$ *probed by threshold photoelectron photoion coincidence spectroscopy: Bond dissociation energy of* SF_5*-*CF_3 *and its atmospheric implications*” J. Phys. Chem. A **105** (2001) 8403-8412.

Charge Transfer in Ionic Systems

M.C. Bacchus-Montabonel[1], Y.S. Tergiman[1], N. Vaeck[2], E. Baloitcha[3] and M. Desouter-Lecomte[3,4]

1: Laboratoire de Spectrométrie Ionique et Moléculaire (UMR 5579 du CNRS) Université Lyon I, 43 Bd du 11 Novembre 1918, 69622 Villeurbane Cedex, France
2: Laboratoire de Chimie Physique Moléculaire, Université Libre de Bruxelles, CP 160/09, B-1050 Bruxelles
3: Laboratoire de Dynamique Moléculaire, Université de Liège, Institut de Chimie B6, Sart-Tilman, Liège 1, Belgique
4: Laboratoire de Chimie Théorique, Université Paris Sud, 91405 Orsay Cedex, France

Charge transfer involving multiply charged ions in collision with atomic or molecular targets are determinant processes in controlled thermonuclear fusion research and astrophysical plasmas. In such processes, an electron is generally captured in an excited state of the ion, followed by line emission. The observation of line intensities provides important information on the electron temperature, density and spacial distributions in the emitting region of the plasma.

From a theoretical point of view, different approaches may be used with regard to the collisional energy range of the process. A semi-classical method is currently used at keV energies, but the description of very low-velocity processes requires a complete quantum mechanical treatment of the dynamics of both electrons and nuclei. The first approach extensively used is the resolution of the stationary close-coupling equations, but we have analyzed recently the efficiency of a time-dependent wave packet method [1,2] which provides a clear and physical insight into the dynamics of the processes and may be particularly interesting for polyatomic systems since it allows the possibility of developing a fully quantal mechanical treatment for some degrees of freedom, the other ones being treated classically.

The keV energy range treatment is presented on two examples pointing out the case of complex ion-atom collision systems, as well as the differences between ion-atom and ion-molecule mechanisms. In connection with translation energy spectroscopy experiments of McLaughlin et al [3] in the 4-28 keV impact energy range, we present a complete ab-initio theoretical approach of the $N^{4+}(2s)^2S$ + He system taking into account both single and double electron capture channels [4]. This is an extremely complex collisional system which involves numerous collision channels with short range interactions and a very intricate interaction

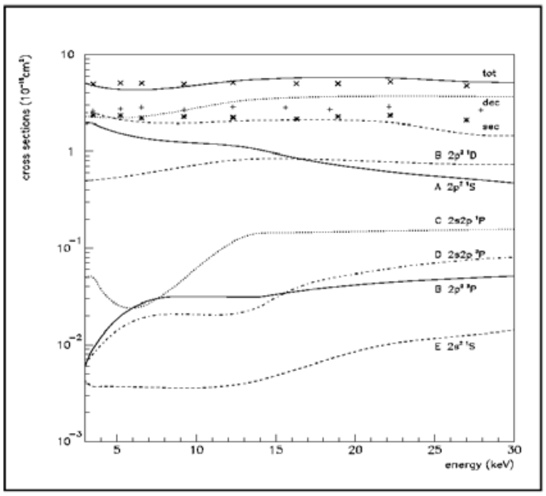

Adiabatic potential energy curves for N^{4+} + He
Full curves, $^2\Sigma^+$ states; broken curves, $^2\Pi$states.

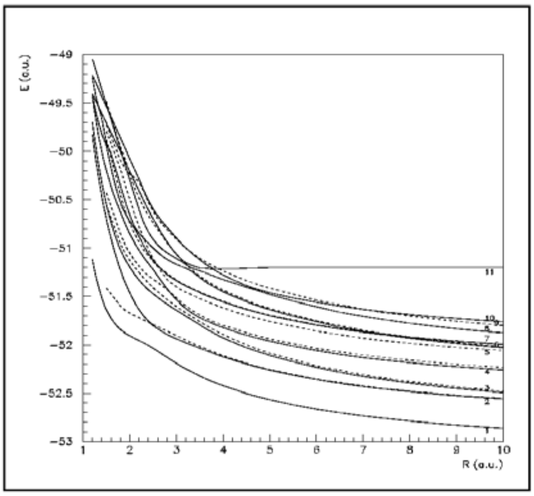

Cross sections for the N^{4+} + He process
Comparison with experimental data [3]

region may be observed for interatomic distances around R=3.5 a.u.. In agreement with experimental data, the process is shown to be dominant on the $N^{3+}(2p^2)^1S$ single capture channel, but the double capture process has to be taken into account in the mechanism.

The semi-classical approach may be extended to molecular targets, taking account of the much higher velocity of electronic transitions, with respect to molecular vibration. At the lower level of approximation, the molecular vibration of the molecule can be ignored and the ion-molecule collision may be visualized as an ion bumping an anisotropic atom. This approach has been applied on the $B^{3+}(1s^2) + H_2$ [5] and give reasonable results for energies greater than 100 eV/amu.[6], taking account of the anisotropy effect for the different orientations of the molecule and the dependence on the vibrational coordinate $r_{H\text{-}H}$.

The wave-packet time-dependent treatment has been developed on the Si^{4+} + He collisional system [1,2]. The recombination of silicon ions with atomic hydrogen and helium is a quite important process in astrophysical plasmas which has attracted recently a particular interest as experiments of Fang and Kwong [7] have provided for the first time measurements of rate constants at very low temperatures. The calculation has been performed in both adiabatic and diabatic representations in order to get rid of the ambiguity in defining the unitary transformation, in particular for polyatomic systems and Hanckel-Ricatti functions have been used in order to improve the precision of the calculations. Our results are in good agreement with time independent approaches [8], but a large discrepancy is observed with the ion-trap experiment of Kwong which cannot be explained by the simple electron exchange Si^{4+}/Si^{3+}. Further mechanisms involving impurities or excited states should perhaps be considered.

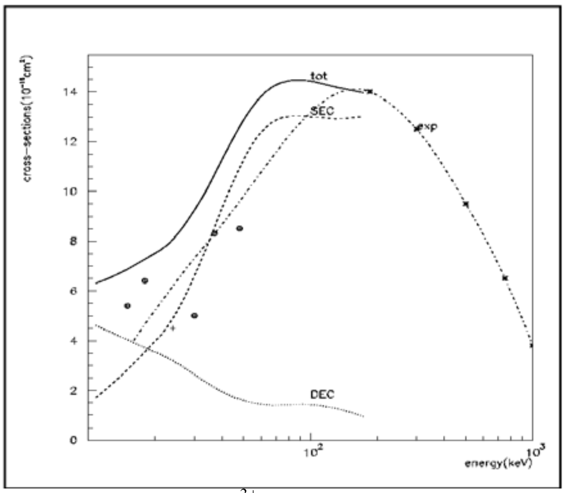

Cross sections for $B^{3+} + H_2$. Comparison with experimental data [6]

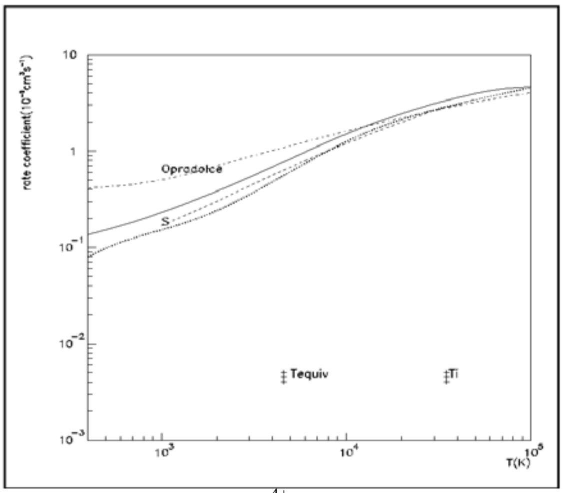

Rate coefficients for Si^{4+}+He (full curve, Hankel- Ricatti functions ; dotted curve, plane waves)

References

[1] N. Vaeck, M.C. Bacchus-Montabonel, E. Baloïtcha, M. Desouter-Lecomte, *Phys. Rev. A* **63**, 042704 (2001).

[2] E. Baloïtcha, M. Desouter-Lecomte, M.C. Bacchus-Montabonel, N. Vaeck, *J. Chem. Phys.* **114**, 8741 (2001).

[3] T.K. McLaughlin, H. Tanuma, J. Hodgkinson, R.W. McCullough, H.B. Gilbody, *J. Phys. B* **26**, 3871 (1993).

[4] Y.S. Tergiman, M.C. Bacchus-Montabonel, *Phys. Rev. A* **64**, 042721 (2001).

[5] M.C. Bacchus-Montabonel, *Phys. Rev. A* **59**, 3569 (1999).

[6] T.V. Goffe, M.B. Shah, H.B. Gilbody, *J. Phys. B* **12**, 3763 (1979) ; D.H. Crandall, R.A. Phaneuf, F.W. Meyer, *Phys. Rev. A* **19**, 504 (1979).

[7] Z. Fang and V.H.S. Kwong, *Phys. Rev. A* **59**, 342 (1999)
[8] P.C. Stancil, B. Zygelman, N.J. Clarke, D.L. Cooper, *Phys. Rev. A* **55**, 1064 (1997)

Correlation properties of surface and percolation transfer of electrons

O.G. Bakunin

Russian Research Center “Kurchatov Institute”,Moscow,Russia. Prokhor@nfi.kiae.ru

In this work was received equation, connecting correlativity properties of surface with electrons distribution function. Usually for equilibrium is necessary a large number of collisions. Collisions are “destroying” correlations. In case rare collisions large importance have correlations and “memory” effects. Non-Markov’s character of emitting particles by surface lead to strongly nonequilibrium condition of “gas” Here kinetic equation of diffusive form does not apply. Classical kinetic equation are described only conditions near to equilibrium.

This work offers to use ideas anomal diffusion in phase-space. The correlation properties of surface describe by correlations of velocities of emitting electrons: $B(t)$. We offer to use functional equation for probability collision instead of kinetic equation:

$$\int_{0}^{v<v_0} W_{noncoll.} F(v)\,dv = 1 - B(t)\,.$$

This functional allow to consider “memory” effects. It is important for consideration of electrons and clusters near surfaces. Distribution function become direct connected with correlations. In classical Kubo-Mory theory of transfer is necessary to get nondivergences integral: $D \propto \int_{0}^{\infty} B(t)$ .In considering case we can use even “power function”. It was used ‘slow’ correlation function as Kohlrausch in calculations. The information about kinetics and correlations properties are containing in one functional equation. It was received solution of this equation in form Levy function:

$$F(v) \propto \frac{1}{v^{\alpha}} \exp\left(-\frac{1}{v}\right).$$

The solution of this form can not to be get with help asymptotic methods of kinetic theory. Asymptotics of solution have scale-invariant character $F(V) \propto \frac{1}{V^{a}}$. This indicate on fractal properties phase-space.

Reactive intermediates of transition metals in water clusters

Martin K. Beyer, Brigitte S. Fox, O. Petru Balaj, Iulia Balteanu, and Vladimir E. Bondybey

Institut für Physikalische und Theoretische Chemie, Technische Universität München, Lichtenbergstraße 4,
85747 Garching, Germany
Email: martin.beyer@ch.tum.de

Metal ions in unusual oxidation states can be introduced into water clusters using a standard laser vaporization source. Such nanosolutions of a single ion in typically 50 water molecules are comparable to a one molar bulk solution, and their chemistry can be studied in the ion trap of a fourier-transform ion cyclotron resonance (FT-ICR) mass spectrometer. The laser vaporization usually yields singly charged hydrated transition metal ions $M^+(H_2O)_n$, corresponding to the oxidation state +I. Due to a rapid disproportionation, this oxidation state is for most transition metals unstable in bulk solution. In the cluster, however, with only a single metal ion present, this decay channel is closed, and the hydrated monocation is stable even on the long time scale of the ICR experiment. The +I oxidation state is a potential intermediate for redox reactions involving transition metals, and these clusters offer a unique opportunity to study these elusive species in an aqueous environment.

When exposed to room temperature black-body radiation, $M^+(H_2O)_n$ with M=Cr, Mn, Fe, Co, Ni, and Cu decay by sequential loss of water molecules, and no redox reactions are observed. Hydrated vanadium cations $V^+(H_2O)_n$, n=5-30, besides the loss of water ligands, show two different intracluster redox reactions, whose branching ratios are strongly size-dependent. Oxidation to the +II state results in $V(OH)^+(H_2O)_n$ ions, and a concurrent release of atomic hydrogen. Alternatively $V(OH)_2{}^+(H_2O)_n$ clusters can form, leaving vanadium in the +III state, common in aqueous solutions, and simultaneously molecular H_2 evaporates from the cluster. This behavior reflects the ability of vanadium as a transition metal to form stable compounds in a variety of oxidation states, and differs from the previously studied intracluster reactions involving the hydrated monovalent main group metals Mg^+ and Al^+ which only react to their preferred oxidation state, $MgOH^+$ and $Al(OH)_2{}^+$, respectively.

A strong acid like hydrogen chloride also oxidizes the early transition metal vanadium to the more common +III state, while Cr, Mn, Fe, Co, Ni, and Cu retain their unusual +I oxidation state, and the binary metal chlorides M(I)Cl precipitate.

Periodic Trends in the Gas-Phase Oxidation of $M(C_6H_6)_n^+$ Adduct Ions (n = 1,2) with Molecular Oxygen.

Doina Caraiman and Diethard K. Bohme

Department of Chemistry, Centre for Research in Mass Spectrometry and Centre for Research in Earth and Space Science, York University, Toronto, Ontario, Canada, M3J 1P3.

An Inductively-Coupled Plasma (ICP) has been interfaced with a Selected-Ion Flow Tube (SIFT) tandem mass spectrometer and this combination has been used in systematic measurements of periodic trends in reactivity for reactions of molecular oxygen with transition-metal cations both bare and attached to benzene.

The gas-phase oxidation of metal cation-benzene adducts in reactions with O_2 can mimic the oxidation of larger organometallic or biological molecules containing benzene units in the presence of metals. Transition metal cations often provide the active sites in such processes and can mediate oxidation reactions by binding molecular oxygen reversibly (O_2 transport by mioglobin) or by delivering an O-atom to various substrates (Cytochrome P-450).[1] To the extent that benzene mimics graphite, the oxidation of metal-coated graphite also can be simulated.

Experimental

Transition metal cations are produced in an ICP source,[2] selected with a quadrupole mass filter and injected upstream into a flow tube containing helium buffer gas at 0.35±0.01 Torr and 295±2 K. Benzene adduct ions are generated by adding benzene and thermalized by collisions with He upstream of the reaction region. Reactant O_2 is added midstream. Reactant and product ions are selected by a second quadrupole and detected downstream. Ion signal measurements are taken as a function of O_2 flow and these provide reaction rate coefficients and product ion distributions. Bond connectivities are determined by inducing collisional fragmentation prior to sampling.[3]

Results and Discussion

Kinetic results obtained for primary reactions of benzene mono-adducts of all transition metal cations (except Tc^+) with molecular oxygen are presented in Figure 1. They are presented as reaction efficiencies, k_{obs}/k_c, where k_{obs} is the measured reaction rate coefficient and k_c is the collision rate coefficient calculated using the Variational Transition State Theory.[4] Also included are branching ratios for competing primary reaction channels.

The primary channels observed are described by reactions (1a)-(1g). Some of these clearly involve O-O (reactions 1a and 1c), C-H (reaction 1c) or C-C (reaction 1f) bond activation. The relative occurrence of these reaction channels clearly depends on the position of the transition-metal cation in the periodic table, viz. the electronic structure of the metal cation.

$MC_6H_6^+ + O_2$	$\rightarrow MC_6H_6O^+ + O$	O-atom transfer	(1a)
	$\rightarrow MC_6H_6O_2^+$	addition	(1b)
	$\rightarrow MC_6H_4O^+ + H_2O$	addition/dehydration	(1c)
	$\rightarrow C_6H_6^+ + MO_2$	metal abstraction	(1d)
	$\rightarrow MO_2^+ + C_6H_6$	ligand switching	(1e)
	$\rightarrow MC_4H_4^+ + (C_2H_2O_2)$	acetylene elimination	(1f)
	$\rightarrow M^+ + (C_6H_6O_2)$	benzene abstraction	(1g)

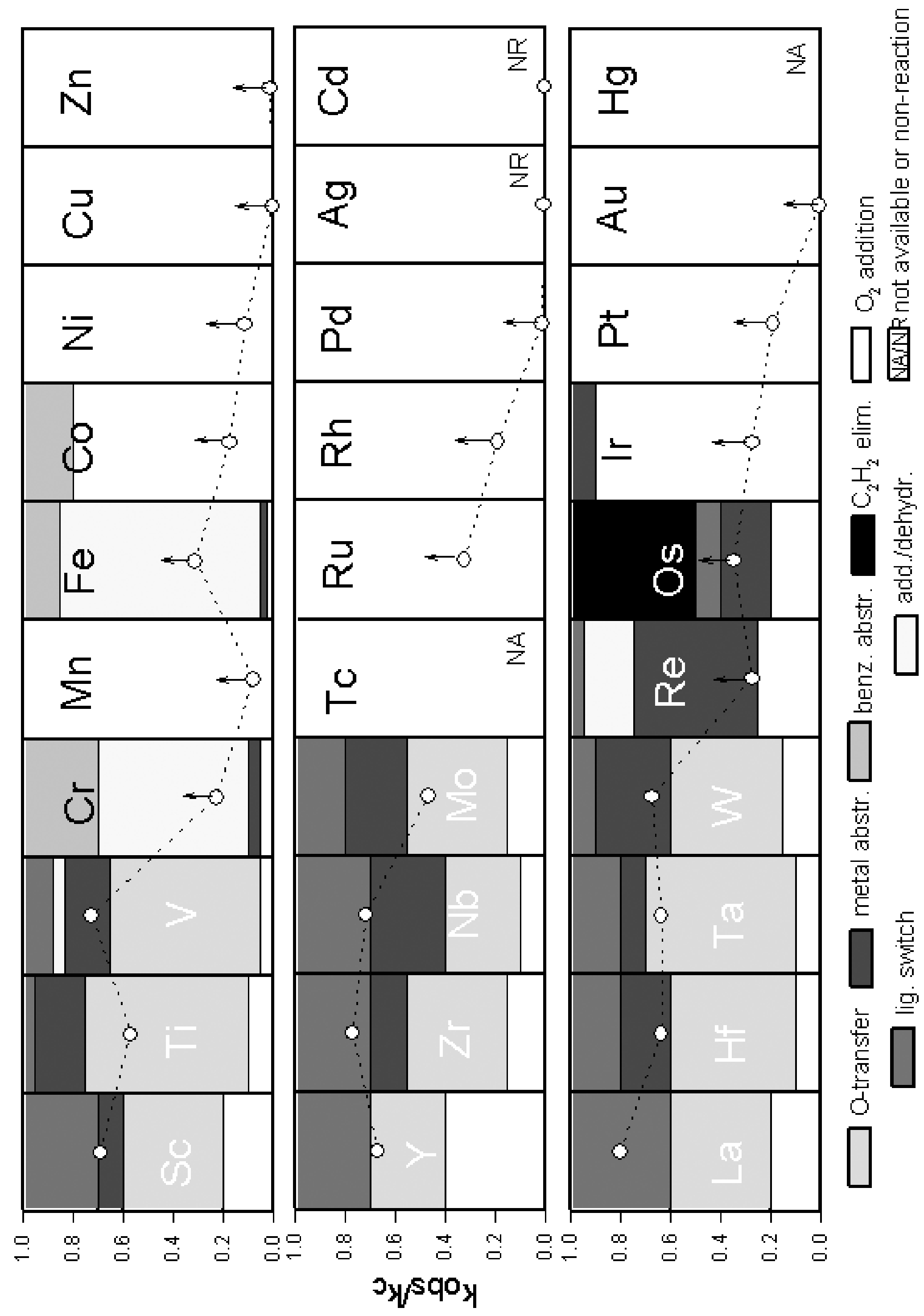

Figure1. Periodic variations in the reactivity of transition metal cation-benzene mono-adducts toward molecular oxygen, k_{obs}/kc, where k_{obs} is the measured rate coefficient and k_c is the calculated collision rate coefficient. The observed reaction channels are also indicated with their measured branching ratios.

Benzene adducts of early transition-metal cations exhibit rich chemistry that involves competition between several (up to five) reaction channels. The overall reactions are fast, approaching the collision limit, $k_{obs} > 2.6\text{x}10^{-10}$ $\text{cm}^3\text{molecule}^{-1}\text{s}^{-1}$. In sharp contrast, late transition-metal cations simply add molecular oxygen and do so slowly, $k_{obs} < 1.8\text{x}10^{-10}$ $\text{cm}^3\text{molecule}^{-1}\text{s}^{-1}$, or they do not react measurably in the flow range investigated, $k_{obs} < 1.6$ $\text{x}10^{-12}$ $\text{cm}^3\text{molecule}^{-1}\text{s}^{-1}$ (Ag, Cd). Some intermediate transition-metal cations react slowly but still exhibit several primary reaction channels. Hg^+ does not form an adduct with benzene, rather it abstracts an electron.

Figure 1 clearly shows that metal-benzene adduct ions of early transition metals activate molecular oxygen and accept an O atom in a manner that we have previously established for bare transition-metal ions (in the absence of benzene).[5] Also we have found that $M(C_6H_6)_2^+$ ions do not accept an O atom and that O-atom transfer (with unit reaction efficiency) occurs as a secondary reaction, reaction (2), for M = Nb, Mo, Ta and W.

$$MC_6H_6O^+ + O_2 \rightarrow MC_6H_6OO^+ + O \qquad (2)$$

Molecular oxygen addition, reaction 1b, occurs with most metal-benzene mono-adducts, in contrast with what is observed in the absence of the benzene ligand.[5] Molecular oxygen addition is the exclusive reaction pathway for benzene adducts of late transition metal cations; rate enhancement of up to one order of magnitude is observed when benzene is added to these cations. Addition of molecular oxygen is also observed in reactions of benzene bis-adducts with early transition metal cations (Sc^+, Y^+, La^+, Zr^+, Hf^+, Nb^+ and Ta^+). Reaction rate coefficients for these addition reactions range from 1.7×10^{-12} $cm^3 molecule^{-1} s^{-1}$ for $Ta(C_6H_6)_2^+$ to 3.4×10^{-10} $cm^3 molecule^{-1} s^{-1}$ for $La(C_6H_6)_2^+$. Only one benzene bis-adduct of late transition metal cations, $Zn(C_6H_6)_2^+$, was observed to react with oxygen by addition, $k_{obs} = 4.1 \times 10^{-11}$ $cm^3 molecule^{-1} s^{-1}$. O_2 addition was also observed to occur with monoxides formed in reaction (1a). $TiC_6H_6O^+$, $VC_6H_6O^+$, $ZrC_6H_6O^+$ and $HfC_6H_6O^+$ reacted relatively fast by adding one molecule of O_2, $k_{obs} > 7.9 \times 10^{-11}$ $cm^3 molecule^{-1} s^{-1}$.

The dehydration channel (1c) occurs with V^+, Cr^+, Fe^+ and Re^+ (with Cr^+ and Fe^+ it is the major channel)) and involves O-O and C-H activation. The product ions $CrC_6H_4O^+$ and $FeC_6H_4O^+$ behaved differently upon collisional dissociation and structures have been assigned accordingly.

Reactions in which the metal is abstracted, reaction (1d), or in which the benzene ligand switches with molecular oxygen, reaction (1e), result in the formation of neutral or cationic transition-metal dioxides. Metal abstraction was observed for M = Sc, Ti, V, Zr, Nb, Mo, Hf, Ta, W, Re, Os, and Ir. Switching was observed for M = Sc, Ti, V, Y, Zr, Nb, Mo, La, Hf, Ta, W, Re and Os. The occurrence or non-occurrence of these channels allows estimations to be made of thermochemical properties of the metal dioxide species.

The benzene abstraction channel (1g) was observed with Cr^+, Fe^+ and Co^+. Formation of the neutral product molecule catechol (1,2-dihydroxybenzene) provides the highest reaction exothermicity.

The product metal ion can reattach to benzene and so initiate a catalytic cycle that results in the oxidation of benzene to catechol.

The acetylene elimination channel (1f) is unique to Os^+ and clearly involves benzene ring cleavage.

Acknowledgements

Continued financial support from the Natural Sciences and Engineering Research Council of Canada is greatly appreciated. Also, we acknowledge support from the National Research Council, the Natural Science and Engineering Research Council and MDS SCIEX in the form of a Research Partnership grant.

References

---

[1] Ho, R.Y. N.; Liebman, J.F. and Valentine, J.S. in *Active Oxygen in Biochemistry*, Blackie Academic & Professional, Glasgow 1992, 1-37.

[2] Koyanagi, G.K.; Lavrov, V.V.; Baranov, V.I.; Bandura, D.; Tanner, S.D.; McLaren, J.W.; Bohme, D.K. *Int. J. Mass Spectrom.* **2000**, *194*, L1.

[3] Baranov, V.; Bohme, D.K. *Int. J. Mass Spectrom. Ion Processes* **1996**, *154*, 71-88.

[4] Su, T.; Chesnavich, J. *J. Chem. Phys.* **1982**, *76*, 5183-5185.

[5] Koyanagi, G.K., Caraiman, D., Blagojevic, V. and Bohme, D.K., *J. Phys. Chem.*, submitted.

Reactive scattering of carbon atoms:
The reaction dynamics of $C(^3P, ^1D) + C_2H_2$ and C_2H_4

P. Casavecchia, G. Capozza, L. Cartechini, A. Bergeat, and G.G. Volpi

Dipartimento di Chimica, Università di Perugia, 06123 Perugia, Italy

Abstract

The reaction dynamics of $C(^3P,^1D)$ with acetylene and ethylene have been investigated by using the crossed beam technique with mass spectrometric detection and time-of-flight (TOF) analysis. The novel capability of generating continuous supersonic beams of carbon atoms by a radio-frequency discharge beam source is exploited. From angular and velocity distribution measurements, the primary reaction products are identified, their relative importance assessed, and their dynamics of formation characterized. While the reaction $C(^3P) + C_2H_2(X^1\Sigma_g^+)$ has been found to lead to $C_3H + H$ and $C_3(X^1\Sigma_g^+) + H_2(X^1\Sigma_g^+)$ in comparable amount, the reaction $C(^3P) + C_2H_4(X^1A_1)$ has been found to lead, predominantly, to $H + C_3H_3$ (propargylene). The dynamics of the $C(^1D)$ reactions are also characterized. The spin-forbidden H_2 elimination channel in the reaction $C(^3P) + C_2H_2$ is attributed to the occurrence of inter-system-crossing between the triplet and singlet manifolds of the C_3H_2 potential energy surfaces. Interestingly, these findings provide evidence that the $C(^3P) + C_2H_2$ reaction maybe the source of both C_3H and C_3species detected in the extreme environments of dense interstellar clouds and outflows of carbon stars, as well as in combustion systems.

Introduction

In this contribution we report on the investigation of the dynamics of some important reactions of $C(^3P,^1D)$ with unsaturated hydrocarbons (acetylene, ethylene), a work carried out in asynergistic fashion with low temperature kinetic[1]and low energy dynamic (integral cross sections)[2]experiments within the EC Network on Astrophysical Chemistry.[3]These reactions are of basic chemical interest and of great relevance in areas which range from combustion to astrochemistry. Kinetic studies of a variety of $C(^3P)$ reactions with unsaturated hydrocarbons(C_2H_2, C_2H_4, C_3H_4, etc.) found them very fast ($k \approx 2\text{-}4\times10^{-10}$ cm^3 molecule^{-1}s^{-1}) down to very low temperature (15 K) and suggested that these are barrierless reactions dominated by long range attractive forces and that may have a critical role in the chemistry of the inter-stellar-medium (ISM).[1]These studies, however, follow the decay of $C(^3P)$and do not provide information on the primary products and on the dynamics of the reaction.

In our laboratory, we have carried out measurements of product angular and velocity distributions at different mass-to-charge (*m/e*) ratios by using the crossed beamtechnique,[4] and from this we have identified the primary products and determined their branching ratios for both $C(^3P)$ and $C(^1D)$ title reactions, have derived their angular and translational energy distributions in the Center-of-Mass (CM) frame, and have characterized the reaction micromechanism. The reaction dynamics are discussed in the light of recent theoretical calculations on the relevant potential energy surfaces (PESs) governing the transformation from reactants to products.[3,5-7]

Experimental

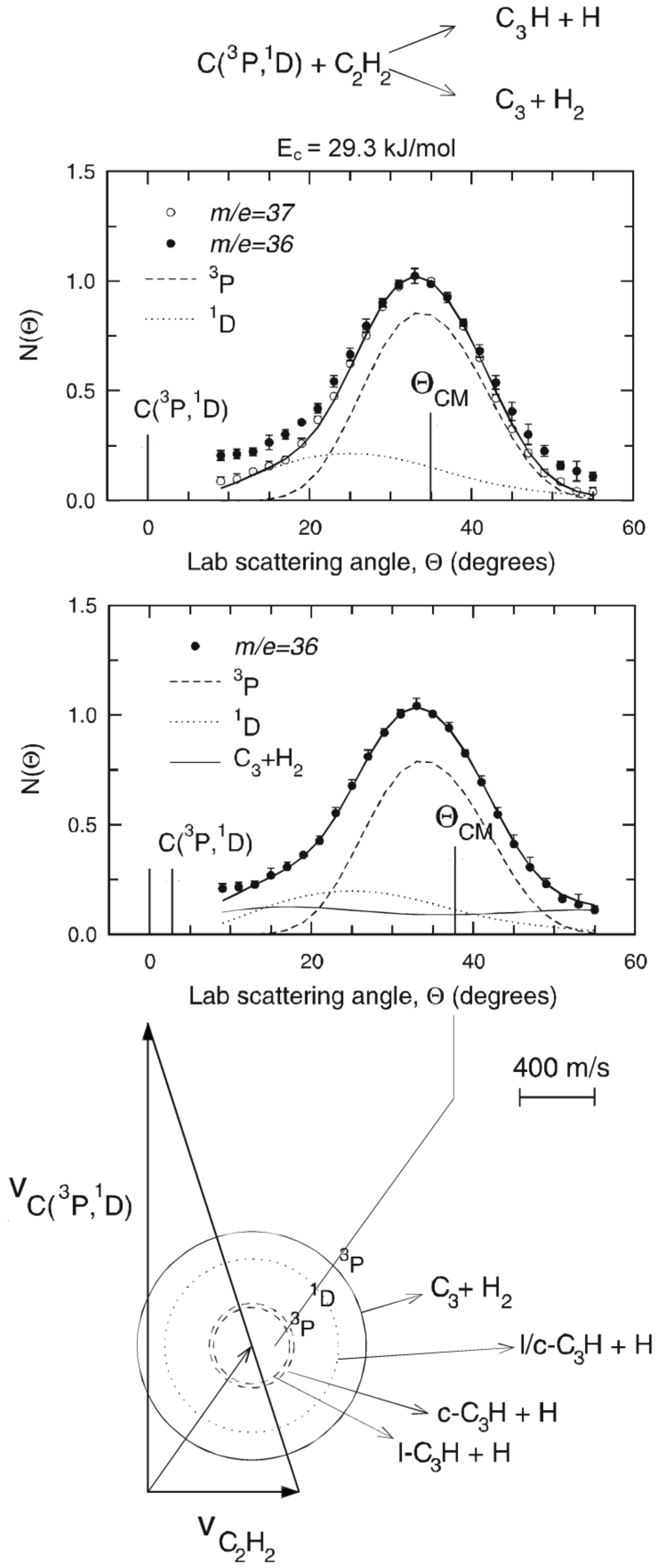

Fig. 1 Lab product angular distributions at *m/e*=37 and 36for the C+C_2H_2 reaction with Newton diagram of the experiment(see text). The circles delimit the maximum velocity that the various products can attain on the basis of momentum and energy conservation.

Supersonic, *continuous* beams of carbon atoms, generated by a high pressure RF discharge beam source in diluteCO_2/rare gas mixtures, well collimated in angle and velocity, are crossed at 90° with supersonic beams of C_2H_2 and C_2H_4 in a large scattering chamber.[5] The reaction products are detected by a rotatable UHV mass spectrometer detector with electron impact ionizer; the product velocities are measured by the pseudo-random TOF technique.[4,5] The C beams contain only 2-3% C_2 and no detectable C_3; this characteristic is particularly important in this study, since C_3 is one of the energetically allowed products of the C+C_2H_2 reaction.

Results

The reaction $C(^3P,^1D) + C_2H_2(X^1\Sigma_g^+)$ was studied at the collision energy E_c of 29.3 kJ/mol by detecting the products at *m/e*=37 and 36. The corresponding lab angular distributions are depicted in Fig. 1 together with the velocity vector ("Newton") diagram of the experiment. The relevant dynamic information, i.e., the double differential cross section $I_{CM}(\theta,E)$, was retrieved using a forward convolution fit of the lab distributions by assuming a separable CM angular, $T(\theta)$, and translational energy, $P(E'_T)$, distributions, i.e., $I_{CM}(\theta,E)=T(\theta)\times P(E'_T)$. The*m/e*=37 data correspond to formation of C_3H + H products and revealed contribution from both the $C(^3P)$ and $C(^1D)$reactions (see best-fit curves in Fig. 1-top). It can be seen that the*m/e*=36 angular distribution is wider and extends on a wider range of lab angles,Θ, than the one at *m/e*=37 (also, the TOF spectra, not shown here, exhibit a faster rising edge). This unambiguosly indicates that the *m/e*=36 signal does not originate only from dissociative ionization of C_3H in the ionizer, but it must also arise from an H_2 elimination channel, corresponding to C_3 + H_2formation (see best-fit in Fig. 1-bottom). From the extent of the $P(E'_T)$ distribution we concluded that C_3 formation arises only from the $C(^3P)$ reaction.[5,6] We have derived a ratio of integral cross sections $\sigma(C_3+H_2)/[\ \sigma(C_3+H_2)+\ \sigma(C_3H+H)]$ of about 0.37; that is, the H_2 elimination channel is comparable in importance to the H elimination channel.[5,6]

The reaction C + C_2H_4 was studied at four different E_c (8.8,15.9, 29.7, and 37.8 kJ/mol) by detecting products at *m/e*=39 and 38. The corresponding angular and TOF distributions were found to be identical, indicating that the C/H exchange channel is the dominant pathway and no H_2 formation occurs.[5,7]

Discussion

Both reactions, $C(^3P,^1D) + C_2H_2$ and C_2H_4 are found to proceed through a strongly bound intermediate (C_3H_2 and C_3H_4, respectively) that lives a time comparable to its rotational period. Formation of H + H_2CCCH (propargyl) is the dominant pathway, at low collision energy (E_c), of the $C(^3P,^1D) + C_2H_4$reaction, while at high E_c formation of the less stable C_3H_3 isomers (cyclopropenyl and/or propyn-1-yl) also occurs; the H_2 elimination channel is negligible and no $C(^1D)$ contribution has been observed except at high E_c.[5,7] The H elimination channel has also been found to be the dominant pathway in the $C(^3P,^1D)$ + CH_3CCH reaction leading toC_4H_3 isomers (both the triplet and singlet dynamics has been characterized); again, no H_2elimination was observed to occur.[5]

In contrast, both H and H_2elimination, leading in comparable ratio to C_3H + Hand $C_3(X^1\Sigma_g^+)$ +$H_2(X^1\Sigma_g^+)$, respectively, have been observed in the reaction $C(^3P) + C_2H_2(X^1\Sigma_g^+)$ at a collision energy of E_c=29.3 kJ/mol. The dynamics of C_3H + H formation from $C(^1D)$ has also beencharacterized.[3,5,6] The occurrence of the spin-forbidden molecular pathway in the $C(^3P) + C_2H_2$ reaction, never detected before,[8] has been rationalized by invoking the occurrence of inter-system-crossing between triplet and singlet manifolds of the C_3H_2 PESs (see Fig. 2). These findings are supported by recent kinetic work[9] as well as by theoreticalcalculations[10] and may have important consequences in establishing the role of this reaction in the modeling of combustion and interstellar chemistry networks.

The detailed results will be discussed at the meeting.

Acknowledgments

We acknowledge financial support from the Italian MURST (COFIN) and the EC TMR Research Network grant on Astrophysical Chemistry (contractFMRX-CT97-0132 (DG12-MIHT)), including post-doctoral fellowships for AB.

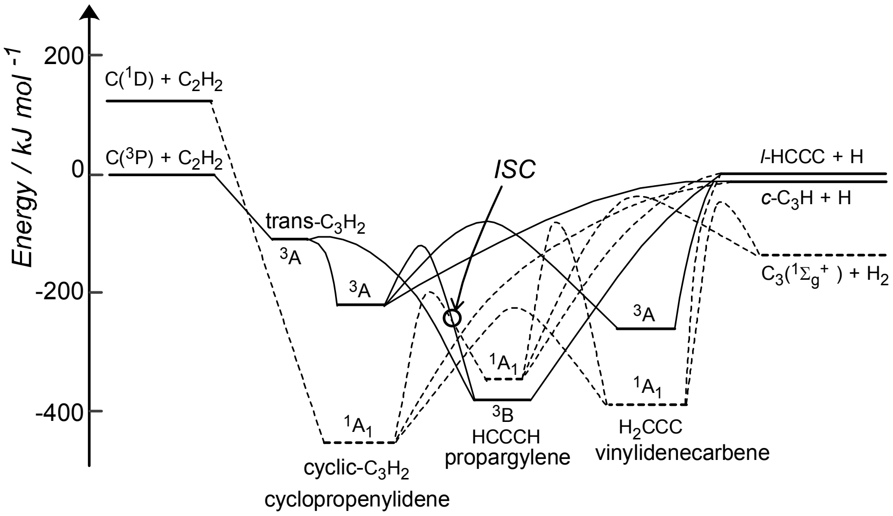

Fig. 2. Schematic representation of the triplet and singlet C_3H_2 potential energy surfaces, adapted from theoreticalcalculations (see Ref. 5). The triplet-singlet seam of crossing is labeledwith *ISC*.

References

[1] D. Chastaing, S. D. Le Picard, I.R. Sims and I.W.M. Smith, *A&A* **2001**, *365*, 241.

[2] D. Chastaing, S. D. Le Picard, I.R. Sims, I.W.M. Smith, W.D. Geppert, C. Naulin,M. Costes, *Chem. Phys. Lett.* **2000**, *331*, 170.

[3] D. C. Clary, E. Buonomo, I.R. Sims, I.W.M. Smith, W.D. Geppert, C. Naulin, M.Costes, L. Cartechini, P. Casavecchia, *J. Phys. Chem. A* (FeatureArticle) (**2002**), submitted.

[4] P. Casavecchia, *Reports on Progress in Physics* (**2000**), *63*, 355.

[5] P. Casavecchia, N. Balucani, L. Cartechini, G. Capozza, A. Bergeat, G.G. Volpi, *Faraday Discuss.* **2001**, *119*, 27, andreferences therein.

[6] L. Cartechini, A. Bergeat, G. Capozza, P. Casavecchia, G. G. Volpi, W.D. Geppert, C. Naulin,M. Costes, *J. Chem. Phys.* (submitted).

[7] G. Capozza,L. Cartechini, P. Casavecchia, G. G. Volpi, W.D. Geppert, C. Naulin,M. Costes, *J. Chem. Phys.* (to be submitted).

[8] R. I. Kaiser, C. Ochsenfeld, M. Head-Gordon, Y. T. Lee, and A. G. Suits, *J. Chem. Phys.* **1997**, *106*, 1729.

[9] A.Bergeat and J.-C. Loison, *Phys. Chem. Chem. Phys.* **2001**, *3*, 2038.

[10] A.M. Mebel, W.M. Jackson, A.H.H.Chang, S.H. Lin, *J. Am. Chem. Soc.***1998**, *120*, 5751.

Dissociative Electron Attachment to Ozone: Rate Constant

P. Cicman[1,2], J.D. Skalny[1] and T.D. Märk[1,2]

[1]*Department of Plasma Physics, Comenius University, Mlynska dolina F-2, 84248 Bratislava, Slovak Republic*
[2]*Institut für Ionenphysik der Leopold Franzens Universität,Technikerstrasse 25, A-6020 Innsbruck, Austria*

Abstract:

The rate constant for dissociative electron attachment to ozone has been derived over the energy range of 0-10 eV by using previously measured cross section data revisited here in regards to discrimination effect occurring during the extraction of ions. The obtained data for both possible channels exhibit the maximum at mean electron energies close to 1 eV.

Introduction

The attachment of electrons to molecules is an important process in discharge plasma, as it substantially affects the concentration of electrons and therefore the macroscopic properties of the plasma. Moreover, if the capture of an electron by an electronegative molecule proceeds via the dissociative channel this can actively affect the kinetics of plasmachemical and ion-molecule reactions in the gas discharge gap and therefore influence the equilibrium in the concentration of chemical compounds. Both the neutral molecular components of gaseous mixtures as well as the molecular products formed due to plasmachemical reactions can be dissociated. Hence the dissociative electron attachment is an additional process to direct electron impact dissociation of neutral gas components, which can play an important role in many industrial plasma technologies.

The dissociative electron attachment to ozone molecules in ozonisers is a typical example of such a process. Ozone, which is generated in the discharge gap can by destroyed by electron impact either directly [1]

$$e + O_3 \rightarrow O + O_2 + e \tag{1}$$

or via two competitive dissociative electron attachment processes

$$e + O_3 \rightarrow O^- + O_2 \tag{2}$$

$$e + O_3 \rightarrow O + O_2^- \tag{3}$$

The cross section for (2) exhibits a maximum in the range of 1.2 – 1.5 eV according to several studies [2]-[8]. The maximum for process (3) was observed at electron energies slightly below that corresponding to process (2). In addition, the existence of a very narrow resonance for process (2) at nearly zero electron energy has been reported recently [7] and [8]. This resonance was observed only if an electron beam of very low FWHM values was used in crossed-beams experiment. Moreover two further resonances in cross section data at 3.5 eV and 7.4 eV have been reported recently [2] and [3].

Despite of the importance of the dissociative process (2) and (3) in ozonisers, there are only several experimental studies reporting rate constants for these processes. Those, conducted over the period 1967-75, were surveyed by Caledonia [9]. Low values of the thermal rate constant at near zero electron energy, smaller than 1×10^{-11} cm^3s^{-1}, are typical for all earlier swarm data [9]. According to Stelman et al.[10] the rate constant k increases with the electron energy $\varepsilon_k = k_B T_e$ (k_B is Boltzmann constant and T_e is the electron temperature) expressed in eV as follows

$$k = 1.9\times10^{-9}(\varepsilon_k)^{1.46} \tag{4}$$

Formula (4) was used by Kastelewitz et al. [11] for low energy electrons $\varepsilon_k < 0.5$ eV. At higher energies the rate constant was derived from Currans relative cross section data [3], and then were normalised to Stelman's data. A Maxwell-Boltzman electron energy distribution function was used for these calculation yielding

$$k = 5.87 \times 10^{-9} \left(\varepsilon_k\right)^{-1.5} . \exp\left[-1.59/\varepsilon_k\right] \qquad (5)$$

which exhibits a flat maximum of 1.2 x 10^{-9} $cm^3.s^{-1}$ at a mean electron energy close to 1.5 eV. As to the author's knowledge there existed no new data for this rate constant.

In contrast to these values for the attachment rate constant determined by swarm experiments several papers report values of k higher that 1 x 10^{-9} cm^3s^{-1} using low temperature gas discharge plasmas [12, 13, 14]. Also from the attachment rate coefficient data obtained in oxygen-ozone [15] and air-ozone [16] mixtures in drift tubes higher values for the rate constant can be surmised. Finally, the modelling of ozone generation in a negative corona discharge has shown that the dissociative attachment processes (2) and (3) participate in the mechanism of ozone destruction [17]. There is however one contradictory data reported by Klopovskij et al. [18] who found a value of 5×10^{-10} cm^3s^{-1}, which does not depend on the electron energy.

In the current paper new attachment rate constant data are reported in the electron energy range (0 –10) eV.

Analysis of the extraction efficiency of a TEM and results.

The rate constant for the dissociative electron attachment has been calculated both for process (2) and (3) by using the earlier measured cross-section data [6] and [7]. Those were revisited in respect to the discrimination effect that occur during the extraction of ions from the collision region.

The operation of the TEM (Trochoidal Electron Monochromator [19]) at high energy resolution regime requires the extraction electric field in the collision chamber to be very small in order to minimise electric field effects on the electron energy distribution in the incidental electron beam. The beam is characterised by the full-width-half-maximum (FWHM). Under such conditions, the efficiency for the extraction of ions having higher kinetic energy is reduced. Therefore the experimentally measured yield of ions per time unit is not proportional to the rate of the ion formation in the collision region. Hence there is no direct proportionality between the measured yield and the cross section data, which is usually assumed to be valid converting the relative cross section data to absolute values [20]. Better to say, the shape of ion yield measured as a function of electron energy does not correspond to the real shape of the attachment cross section as a function of electron energy. The problem has been discussed in detail recently [21].

In order to avoid effects of the discrimination on the shape of the measured ion yield the extraction efficiency for ions has to be taken into account. Therefore this effect has been calculated by the program SIMION for the geometry of the TEM used in earlier experiments [6] and [7]. The calculated extraction efficiency for both O^- and O_2^- ions is shown in Fig. 1a, and 1b respectively.

The extraction efficiency is at its maximum (100%) when the high extraction electric field (extraction potential of 10 V) is applied only for ions having kinetic energies smaller than about 0.4 eV. At higher ion energies the efficiency is strongly reduced down to about 20%. In the case of low extraction electric field (extraction potential below 1 V) only a small fraction of ions having low energy is extracted completely. All other ions are strongly discriminated and the efficiency sharply decreases down to 20 % of maximum.

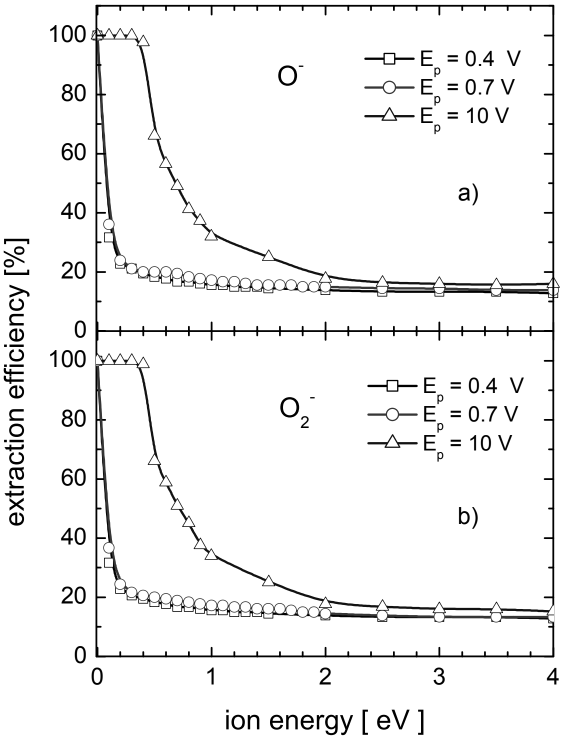

Figure 1

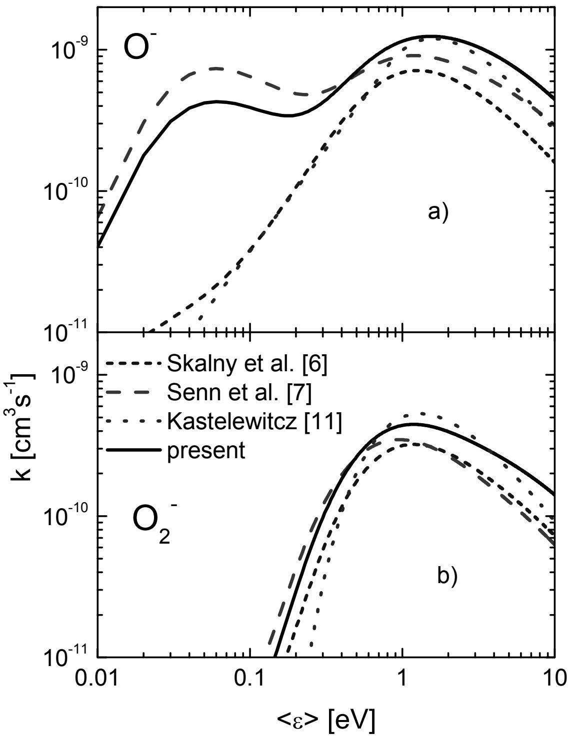

Figure 2

The earlier published absolute cross section data [6] and [7] were revisited by using this calculated extraction efficiency, assuming that the excess of the kinetic electron is transferred to the negative ion product. Absolute calibration of the corrected relative cross sections has been carried out by calibrating our O^- data at 1.3 eV (resonance maximum) to the O^- cross section values of Rangwalla et al. [2] at the same position. Knowing the absolute cross section values $\sigma(\varepsilon)$, a rate constant for the processes (2) and (3) was then calculated using the formula

$$k_{th} = \sqrt{\frac{8}{\pi m_e}} \int_0^{\infty} \sigma(\varepsilon)\varepsilon_k^{-3/2}\varepsilon.\exp\left[-\varepsilon/\varepsilon_k\right]d\varepsilon \qquad (6)$$

where m_e is an electron mass, $\varepsilon_k = 2/3 <\varepsilon>$ and $<\varepsilon>$ is the mean electron energy.

The calculated values of k as a function of the mean electron energy both for process (2) and (3) are plotted in Fig. 2a) and 2b) respectively together with the data determined from the original cross section data published earlier [6, 7]. For the comparison also the data reported by Kastelewitz and Bachman [11] are displayed.

The current data are evidently shifted in comparison to the earlier data and are in good agreement with that obtained from parameters of various discharges [12, 13, 14]. Moreover the current data are fairly well consistent with those determined by Kastelewitz and Bachman at electron energies above 1 eV by using the formula (4), and (5) [11]. At lower energies the differences between current data and earlier calculated are evident. The results confirm the fact that dissociative electron attachment to ozone under certain conditions typical for low temperature gas discharges (mean energy close to 1 eV) is a process which considerably contributes to mechanism of the ozone decomposition by an electron impact and must be considered, besides the direct electron impact dissociation (1), in the kinetic models of ozone formation by electrical discharges.

Acknowledgements

This work was partially supported by the FWF, Wien and the European Commision, Brussels. The author JDS is obliged also to Slovak Grant Agency Vega 2 under the project 1/765920 and NATO grant PST.CLG. 976544 for collaborative research.

References

[1] M. Kuzumoto, J. Kitayama, Y. Tabata, in Proceed. of 13th Ozone World Congress, Vol. 2, (Kyoto, Japan, 1997), pp. 815.
[2] S.A. Rangwala, S.V.K. Kumar, E. Krishnakumar, N.J. Mason, *J. Phys. B: At. Mol. Opt. Phys.* **32** (1999) 3795.
[3] I.C. Walker, J.M. Gingell, N.J. Mason, G. Marston: *J. Phys. B: At. Mol. Opt. Phys.* **29** (1996) 4749.
[4] R.K. Curran, *J. Chem. Phys.* **35** (1961) 1849.
[5] K.S Klopovskii, N.A. Popov, O.V. Proshina, A.T. Rakhimov, T.V. Rakhimova, *Plasma Physics Reports* **23** (1997) 165.
[6] J.D. Skalny, S. Matejcik, A. Kiendler, A. Stamatovic, T.D. Märk, *Chem. Phys. Lett.* **255** (1996) 112.
[7] G. Senn, J.D. Skalny, A. Stamatovic, N.J. Mason, P. Scheier, T.D. Märk, *Phys. Rev. Lett.* **82** (1999) 5028.
[8] G. Senn, H. Drexel, N.J. Mason , J.D. Skalny, A. Stamatovic, , P. Scheier, T.D. Märk, in CP 500, The Physics of Electronic and Atomic Collisions, (edit. Y. Itikava, Am. Inst. of Physics, New York 2000), pp.131.
[9] G.E. Caledonia, *Chem. Rev.* **75** (1975) 333.
[10] D. Stelman, J.L. Moruzzi, A.V. Phelps, *J. Chem. Phys.* **56** (1972) 4183.
[11] H. Kastelewitz, P. Bachman, preprint 78-10 Akademie der Wissenschaften der DDR (zentralinistitu für Elekroneprhysik, 1978), see also Ref. In E. Eliason, Brown Boweri Forschungsbericht N^{o} KLR 83-40C, 1985.
[12] V.I. Gibalov, A.B. Pravdin, M. Wronski, in Proceed. of HAKONE II (Intrnational Symposium on High Pressure and Low Temperature Plasma Chemistry), Kazimierz nad Wisla, Poland(edit. Technical Univerity, Lublin, 1989), pp. 68.
[13] L.E. Khvorostovskaya, V.A. Yankovsky, *Contrib. Plasma Phys.* **31** (1991) 71.
[14] J. Rahel, M. Pavlik, L. Holubcik, V. Sobek, J.D. Skalny, *Contrib. Plasma Phys.* **39** (1999) 502.
[15] S. Kajita, S. Ushiroda, Y. Kondo, in Proceed. of 21st ICPIG (Beograd, Yugoslavia, 1989), Vol. 4 pp.662.
[16] Y. Kondo, S. Kajita, S. Ushiroda, in Proceed. of The Third Workshop on Radiation Detectors and Their Use (Ibaraki, Japan, 1988) pp. 64.
[17] F. Pontiga, C. Soria, A. Castellanos, J.D. Skalny, in Proceed. of 15th Ozone World Congress (Edit. S.D. Lambert, Imperial College of London, London, UK, 2001) pp. 30.
[18] K.S. Klopovskij, A.A. Nechaev, A.P. Osipov, I.G. Periancev, V.M. Polushin, T.V Rachimova, N.V. Suetin, M.A. Timofeev, *Chimia Vysokich Energii* **19** (1985) 379.
[19] A. Stamatovic, G.J. Schulz, *Rev. Sci. Instrum.* **41** (1970) 423.
[20] J.D. Skalny, S. Matejcik, T. Mikoviny, J. Vencko, G. Senn, A. Stamatovic, T.D. Märk, *Int. J. Mass Spectrom.* **205** (201) 77.
[21] V. Grill, H. Drexel, W. Sailer, M. Lezius, T.D. Märk, *Int. J. Mass Spectrom.* **205** (2001) 209.

Alkali Clusters in Giant Spin States from Helium Nanodroplet Isolation

P. Claas, D. Schumacher, and F. Stienkemeier

Fakultät für Physik, Universität Bielefeld, D-33615 Bielefeld, Germany; email: franks@physik.uni-bielefeld.de

C.P. Schulz

Max-Born-Institut, Max-Born-Str. 2a, D-12489 Berlin, Germany

Superfluid helium nanodroplets (He_N, N≈5000) are produced in a supersonic expansion of helium gas under high pressure and low temperature conditions. Evaporative cooling keeps the droplets at an internal temperature of T=380mK. Doping with atoms and molecules can easily be achieved by pick-up from the gas phase. Hence, the droplets provide a weakly interacting and cold matrix for studies at very low temperatures. The application of this technique for matrix isolation spectroscopy has drawn much interest during recent times, governing many interesting new results (e.g. see special issue on helium nanodroplets in J.Chem.Phys. [1]).

Furthermore, molecules, clusters and weakly bound complexes can be synthesized when sequentially adding constituents under the low temperature conditions. In contrast to atoms and molecules which normally reside inside helium droplets, alkalis do not submerge in helium. They form weakly bound surface states due to the Pauli-repulsion of the helium electronic distribution and the alkali valence electrons. As a consequence the formation of alkali clusters on the surface is hindered by desorption from the droplet, induced by the dissipation of binding energy upon cluster formation. Hence, only weakly bound clusters survive the agglomeration process on the surface of a droplet. In this way, van der Waals bound alkali clusters, having all the spins of the valence electrons aligned in parallel, can be exclusively produced. We employed femtosecond multiphoton ionisation for studying this phenomenon. In Fig. 1 a mass distribution is shown, indicating the abundance of such high-spin clusters. The odd-even alternation of intensities is due to a spin relaxation mechanism induced by the laser excitation. Even the clusters having more than 10 constituents are totally spin-polarized. Since there is no question about the non-metallic property of these clusters, the electronic and geometric structure has to be experimentally confirmed in future experiments. We observed distinct differences in the cluster formation depending on the alkali used (Li, Na, K, Rb, Cs). Na and K readily form clusters up to N ≈ 20; in contrast, the formation of larger Rb and Cs clusters is suppressed. Finally, applying this method, Li does not form any clusters beyond the trimer. Absorption, ionisation and fragmentation properties of the clusters will be discussed.

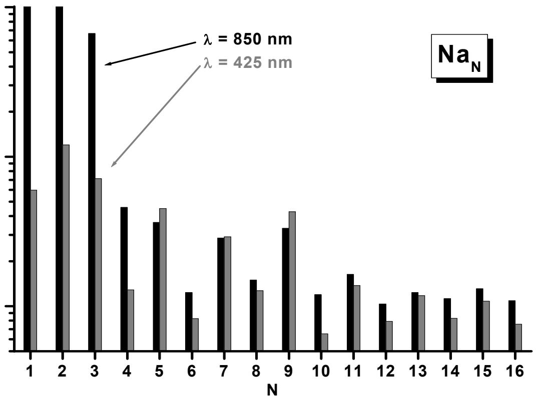

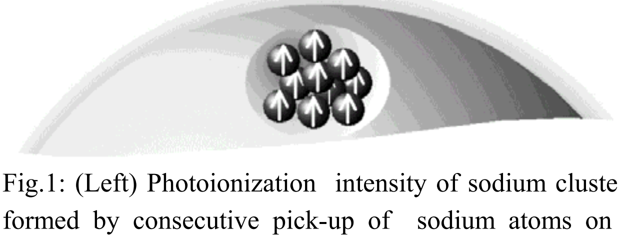

Fig.1: (Left) Photoionization intensity of sodium clusters formed by consecutive pick-up of sodium atoms on a helium nanodroplet at two different laser wavelengths. Selection of weakly bound complexes leads preferentially to clusters with all the valence electrons having parallel

References

---

[1] "Helium Nanodroplets: A Novel Medium for Chemistry and Physics", *J.Chem.Phys.* **115** (22), 10065-10281 (2001).

Ionization of Uracil Vapor by 20-150 keV protons

B. Coupier, B. Farizon, M. Farizon (a); M. Carré (b); S. Ouaskit (c); N.V. de Castro Faria, G. Jalbert (d);G. Hanel, P. Scheier and T.D. Märk (e)

(a) Institut de Physique Nucléaire de Lyon, IN2P3-CNRS et Université Claude Bernard, 43 Bd du 11 Novembre 1918, F-69622 Villeurbanne Cedex, France.
(b) L.A.S.I.M, CNRS UMR 5579 et Université Claude Bernard, 43 Bd du 11 Novembre 1918, F-69622 Villeurbanne Cedex, France.
(c) Laboratoire de Physique de la matière condensée, Faculté des sciences Ben M'sik, Casablanca, Marocco.
(d) Université Fédérale de Rio de Janeiro, Rio de Janeiro, Brazil.
(e) Institut für Ionenphysik, Leopold Franzens Universität, Technikerstr. 25, A-6020 Innsbruck, Austria.

This work must be attached to the study of the effects of radiations on bio molecules at the molecular scale, occurring in hadrontherapy for instance. Indeed, in the Bragg peak energy range of hadrontherapy, charge exchanges processes are occurring, leading to particularly destructive effects like strand breakings of DNA molecules. The survival of the irradiated cells is then under question. As a consequence, the study of these processes is of great interest to gain a better understanding of the biological effects of radiations. In a first step, we will study the effects of proton impacts on the isolated bases of the macromolecule, such as the uracil molecule $C_4H_4N_2O_2$ (one of the RNA bases).

The experimental set-up is schematically represented on the figure. Using a coincidence system between a TOF mass spectrometer and the outgoing-projectiles detectors, we are able to measure the branching ratio of electron capture processes versus direct ionization processes in proton-uracil collisions in the range of proton beam energy 20 to 150 keV.

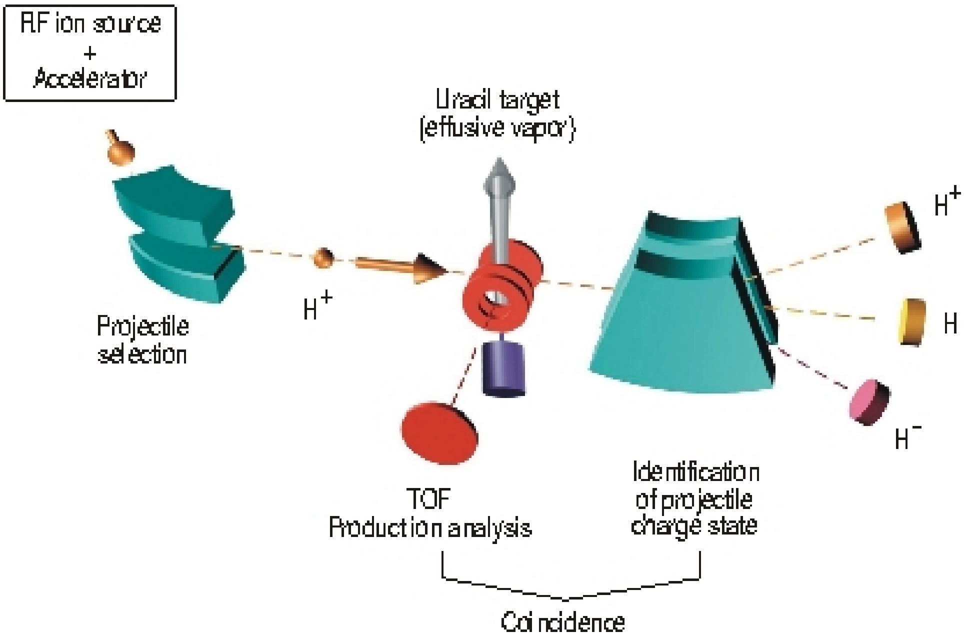

The velocity dependence of the Branching Ratio and the corresponding Uracil fragment spectra will be presented.

The intriguing steric dependence and interfering behaviour of rotationally inelastic NO-Ar, He and D_2 collisions.

Marc de Lange[a], Craig Taatjes[b], Marco Wisse[a], Geesje Boon[a], Paul Griffiths[a], Marcel Drabbels[a,c], Millard Alexander[d] and Steven Stolte[a]

(a) Laser Center and Department of Physical Chemistry, Vrije Universiteit, De Boelelaan 1083, 1081 HV Amsterdam, The Netherlands.
(b) Combustion Research Facility Sandia, National Laboratories, P.O.Box 969, Livermore, CA, 94551-0969 USA.
(c) Department of Chemistry, Swiss Federal Institute of Technology Lausanne, CH-1015 Lausanne EPFL, Switzerland.
(d) Department of Chemistry and Biochemistry, University of Maryland, College Park, MD 20742-2021 USA.

Abstract

The orientational dependence of the state to state rotational energy transfer collision cross section has been measured for NO with He or D_2 and found to be larger and more oscillatory in j', than that obtained for NO-Ar[1-3]. To elucidate this puzzling phenomenon of a strong and undulative steric effect for nearly symmetric NO, as predicted by ab initio theory [2], a new type of semiclassical approximation to the scattering problem is presented .

Introduction

The total inelastic collision cross-section of NO and Ar with $\Omega = \Omega'$ at $E_{tr} = 475 cm^{-1} (0.06 eV)$ exhibits a strong propensity to conserve parity. This homonuclear-like behaviour suggests that the total rotational inelastic cross-section ought to be rather insensitive whether the incoming Ar, (or He, D_2) impinges preferentially onto the N-end (σ_N) or onto the O-end (σ_O) of the NO-molecule.

Experimental

A pulsed beam of Ar, He or D_2 and a hexapole state-selected, pulsed beam of NO ($\Omega = \frac{1}{2}, j = \frac{1}{2}, \varepsilon = -1$) cross each other at the scattering centre. Here the incoming NO molecules are oriented by applying an electric orientation field $\vec{E}(\approx 30\, kV/cm)$. Depending upon $\vec{E} \uparrow\uparrow \vec{\upsilon}_{rel}$ or $\vec{E} \downarrow\uparrow \vec{\upsilon}_{rel}$ the N-end with $\langle \hat{r}_{NO} \cdot \hat{\upsilon}_{rel} \rangle = 1/3$ or the O-end with $\langle \hat{r}_{NO} \cdot \hat{\upsilon}_{rel} \rangle = -1/3$ of NO points preferentially towards its incoming collision partner. The yield of (scattered) NO molecules residing in a single ($\Omega', j', \varepsilon'$) state is detected by Laser Induced Fluorescence (LIF), using resonant excitation by a narrow-band (0.1 cm^{-1}) pulsed laser tuneable around 226 nm. The quantum number $\Omega' = \frac{1}{2}$ or $\frac{3}{2}$ indicates the fine structure state, j' the rotational state and $\varepsilon' = -1$ or 1 the symmetry of the selected Λ-doublet component.

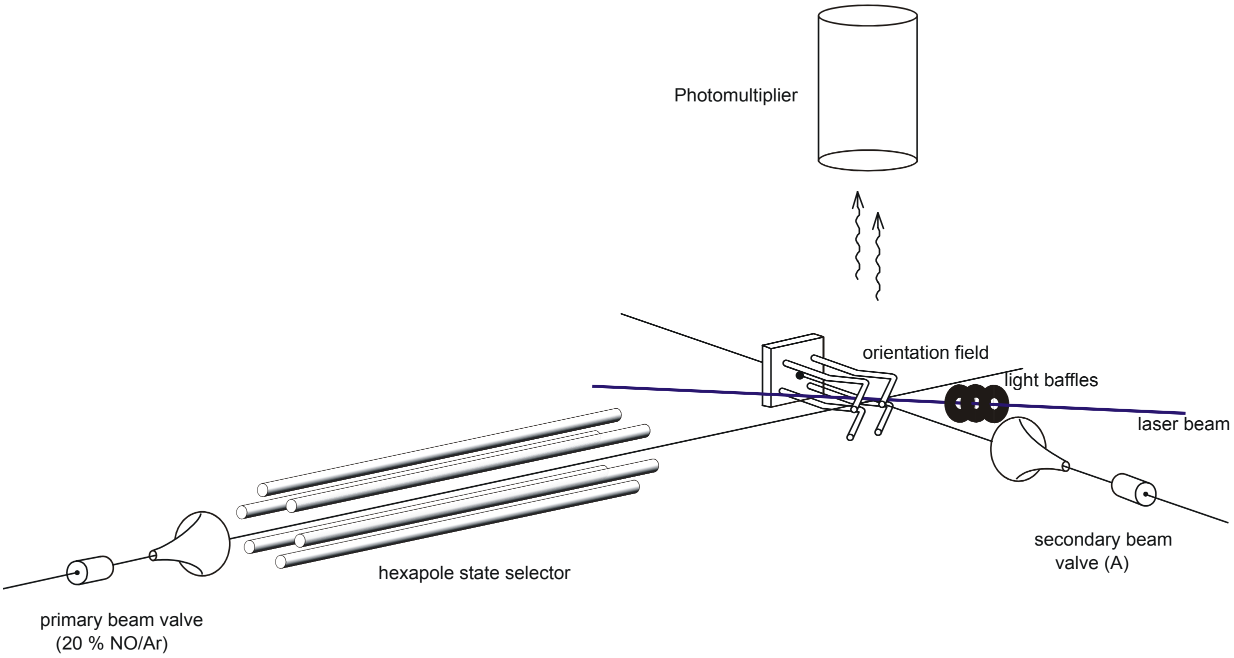

Fig. 1: The arrangement of the oriented NO-Ar, He, D_2 scattering experiment.

Results and Discussion

The steric asymmetry $S \equiv (\sigma_N - \sigma_O)/(\sigma_N + \sigma_O)$, which is used to quantify the dependence of a collision cross section upon molecular orientation, has been determined at E_{tr}=475 cm^{-1} for NO-Ar and at E_{tr}=502 cm^{-1} for NO-He or D_2. The measured values of S, which are depicted in fig. 2, at $\varepsilon' = 1$ and $\Omega' = \Omega = \frac{1}{2}$, as a function of j', $S(j', \varepsilon' = 1)$, show that $|S(j', \varepsilon' = 1)|$ for NO-He is almost a factor two larger than for NO-Ar. Additionally, the oscillatory behaviour is found to be much more pronounced for NO-He. The measured values of $S(j', \varepsilon' = -1)$ of NO-He, both for $\Omega' = \frac{1}{2}$ and $\Omega' = \frac{3}{2}$, are plotted in fig. 3. Here, for NO-He, the similarity of $S(j', \varepsilon' = -1)$ for $\Omega' = \frac{1}{2}$ and for $\Omega' = \frac{3}{2}$ is very striking. Such a similarity is found to be marginal for NO-Ar. Finally, for NO-He and NO-D_2, the observed values of $S(j', \varepsilon' = 1)$ with $\Omega' = \frac{1}{2}$ are displayed in fig. 4. Similarly, as obtained in differential scattering ion-imaging experiments [4] only small differences emerge in $S(j', \varepsilon' = 1)$ between NO-He and NO-D_2, which suggest a very similar anisotropic potential for both systems.

In our model to elucidate the surprisingly large steric asymmetries for a nearly symmetric NO molecule the ab-initio surface is simplified to an anisotropic hard shell potential. The transfer of collision energy into the outgoing j' state is assumed to occur impulsively at the turning point of a classical trajectory. Imposing conservation of incoming momentum perpendicular to the normal potential surface at the turning point, one can identify at every spatial orientation of the molecular axis a curved array of impact parameters that will contribute for a fixed j→j' to the same scattering angle ϑ. The spatial coherence of the state selected (j=m=Ω=1/2) NO oriented molecule wave function requires introduction of a phase shift η to account for interference among all outgoing "plane wave" rays, belonging to fixed j→j' and ϑ. This to obtain a semi-classical scattering amplitude. We will show and discuss the results of this calculation. The mechanism for the observed NO-orientation dependent interference resulting in the steric asymmetry oscillation will be elucidated. This mechanism explains why S is very sensitive to the anisotropy of the potential [3]. This could offer a possibility to resolve the unexpected discrepancy between the observed differential cross sections [4] and ab initio close coupling predictions [5]. Finally sophistication of our newly developed treatment could lead to the possibility of inverting experimental $S(j',\varepsilon'=\pm1)$, when resolved for scattering angle, into the anisotropic potential. Moreover, a pedestal to bimolecular control possibly emerges.

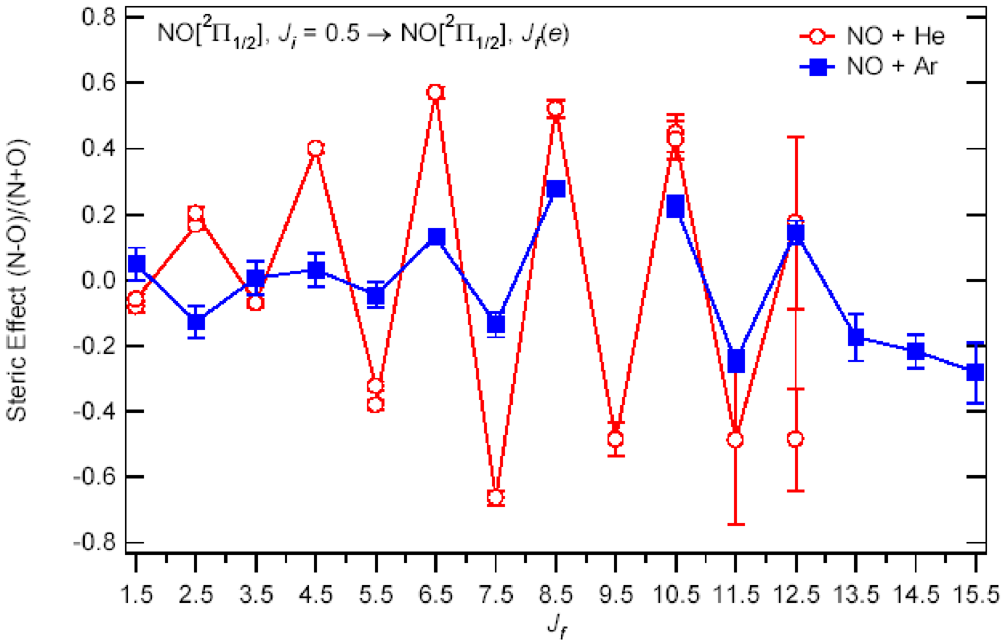

Fig. 2: The steric asymmetry $S(j',\varepsilon'=1)$*, with Ω'=Ω for NO-Ar [2] and NO-He. Note that S=0.6 corresponds* σ_N/σ_O *=4.*

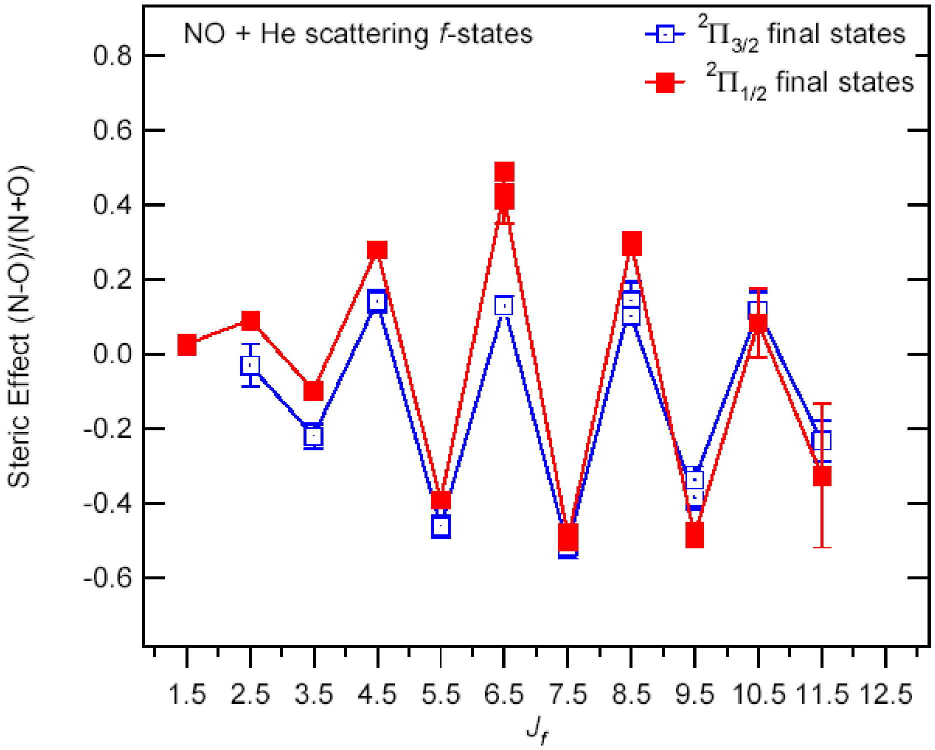

Fig. 3. $S(j',\varepsilon'=-1)$ *of NO-He for* $\Omega'=\frac{1}{2}$, $\Omega'=\frac{3}{2}$

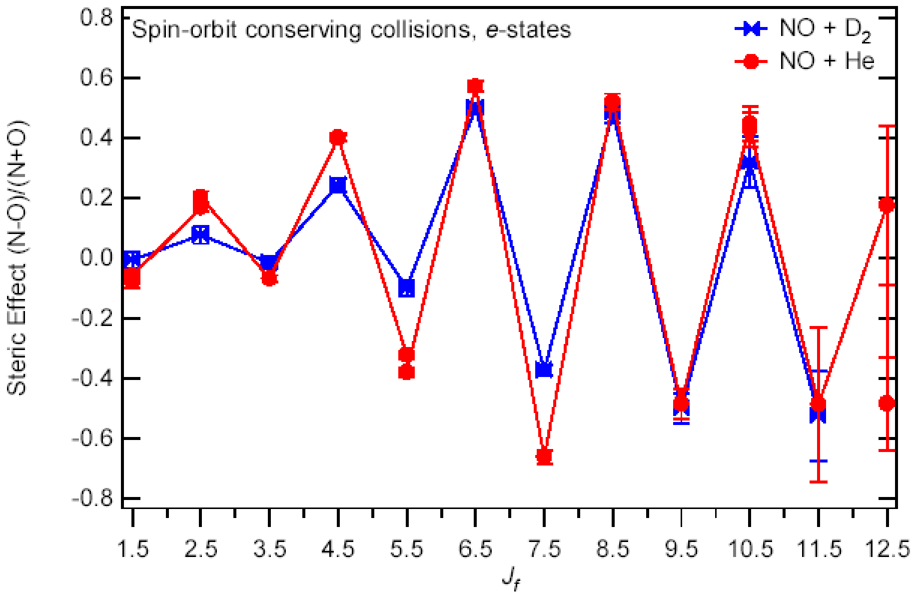

Fig. 4. $S(j',\varepsilon'=1)$ *for NO-He and for NO-D_2 with* $\Omega' = \frac{1}{2}$.

References

[1] M.J.L. de Lange, M. Drabbels, P.T. Griffiths, J. Bulthuis, S. Stolte and J.G. Snijders, *Chem. Phys. Lett.* **313** (1999) 49.
[2] J.J. van Leuken, J. Bulthuis, S. Stolte and J.G. Snijders, *Chem. Phys. Lett.* **260** (1996) 595.
[3] M.H. Alexander and S. Stolte *J. Chem.Phys.* **112** (2000) 8017.
[4] M.S.Westley, K.T.Lorentz, D.W. Chandler and P.L. Houston, *J. Chem. Phys* **114** (2001) 2669.
[5] M. Yang and M.H. Alexander, *J. Chem. Phys.* **103** (1995) 6973.

Electron impact ionization of the uracil molecule

S. Denifl, B. Gstir, G. Hanel, P. Scheier, B. Farizon[a)], M. Farizon[a)], T.D. Märk

Institut für Ionenphysik, Universität Innsbruck, Technikerstrasse 25, A-6020 Innsbruck, Austria
a)Institut de Physique Nucleaire de Lyon, IN2P3-CNRS et Universite Claude Bernard, 43 boulevard du 11 Novembre 1918,69622 Villeurbanne Cedex,France

With the recently rising interest in the properties of biomolecules and astromolecules we have also started a series of measurements concerning inelastic electron scattering (ionization / attachment) on these molecules. Here first measurements have been carried out for the uracil molecule $C_4H_4N_2O_2$. Uracil is one of the four bases in the human cellular RNA. Besides electron attachment experiments at electron energies in a range from 0 to 15 eV, which can be also done with the present apparatus (see contribution same conference), our main task here was to investigate positive ion formation and dissociation at higher electron energies in a range from 8 to 30eV.

The main part of the apparatus used is a hemispherical electron monochromator [1] with a maximum energy resolution of about 30meV and a maximum electron energy of 600eV. This energy resolution was determined by electron attachment studies of the zero energy Cl^- yield of CCl_4.

The interaction between the uracil and the monochromatized electron beam occurs in the collision chamber which is directly mounted onto the monochromator. After the crossing point of the electron beam and the uracil beam the ions produced are mass separateted by a commercial quadrupol mass spectrometer (Balzers QMG421C). At the exit of the quadrupole mass spectrometer the ions are deflected into a channeltron mounted off-axis. In the present experiment the energy resolution of the electron beam was typically chosen to lie in the range between 100 and 130 meV. The major problem encountered in doing these measurements was the rather low intensity of the evaporated uracil in the collision chamber. Uracil is a white powder at room temperature and at first an existing Knudsen type C_{60} oven was used but too low signal was achieved. To increase the neutral beam intensity it was necessary to move the nozzle of the evaporation oven used as near as possible to the crossing zone with the electron beam. Thus obtaining an optimum situation for the determination of appearance energies. The temperature of the oven during operation of the experiments was kept between 180° and 185°C.

With this experimental setup it is possible to determine ionization appearance energies for atoms and molecules up to charge states of about 7 (see recent measurements on multiple ionization of rare gas atoms by Gstir et al same conference).

Here, the electron impact ionization cross section was measured as a function of the electron energy from a few eV below the threshold to about 3 eV above its onset. The calibration of the energy scale was made relative to well known threshold values for singly charged rare gas ions. In the present case we used xenon and krypton for calibration.

The measured raw data for the ionization cross section near the threshold were fitted with a nonlinear least squares fit procedure [3]. This procedure uses the Marquart-Levenberg algorithm for the fit. Addionally the fit procedure includes a weighting function to achieve better values for the ionization energies [3]. In short, a function F(E) is fitted over an energy range which incorporates the threshold region:

$$F(E)=b \qquad E<AE \qquad (1)$$

$$F(E)=b + c(E-AE)^p \qquad E>AE \qquad (2)$$

The fit involves the four parameters:

b	the background signal
AE	the appearance energy
c	scaling constant
p	an exponential factor (Wannier factor)

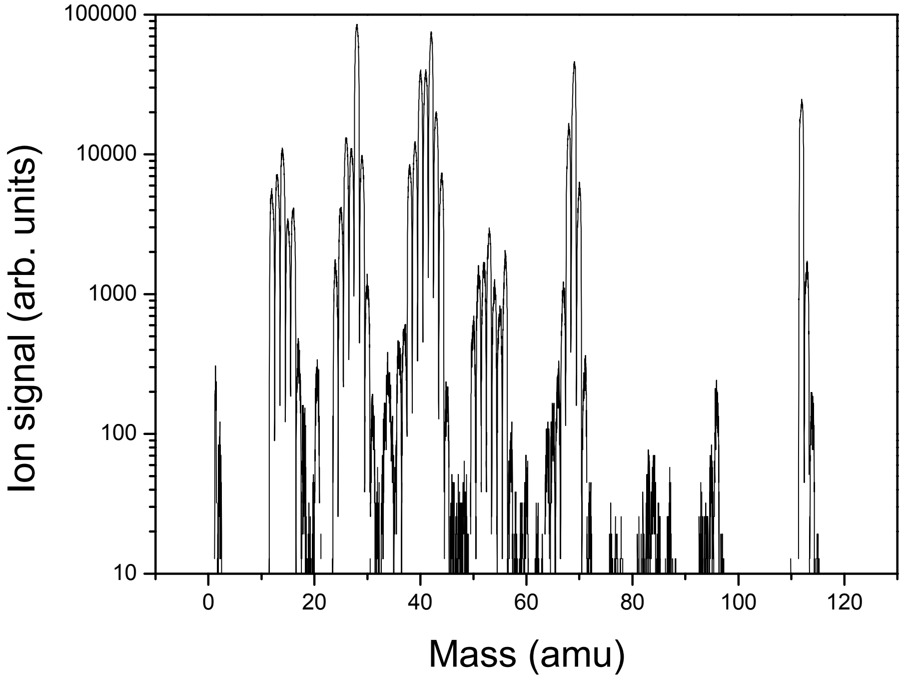

Fig.1:Mass spectrum of the uracil molecule

Fig.1 shows as an example an uracil mass spectrum measured at an electron energy of 100eV. It shows the parent ion at 112 amu and various fragments due to dissociation reactions. The fragments with the highest intensities are at mass 69 amu identified as $(H_3C_3NO)^+$ and mass 42 amu identified as $(OCN)^+$. After proper identification of all the ions present (also in comparison with a mass spectrum obtained by proton ionization in Lyon by Farizon et al., see same conference) we have been able to measure for all of these ions corresponding threshold ionization efficiency curves. Using the analysis technique outlined above and described in detail in [3] it is then possible to determine the corresponding parent ion and fragment ion appearance energies. Values obtained will be compared where available with previous determinations.

Work supported by the FWF,Wien, Austria, the Austrian-French Amadee program and the European Commision, Brussels.

References

---

[1] G. Denifl, D. Muigg, A. Stamatovic, T.D. Märk, *Chem. Phys. Lett.* **288** (1998) 105

[2] G.H. Wannier, *Phys. Rev.* **90** (1953) 817

[3] S. Matt, O. Echt, V. Grill , P. Scheier, C. Lifshiz, T.D. Märk, *Chem. Phys. Lett.* **264** (1997) 149

Generation of Atomic H and O Vacuum Ultraviolet Emissions in High-Pressure Dielectric Barrier Discharge Plasmas and Microhollow Cathode Discharge Plasmas in Ne-H_2 and Ar-O_2 Gas Mixtures

A. El Dakroury[1], J. Yan[1], P. Kurunczi[2,3], K. Martus[4], M. Laroussi[1], M. C. Gupta[1], and K. Becker[2]

[1] *Applied Research Center, Old Dominion University, Norfolk, VA, USA*
[2] *Department of Physics, Stevens Institute of Technology, Hoboken, NJ, USA*
[3] *Plasmion Corporation, Hoboken, NJ, USA*
[4] *Department of Chemistry and Physics, William Paterson University, Wayne, NJ, USA*

ABSTRACT

As the semiconductor industry pushes toward ever smaller chip feature sizes (< 100 nm), ever shorter wavelengths are sought for the photolithographic process used in their fabrication. We used two types of plasma-based light sources for the generation of near-monochromatic vacuum ultraviolet atomic hydrogen (121.6 nm) and oxygen (130.6 nm) line emissions, (i) a variant of a dielectric barrier discharge and (ii) a microhollow cathode discharge. When operated in high-pressure mixtures of Ne (Ar) with a trace admixture of H_2(O_2) both sources emit intense, near-monochromatic atomic line H and O emissions. The underlying microscopic processes have been identified as near-resonant energy transfer from Ne_2^* to H_2 and resonant absorption of Ar_2^* excimer radiation by O atoms produced from O_2 in the plasma, respectively.

1. Introduction

High-pressure discharge plasmas have been used extensively for the generation of non-coherent UV and VUV excimer radiation using either pure rare gas or rare gas - halide mixtures [1,2]. Rare gas atoms have a $^1S_0$ electronic ground state. The lowest excited-states result from the promotion of a (np) valance electron to the (n+1)s-level (n=2,3,4,5 for Ne, Ar, Kr, Xe) leading to four "P-states", two of which are metastable, while the other two states decay to the ground state via dipole-allowed transitions. Excimer molecules are formed via three-body collisions involving a metastable rare gas atom and two ground state atoms (and via other collisional interactions between electrons and atomic and molecular ions), if (i) there is a sufficiently large number of electrons with energies above the threshold for the formation of metastable rare gas atoms, and if (ii) the pressure is high enough in order to have a sufficiently high rate of three-body collisions. Rare gas excimer emission spectra are dominated by transitions from the lowest lying bound $^1\Sigma_u$ and $^3\Sigma_u$ excimer states to the repulsive ground state (second continuum) [1-3] with peak emissions at 170 nm (Xe), 145 nm (Kr), 130 nm (Ar), 84 nm (Ne), and 75 nm (He). Spectroscopy of the Ne_2^* and He_2^* excimers requires specially designed "open" discharge sources [3] connected directly to a VUV monochromator, since no material is transparent below 105 nm.

Recent studies [3,4] have revealed that the generation of Ne_2^* excimers in the presence of trace amounts of H_2 result in intense emissions of near-monochromatic H Lyman-α radiation at 121.6. nm. We attribute the observed Lyman-α emission to the near-resonant energy transfer from the Ne_2^* excimer (14.5 – 15.5 eV corresponding to an emission wavelength of 80-85 nm) to H_2 leading to the dissociation of H_2 (which requires 4.48 eV) and the excitation of the n=2 state of H (which requires 10.2 eV). Similarly, Ar_2^* excimers when generated in discharge plasmas in the presence of trace amounts of O_2 result in an intense atomic O line emission at 130.6 nm. This emission is attributed to the effective absorption of the Ar_2^* excimer radiation by O atoms generated in the discharge plasma from O_2. We have explored the utility of these atomic line emissions from different high-pressure discharge plasmas for advanced photolithography applications. The influence of the operating pressure, gas mixture ratio, and the applied power on the emission spectra, the emitted optical power, and the stability of the sources will be presented at the Conference.

2. Experimental Details

The first light source is based on the hollow cathode concept. Hollow cathode (HC) discharges consist of a metallic cathode with hole, an arbitrarily shaped metallic anode, and an insulating ceramic in between. HC discharges show several modes of operation as a function of gas pressure p, hole diameter D, cathode-anode separation d, and discharge current I. At values of the product $p \cdot D$ below 10 Torr · cm and low currents (below 1 mA), a normal glow discharge develops along the path of the vacuum electric field. As the current increases, a transition to the hollow cathode mode occurs, in which the ionization is concentrated along the axis of the discharge and the discharge is sustained by energetic “pendulum electrons” [1,2]. If the current is increased further, an abnormal glow discharge develops. The hole diameter D is inversely proportional to the pressure up to about 10 Torr/D (in cm) for noble gases and N_2 [1,2], so that atmospheric-pressure operation requires a hole diameter of the order of 100 μm (microhollow cathode or MHC discharge). The electrodes of our MHC discharge are made of 0.1 mm thick molybdenum foils separated by a 0.25 mm spacer of mica with a hole of typically 0.05 - 0.2 mm diameter in the cathode, the dielectric, and in the anode. Supply voltages V_o are typically 400 to 700 V and sustaining (discharge) voltages are in the range of 200 - 300 V depending on the gas, the pressure, and the actual geometry of the MHC discharge. Discharge currents I_{DIS} vary between 1 - 10 mA. The circuit includes a resistor R_{CVR} which allows us to monitor the discharge current directly on an oscilloscope along with the discharge sustaining voltage V_{DIS}. We can also operate the MHC discharge in a pulsed dc mode with frequencies up to tens of kHz, pulse lengths from 100 ns to 1 ms and variable pulse separation and duty cycle using a versatile pulse generator.

The second light source that we used employs a novel, patented variant of a high-pressure dielectric barrier discharge (DBD) based on a cylindrical design, which was developed by Laroussi and co-workers [5]. The discharge unit consists of a hollow dielectric tube with two loop-shaped electrodes wrapped around the outside wall of the tube which are separated by a distance of a few millimeters. The discharge is generated inside the tube by means of a 13.56 MHz radio-frequency (rf) source. An impedance matching network inserted between the rf power source and the discharge unit ensures maximum coupling of the rf power into the plasma.

Spectroscopic measurements were carried out in high-pressure Ne or Ar (several hundred Torr) with small admixtures of H_2 or O_2 (up to 1 Torr) using the discharge source in an “open” mode, i.e. mounted directly to the entrance slit of a Minuteman 302-V 0.2 m VUV monochromator (wavelength range 50 - 250 nm, reciprocal linear dispersion of 4 nm/mm) or in a “closed” mode where the discharge is sealed by a LiF or MgF_2 window and only radiation of wavelengths longer than 115 nm (i.e. only the atomic resonance emissions) can be detected. In the “open” mode, the Ne radiation from the MHC discharge (60 -90 nm) enters the VUV monochromator through a 200 μm pinhole between the discharge region and the monochromator, which reduces the gas load from the high-pressure discharge into the separately pumped monochromator and detector regions. The VUV photon were detected by a channel electron multiplier or a VUV photomultiplier tube connected to a standard pulse counting system.

3. Results and Discussion

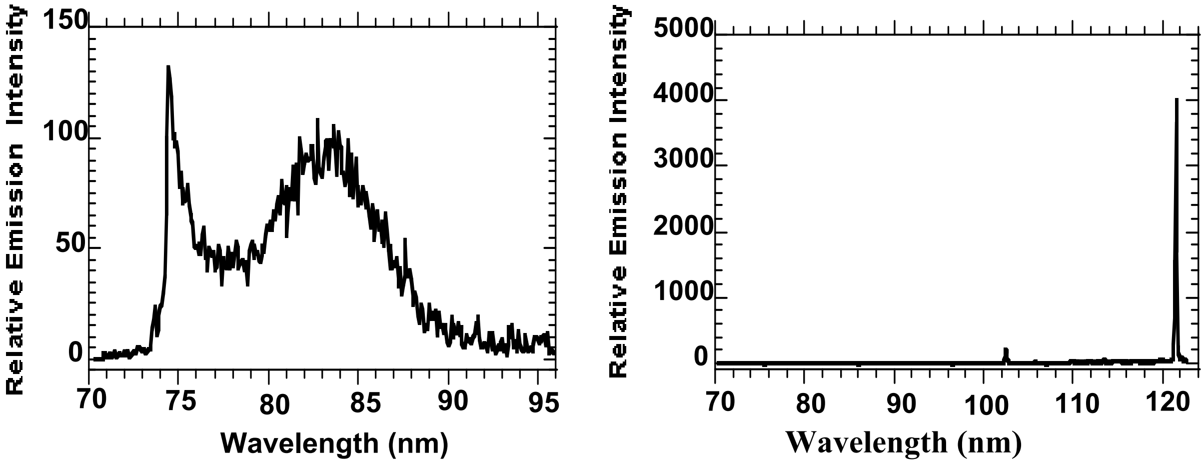

Fig. 1: Left: Emission spectrum in the 70–95 nm region from a MHC discharge in 740 Torr Ne; right: Emission spectrum in the 70–125 nm region from a MHC discharge in 740 Torr Ne with a 1.5 Torr admixture of H_2.

The first experiments were carried out with a MHC discharge in high-pressure Ne (up to 760 Torr) either pure or with small admixtures of H_2 (up to about 2 Torr). Fig. 1 (left spectrum) shows the emission spectrum from a 740 Torr pure Ne MHC discharge in the spectral range from 70 - 95 nm. The emission feature between 73 and 77 nm corresponds to the Ne_2^* first excimer continuum around 75 nm (with a small residual presence of the Ne resonance lines at 73.5 and 74.3 nm). The broad emission feature in the region 76-88 nm is attributed to the second continuum of the Ne_2^* excimer emission. Fig 1 (right spectrum) shows an emission spectrum between 70 and 125 nm from the same MHC discharge operated in a mixture of Ne (740 Torr) and H_2 (1 Torr). There are essentially no emissions in the region of the Ne resonance lines and the Ne_2^* excimer. The spectrum is totally dominated by two intense atomic lines at 121.6 nm and 102.5 nm which coincide with the Lyman-α (121.6.nm) and Lyman-β (102.5 nm) lines of atomic hydrogen. The intensity of these two atomic line emission is orders of magnitude higher than what one expects from a conventional discharge containing 1 Torr H_2 [3,4].

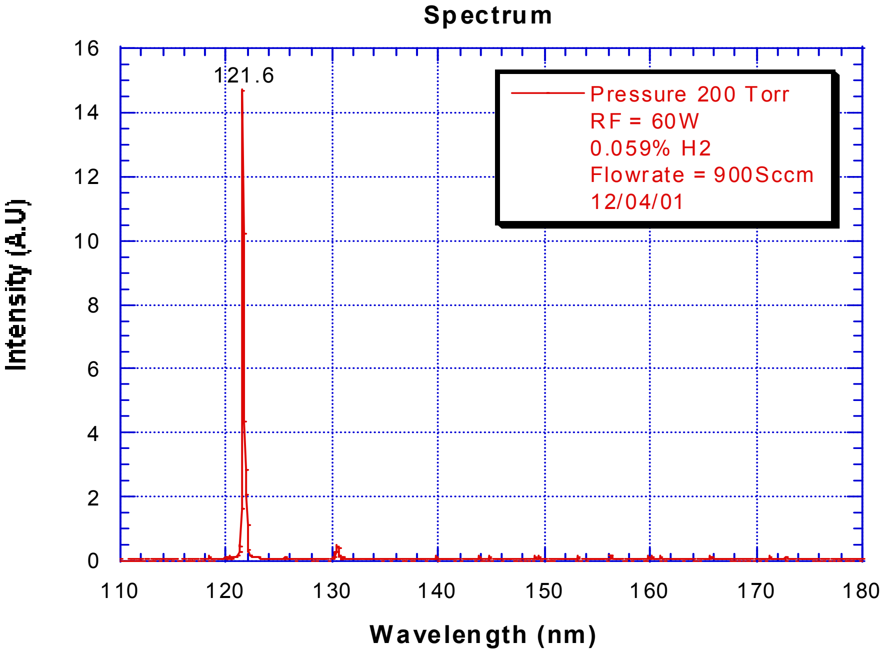

Fig. 2: Emission spectrum in the 110 – 180 nm region from a cylindrical DBD discharge in 200 Torr Ne with a 0.059% admixture of H_2.

Fig. 2 shows the emission spectrum from the DBD source in the wavelength region between 110 nm and 180 nm. It is obvious that the emission spectrum on the long-wavelength side of the Lyman-α line is also essentially free from other emissions (except for a weak emission feature at the position of the O resonance line). This demonstrates that the Lyman-α emission from such high-pressure discharge sources is essentially monochromatic.

Further details of the two light sources, of the underlying microscopic processes that lead to the VUV line emissions, and the operating parameters of the discharge light sources and their correlation to the spectral characteristics of the emitted lines will be presented and discussed at the Conference.

Acknowledgments

This work was supported by the NSF and by DARPA. We acknowledge helpful discussions with K.H.Schoenbach and U. Kogelschatz.

References

[1] K.H. Schoenbach et al., Plasma Sources Sci. Technol. 6, 468 (1997)
[2] A. El-Habachi and K.H. Schoenbach, Appl. Phys. Lett. 72, 22 (1998)
[3] P. Kurunczi et al, J. Phys. B 32, L651 (1999)
[4] J. Wieser et al., J. Phys. B 31, 4589 (1998)
[5] M. Laroussi, in Proc. IEEE Int. Conf. Plasma Sci., p. 203, Monterey, CA, June 1999

Production of oxides by RF assisted pulsed laser deposition

A.Giardini§, V. Marotta, S. Orlando*, A. Paladini§, G. D'Amico, and G. P. Parisi

CNR – Istituto per i Materiali Speciali
Zona Industriale di Tito Scalo, I – 85050 Tito Scalo (PZ), Italy
§also at: Dipart. di Chimica, Universita' "La Sapienza"
Piazzale A. Moro 5 , I – 00185, Roma, Italy

INTRODUCTION The interest in metal oxide thin film technology has grown enormously during the last decades. These films are important for several applications, including optical and protective coatings, microelectronic applications, and photochemical active layers. Among them quite relevant is tungsten trioxide (WO_3) which an important electro-chromic material [1]. It has been recognized that WO_3 can be coloured through electro-, photo-, gas-, laser-induced and thermochromism processes [2-4]. Thin films of tungsten oxide have been made by physical methods, such as evaporation, sputtering and pulsed laser deposition (PLD), and chemical methods, such as chemical vapour deposition (CVD) [5], sol-gel and electrochemical methods.

Zinc oxide (ZnO) is an interesting wide-bandgap II-VI semiconductor with a lot of scientific and technological potential applications. For instance, it is characterized by high optical transparency in the visible region, also stable for chemical as well as thermal fluctuations, with a reasonably good electrical conductivity. Therefore, ZnO thin films are suitable as electrode materials in photodetectors [6]. ZnO exhibits good piezoelectric, photoelectric and optical properties, and might be a good candidate for electroluminescence devices. ZnO films can also be used for application in surface acoustic wave (SAW) devices and low-loss optical waveguides. It is one of the promising candidate in optoelectronic applications like energy windows, liquid crystal displays, light emission devices, solar cells, gas sensors, ultrasonic oscillators, trasducers, etc. [7]. A variety of methods were used to fabricate ZnO thin films, including molecular beam epitaxy (MBE), Radio Frequency (RF) sputtering, ion plating, spray pyrolysis, and CVD [8]. Recently, pulsed laser deposition (PLD) became a powerful deposition method, and various thin films were produced successfully [9]. In the ZnO film depositions [10-12], the most common PLD method is to focus an excimer or a Nd:YAG laser onto a zinc oxide target, in vacuum or in oxygen atmosphere [13].

In this work we present the depositions of tungsten oxide and zinc oxide thin films performed by reactive pulsed laser ablation and deposition (RPLAD). This technique combines the several advantages of conventional PLD, such as deposition in relatively high partial pressure, crystallization of films at lower temperature because of the higher energy of the ablated particles in the laser-produced plume, and relatively high deposition rates [14], with the enhancement of the reactivity in the gas phase due to the presence of a reactive buffer gas. In our experiments, the reactive gas is a RF generated oxygen plasma.

EXPERIMENTAL The laser ablation experiments were carried out in a multiport stainless steel vacuum chamber equipped with a gas inlet, a rotating multi-target and a heatable substrate holder (Fig. 1). The vacuum pressure of the deposition chamber was below 10^{-3} Pa whereas the oxygen gas pressure during film depositions was 10 Pa. The deposition temperature could be varied from room temperature up to 1000 K. The fluence of the laser employed (Quantel Nd:YAG 581, λ=532 nm, pulse duration=7 ns, repetition rate=10 Hz) has been kept nearly constant at 8 J/cm^2. The laser impinges on the target surface at an angle of 45° with respect to the normal.

---

*Corresponding author: Tel. +39 0971 427259; Fax +39 0971 427222; E-mail: orlando@ims.pz.cnr.it

The PLD set up has been improved by employing a RF plasma system placed just above the substrate holder (Fig. 1), maintaining this last one electrically connected to the ground. The substrate holder is surrounded by an isolated stainless steel top-hat connected to the RF generator, through a customized matching unit. A 3 cm diameter hole on the top-hat allows the deposition of the plume coming from the ablated target. The RF power generator is a 13.56 MHz ENI Model OEM-6, maximum power output 650 W.

A zinc disk, and a tungsten foil (0.5 mm thickness), 99.9+% purity (Aldrich 35,718-9) were used as target materials. The one inch diameter metallic disks have been obtained pressing at about 300 MPa, granular zinc -30+100 mesh 99,8+% purity (Aldrich 24,347-7). All the targets were rotated at 2 rpm during depositions.

The gaseous species have been collected on Si (100) and quartz substrates positioned, with the on-axis configuration, 5 cm far from the target, on a heatable holder.

The deposited thin films were analyzed by x-ray diffraction (XRD) and scanning electron microscopy (SEM).

A commercial laser microprobe mass analyzer (LAMMA) Leybold 500 [15] based on a time of flight mass spectrometer (TOF-MS) was employed to analyze positive and negative ions, coming from the ablation process of thin films deposited on suitable quartz substrates. The laser source employed for the ablation is a pulsed frequency-quadrupled Nd:YAG (wavelength=266 nm, pulse duration = 6 ns) operating at 10^8-10^9 W/cm^2.

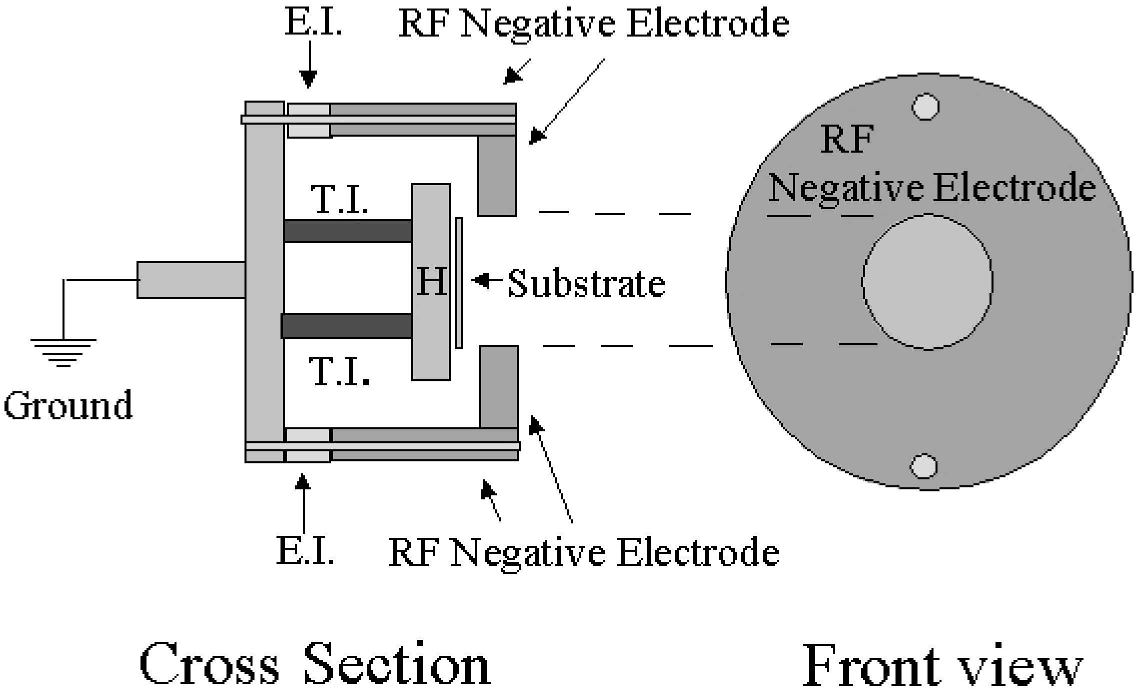

Fig. 1. Schematic layout of the heatable sample holder (H) hooded by a stainless steel top-hat, with a 30 mm diameter hole, in which it is inserted the output of the matching network coming from the RF power generator. (E.I. = electrical insulator, T.I. = thermal insulator).

RESULTS The surface morphology of the deposited thin films has been studied by SEM. Tungsten oxide thin films show a smooth surface with only few particulates. SEM photographs of zinc oxide on Si (100) deposited without RF discharge and in presence of RF oxygen plasma show a surface smoothness quite good even if particulates are present in samples produced in both PLD processes, with and without the RF plasma. The thin films deposited in RF oxygen plasma show a particulate less closely distributed with respect to the one of the samples produced by conventional PLD. To evaluate the adhesion of the deposited thin films, we performed tape tear tests which confirmed a slight difference between samples produced with and without RF plasma. The RF plasma deposited thin films presented a very good adhesion.

XRD patterns of the tungsten oxide samples deposited on Si (100) in RF oxygen plasma are measured as function of the substrate temperature, from 373 to 973 K. It is quite evident that at low temperature the growth of cubic W_3O is preferred, but this phase decreases rapidly, and the formation of cubic WO_3 is favoured in the thermal range of 500-750 K. At 773 K it is possible to note the cubic phase of metallic tungsten. At higher temperature only the cubic phase of metallic tungsten can be recognized in the spectra of the thin films deposited.

X-ray patterns of the ZnO samples deposited without and with RF discharge show spectra ordered as increasing substrate temperature. A clear depletion of peak intensities of the samples as function of the increasing substrate temperature, probably due to the reduction of the film thickness as consequence of the variation of the sticking coefficient, is observed. This behaviour suggests that high substrate deposition temperature does not favour ZnO formation. The intensities of ZnO (101) plane are always smaller than those of (002). On the other hand, the spectra of thin films produced by RF plasma-assisted PLD show a preferential growth of (101) planes up to 600 K. Beyond this substrate temperature, the (002) becomes the preferred orientation of the thin films, at least up to 800 K. Therefore, comparing the XRD spectra of the samples produced by conventional PLD and by plasma-assisted PLD, the effect of RF plasma could be synthesized in a strong depletion of the ZnO (002) planes up to a deposition temperature of 600 K and an enhancement of the same ZnO (002) planes beyond 600 K. The similarity of XRD spectra of samples deposited by conventional PLD at 573 K and those produced by RF plasma-assisted PLD at 673 K could be the evidence of a shielding effect. The presence of the RF plasma, just upon the substrate, seems to shield the plume, or at least its charged components.

The laser microprobe mass analysis was employed to detect positive and negative ions, resulting from the ablation process of the thin films previously deposited on quartz substrates. In particular, here it is reported the LAMMA analyses performed on tungsten oxide thin films. Part of a typical mass spectrum of negative ions, detected during the analysis, is shown in Fig. 2. The fingerprint of tungsten is given by the following isotopic abundances: 182 (26.3%), 183 (14.3%), 184 (30.7%), 186 (28.6%). It is evident the detection of the tungsten-oxide family, starting around 200 m/e (WO) and going on with WO_2, WO_3, WO_4. W_2O_4, W_2O_5, W_2O_6, and W_2O_7 are detected with weak intensities. The intensity of the W2 is quite negligible. The abundance of WO_3 may confirm that, during the process, the deposition of tungsten oxide takes place. The spectra of positive ions (not reported) show preferentially the W and W_2 abundances, with only few clusters of WO and WO_2. The aim of this analysis is that of appreciating only qualitatively the achievement of WO_3 deposition by RF assisted PLD. However, more reliable analyses of such deposits have been already performed and they confirm that RF plasma-enhanced reactive PLD is a suitable technique for depositing not only oxides but also nitrides [16].

CONCLUSIONS Tungsten oxide and zinc oxide thin films have been deposited on Si (100) substrates by RF plasma-assisted reactive pulsed laser ablation of metallic target in 10 Pa O_2 atmosphere using a doubled frequency Nd:YAG laser (532 nm). Depositions have been performed at various substrate temperatures ranging from 373K up to 873K. The surface morphology of deposited thin films has been roughly evaluated by SEM analysis. The XRD analyses have shown that tungsten oxide samples, produced in RF oxygen plasma, grow as cubic W_3O and as cubic WO_3 depending upon the deposition temperature. Above 800 K only the cubic phase of metallic tungsten can be recognized in the spectrum of the thin films deposited. For ZnO thin films, a clear depletion, as function of the substrate temperature, has been shown in sample deposited without the RF discharge plasma. Instead, for those produced by RF plasma-assisted PLD, it has been evidenced that the preferential orientation changes from (101) to (002) around a substrate temperature of 600 K. A comparison between the conventional PLD and the RF plasma-assisted PLD showed the influence of the RF plasma in the reactivity of the plume, modifying the surface roughness and performing a better adhesion to the substrates by the plasma-aided thin films, as confirmed also by adhesive tape tear tests. In conclusion, the performed analyses, even if not exhaustive, confirm that RF plasma-enhanced reactive PLD is a suitable technique for depositing metal oxide thin films as previously found for nitrides [16]. Work is still in progress to identify the best settings of the experimental parameters, such as oxygen pressure, RF applied power, target-substrate distance, laser fluence, with the aim to optimize the effects on the surface and structure, during deposition of the thin films.

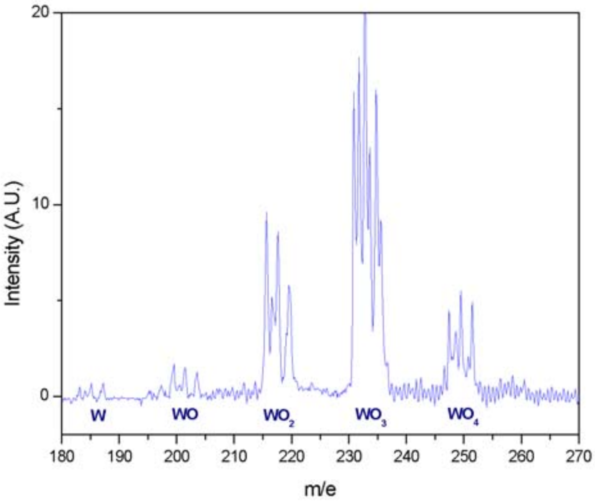

Fig. 2. LAMMA spectrum in the range 180-270 m/e evidencing the negative ions detection of tungsten and tungsten oxide clusters.

ACKNOWLEDGEMENTS This work was partially supported by Progetto Strategico MSTA II of Consiglio Nazionale delle Ricerche (CNR) of Italy.

REFERENCES

[1] G. J. Fang, Z. L. Liu, G. C. Sun, K. L. Yao, *Phys. Stat. Sol. (a),* **184** (2001) 129.
[2] M. Green, Z. Hussain, *J. Appl. Phys.,* **69** (1991) 7788.
[3] J. S. E. M. Svenson, C. G. Granqvist, *Sol. Energy Mater.,* **11** (1984) 29.
[4] H. H. Kung, *Surf. Chem. Catalysis,* **45** (1989) 259.
[5] R. G. Gordon, S.Barry, J. T. Burton, R. N. R. Broomhall-Dillard, *Thin Solid Films,* **392** (2001) 231.
[6] M. Okoshi, K. Higashikawa, M. Hanabusa, *Appl. Surf. Sci.,* **154-155** (2000) 424.
[7] S. H. Bae, S. Y. Lee, B. J. Jin, S. Im, *Appl. Surf. Sci.,* **154-155** (2000) 458.
[8] F. C. M. Van de Pol, *Ceram. Bull.,* **69** (1990) 1959.
[9] D. B. Chrisey, G. K. Hubler, *Pulsed Laser Deposition of Thin Films*, Wiley, New York, 1994.
[10] V. Craciun, J. Elders, J. G. E. Gardeniers, I. W. Boyd, *Appl. Phys. Lett.,* **65** (1994) 2963.
[11] N. J. Ianno, L. Mc Conville, N. Shaikh, S. Pittal, P. G. Snyder, *Thin Solid Films,* **220** (1992) 92.
[12] M. Ogasawara, M. Shimizu, T. Shiosaki, *Jpn. J. Appl. Phys. Lett.,* **31** (1992) 2971.
[13] R. D. Vispute et al., *Appl. Surf. Sci.,* **127-129** (1998) 431.
[14] W. S. Hu, Z. G. Liu, J. Sun, S. N. Zhu, Q. Q. Xu, D. Feng, Z. M. Ji, *J. Phys. Chem. Solids,* **58** (1997) 857.
[15] D. Consalvo, A. Mele, D. Stranges, A. Giardini Guidoni, R. Teghil, *Int. J. Mass Spectrom. Ion Phys.,* **91** (1989) 319.
[16] A.Giardini, V. Marotta, S. Orlando, G. P. Parisi, *Surf. Coat. and Technol.,* XXX (2002) in press.

Absolut partial and total electron impact ionization cross sections for CH_4 from threshold to 1000 eV.

K. Głuch, R. Parajuli, S. Matt-Leubner, A. Stamatovic, P. Scheier and T.D. Märk

Institut für Ionenphysik, Leopold Franzens Universität, Technikerstrasse 25, A-6020 Innsbruck, Austria

Electron impact ionization cross sections for the production of ions for hydrocarbons are of interest in many branches of physical science, i.e., especially for elucidating fundamental processes in the energy deposition of biological cells [1] and for investigating reactive processes near the edge of the hot hydrogen fusion tokamak plasma involving interactions with the inner walls consisting of carbon coated materials [2]. The present measurements of the partial and total ionization cross section functions in the energy range from threshold up to 1000 eV for methane and other hydrocarbons were carried out with a modified NIER type ion source and a double focussing reversed geometry mass spectrometer. Ions produced by electron impact ionization are extracted from the collision chamber through a slit in the first electrode with the help of an electric field penetrating into the collision chamber. The collision chamber, first electrode and pusher are kept on the same potential, typical 3 kV (ion accelerating voltage). Two pairs of deflecting plates (in parallel and perpendicular to the direction of the entrance slit) are used to sweep the extracted ion beam across the mass spectrometer entrance slit. The gas under study can be introduced into the ion source via the capillary leak gas inlet, thereby allowing to generate a stagnant gas target in the ion source. The stabilized electron beam current (kept typically between 1 μA and 10 μA) is aligned by a weak magnetic field (~400G). The energy spread of the electron beam is approximately 0.5 eV (FWHM). Fractions of the ions extracted from the ions source are analyzed in a 48.5° magnetic sector field followed by 90° electric sector field. To measure absolute ion currents a Faraday cup may be used instead of the standard single ion channeltron counting detection set-up. A detailed description of the apparatus has been given previously [3-5].

In order to determine the absolute partial ionzation cross section it is nessesery to correlate uniquely the mass analyzed individual ion signals at the ion collecting system to the number of ions produced in the ion source under known interaction parameters as gas density, electron current, interaction length [6]. This is a very difficult task because of the mass to charge discrimination in the ion source and the mass to charge dependent transmission of the mass spectrometer. In order to avoid discrimination at the entrance slit of the mass spectrometer it has been shown [3] that for ions without kinetic energy (parent ions) it is sufficient to sweep the extracted ion current perpendicular across the entrance slit and to integrate over the recorded *y*-ion beam profile. For (energetic) fragment ions this can be also achieved, according to Ref. [5], by operating a 1 kHz sweep generator on the *y*-direction plates while operating a z scan and then integrating over this *z*-ion beam profile. Moreover, it is also necesery to extract a *known* fraction of all ions of a specific species produced in the ion source to obtain a reliable measure for the ion current produced. Fragment ions, which have excess kinetic energies, are not extracted with the same efficiency as the parent ion [5] and in order to account for this discrimination an additional correction procedure has been developed in our laboratory [4].

This correction is based on a study of the discrimination in our ion source and mass spectrometer by computer simulations (using the SIMION program [7]) of the electrical field distribution and the corresponding ion trajectories. The calculations show strong discrimination effects in the extraction characteristics of fragment ions with kinetic energies. Trajectories of ions with starting angles larger than a specific maximum angle are being lost at one of the electrodes. This maximum angle is strongly dependent on the initial kinetic energy of the ion. For the calculated maximum angle as a function of kinetic energy from 0 to 10 eV see Ref. [8]. The strongest dependency of the maximum angle on the kinetic energy is in the regime between thermal and 2 eV which is a typical energy range for fragment ions. In order to correct measured ion currents and ratios which are the basis for the partial cross section determinations it is neceserry to define an extraction coefficient being the ratio of the extracted ions and the ions produced in the ion source. Knowledge of the extraction coefficient dependence on the kinetic energy of the ions may be used to correct measured fragment ion currents if the kinetic energy of fragment ion under consideration is known. For the determination of these energies a simple method using the same experimental set-up has been devised in our laboratory [4]. The kinetic energy may be determined from the relation $E_{kin} \sim [U_{FWHM}]^2$ where the U_{FWHM} is the half-width at full maximum of the measured ion beam profile in z direction. This relationship has been confirmed later [8] by plotting measured U_{FWHM} for fragment ions of ethane, propane and H_2 fragment ions versus determined kinetic energies [9,10]. Moreover, in the present study we have developed a new method to obtain the kinetic energy distribution of the fragment ions produced by employing a kind of MIKE scan method.

Using this ion beam deflection technique and extraction/correction procedure described above, we have determined (besides relative cross sections differential in kinetic energy) relative partial ionization cross section functions from threshold to 1000 eV for the production of CH_4^+, CH_3^+, CH_2^+, CH^+, C^+, H_2^+,H^+ from methane. Absolute partial ionization cross section function for these ions were obtained by charge weighted summing of all observed partial ionization cross sections at 80 eV and by normalizing this sum to the absolute total ionization cross section (summation method [6]) reported by Straub et al [11].

The present results are shown together with earlier determinations in Fig.1. Besides very good agreement in the relative shape of all of the partial (and total) cross sections between the present data and the data of Straub et al and Tian et al. [11,13] (which are the most recent ones and considered to be also very accurate), there exists also quite good agreement for the absolute cross section values.

In conclusion it is worth noting that using the present double focusing mass spectrometer it is (as already demonstrated also earlier [8]) possible to determine partial cross sections in good agreement with results obtained using a time-of-flight mass spectrometer with a position sensitive detector whose output demostrates that all product ions are completely collected [11]. Based on this success we have recently extended this study to other hydrocarbon gas targets (e.g., C_2H_2, C_2H_4,) thereby producing data (partial and total cross sections, kinetic energy release distributions of fragment ions that is cross sections differential in kinetic energy of these fragment ions) not only of fundamental interest but also of importance for modelling plasma edge behavior in high temperature plasmas.

Acknowledgements

This work has been carried out within the Association EURATOM-ÖAW. The content of the publication is the sole responsibility of its publishers and it does not necessarily represent the views of the EU Commission or its services. It was partially supported by the FWF and ÖAW, Wien, Austria and the European Commission, Brussels (network programme).

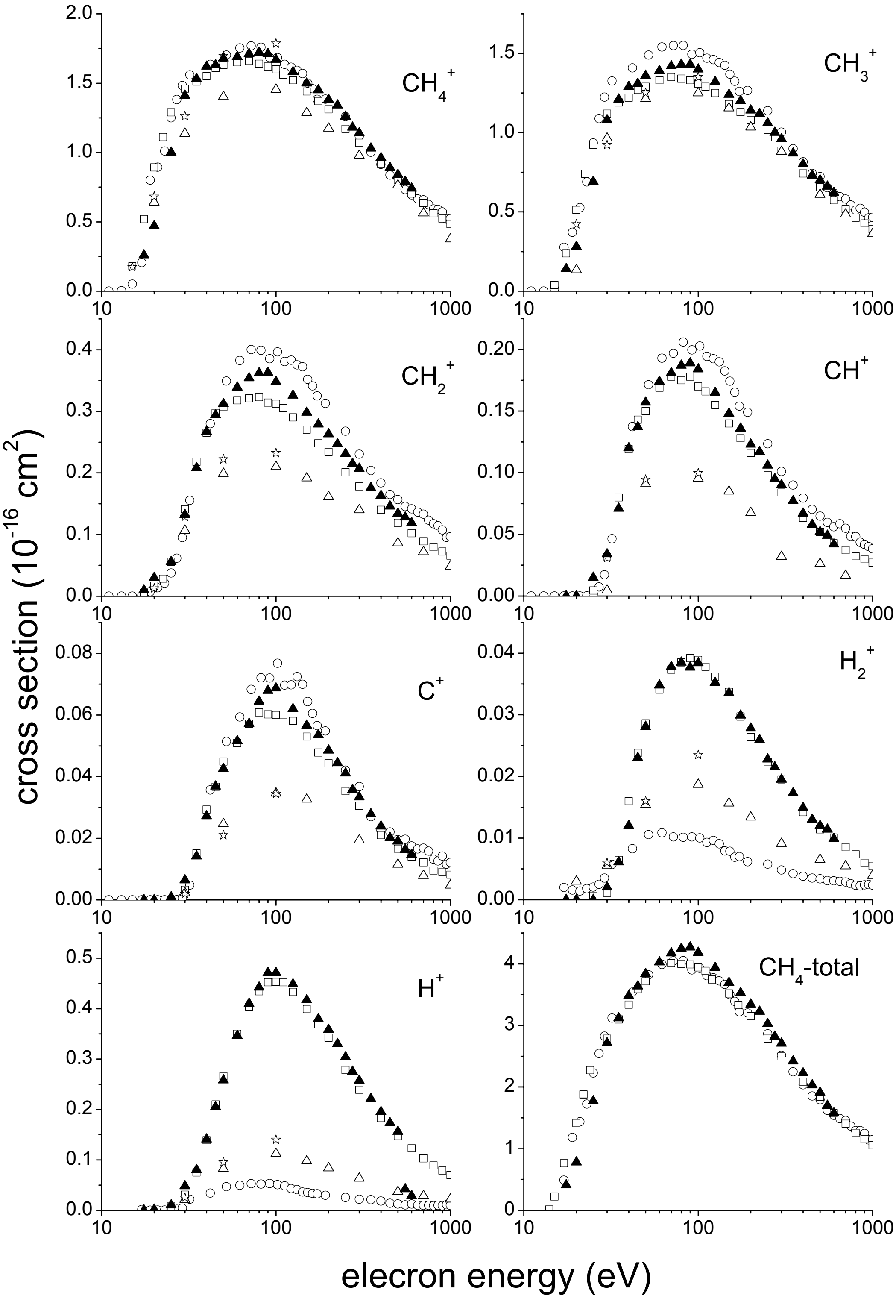

Fig 1. Present partial and total electron impact ionization cross sections (designated by ○) together with the results of Straub *et al* (Ref.11) (□), Chathan *et al* (Ref. 12) (★), Adamczyk et al (Ref.13) (Δ) and C. Tian et al (Ref.14) (▲).

References

[1] L.H. Toburen, Y. Hatano, Z. Herman, T.D. Märk, S. Trajmar and J.J. Smith, IAEA-TEC DOC, 506 (1989)23.

[2] H. Tawara, Y. Itikawa, H. Nishimura, H. Tanaka and Y. Nakamura, Research Report, NISF DATA6, Nagoya 46401, Japan, 1990.

[3] K. Stephan, H. Helm and T.D. Märk, *J. Chem. Phys.* **73** (1980) 3763.

[4] H.U. Poll, C. Winkler, V. Grill, D. Margreiter and T.D. Märk, *Int. J. Mass Spectrom. Ion Processes* **112** (1989) 209.
[5] K. Stephan, H. Deutsch and T.D. Märk, *J. Chem. Phys.* **83** (1985) 143.
[6] Märk T. D., Dunn G.H.: Electron impact ionization. Wien, Springer 1985 Chap.5 and 8.
[7] SIMION, Version 3.0, Idaho National Engineering Lab., EG&G, Idaho Inc., Idaho Falls, ID 83415, 1987.
[8] V. Grill, G. Walder, P. Scheier, M. Kurdel, T.D. Märk, *Int. J. Mass Spectrom. Ion Processes* **129** (1993) 31.
[9] R. Fuchs and R. Taubert, *Z. Naturforforschg. Teil A* **19** (1965) 1464.
[10] K. Köllmann, *Int. J. Mass Spectrom. Ion Phys.* **17** (1975) 261.
[11] H.C Straub, D. Lin, B.G. Lindsay, K.A. Smith and R.F. Stebbings, *J. Chem. Phys.* **106** (1997) 4430.
[12] H. Chathan, D. Hols, R. Robertson and A. Gallagher, *J. Chem. Phys.* **81** (1984) 1770.
[13] B. Adamczyk, A.J.H. Boerboom, B.L. Schram and J. Kistemaker, *J. Chem. Phys.* **44** (1966) 4640.
[14] C. Tian and C.R. Vidal, *J. Phys. B: At. Mol. Opt. Phys.* **31** (1998) 895-909.

Comparison of VOC measurements in Nashville, TE, during the Southern Oxidants Study (SOS) 1999

W. Grabmer[1], A. Wisthaler[1], A. Hansel[1], C. Stroud[2], J.M. Roberts[2], and F.C. Fehsenfeld[2]

[1] *University of Innsbruck, Technikerstrasse 25, Innsbruck A-6020, Austria*
[2] *Aeronomy Laboratory, NOAA, 325 Broadway, Boulder, CO 80303, United States*

Abstract

During the Southern Oxidants Study (SOS) 1999 Nashville campaign ambient air samples were analyzed at Cornelia Fort Airport (CFA) for organic compounds by two independent methods: 1) a gas chromatographic systems operated by NOAAs Aeronomy Laboratory, which performed immediate analysis of collected samples and 2) an in situ proton transfer reaction mass spectrometer (PTR-MS) system operated by the University of Innsbruck. The sample protocols were quite different for the different methods. The GC system sequentially collected and analyzed air samples each 60 minutes for VOCs. The in-situ PTR-MS system measured more than 20 VOCs on a time shared basis for 5 to 15 seconds respectively, once each 5 minutes. The PTR-MS system is not able to distinguish between isobaric species, therefore acetone and propanal (MVK and MACR) values measured by NOAAs GC were added up prior to comparison with the respective PTR-MS values. For all species mentioned above the different measurement methods show good agreement. In Figures 1 and 2 Isoprene and MVK&MACR values are shown.

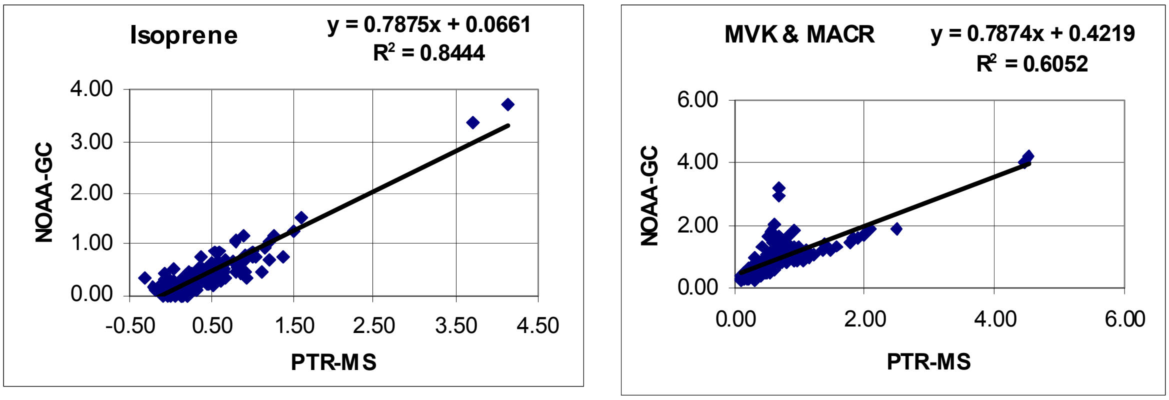

Figure 1: Scatter plots of coincident PTR-MS and GC measurements for isoprene and MVK & MACR for the time period June 18 – June 29 obtained during SOS 99 in Nashville, TE.

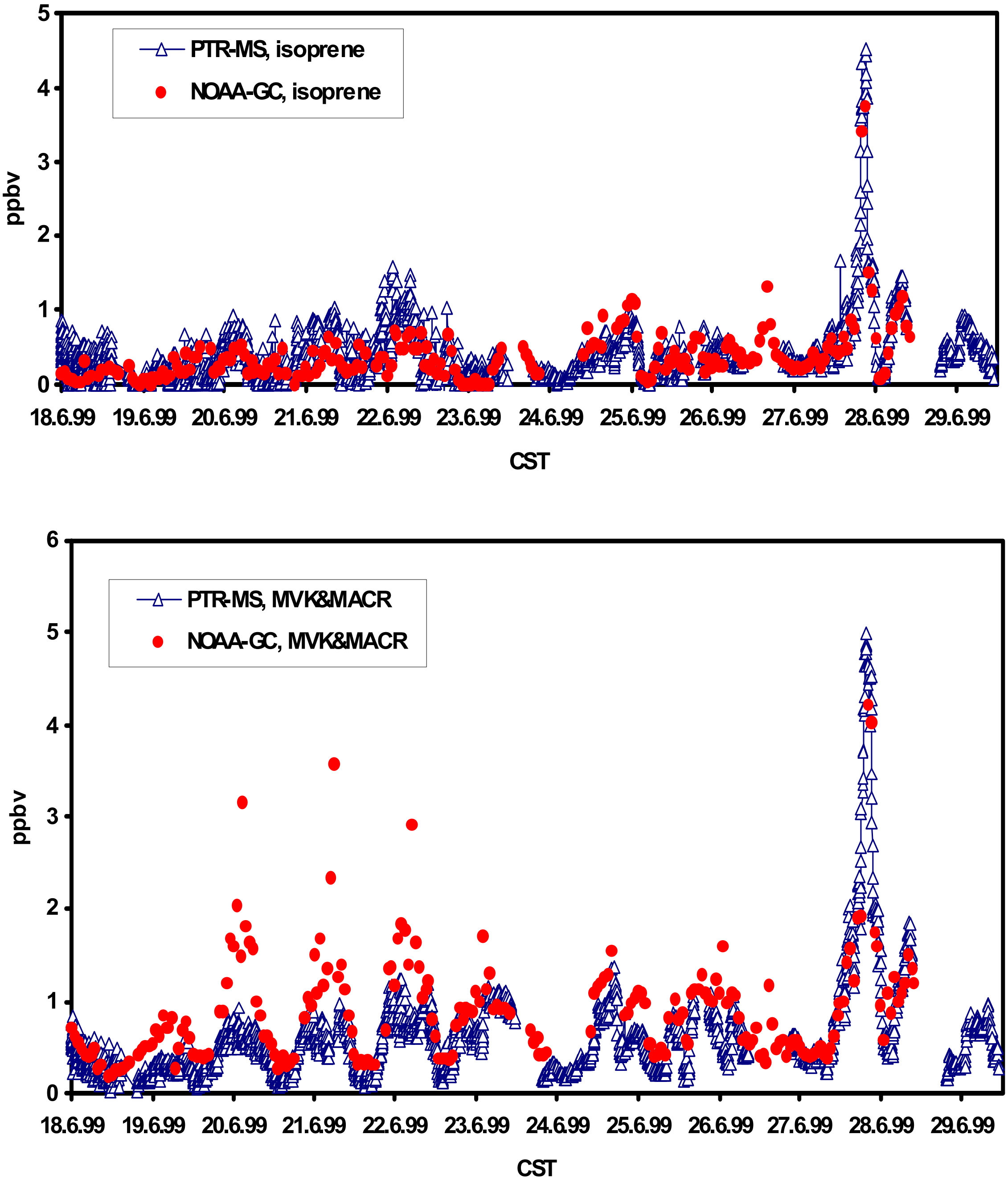

Figure 2: Synoptic variations for isoprene and its photooxidation products MVK & MACR for the time period June 18 to June 29 as observed at Cornelia Fort Airport in Nashville TE, during SOS 99. Open triangles represent in-situ PTR-MS results, full circles; NOAAs GC measurements.

In-Mouth Coffee Aroma: Breath-By-Breath Analysis of Nose-Space by PTR-MS While Drinking Coffee

Martin Graus[1*], Chahan Yeretzian[2], Alfons Jordan[1], Werner Lindinger[1]

[1]Institut für Ionenphysik, Leopold-Franzens-Universität Innsbruck,
Technikerstraße 25,A-6020 Innsbruck, Austria
[2]Nestlé Research Center, P.O. Box 44, CH-1000 Lausanne 26, Switzerland

Abstract

PTR-MS combined with a fast response inlet-system was used to investigate breath-by-breath the evolution of the in-mouth coffee aroma. The time-intensity profiles of a series of 14 masses were monitored on-line. From an analytical perspective, the purpose of this contribution is to demonstrate the potential of PTR-MS for real-time nose-space analysis. From a flavour science perspective, we wish to examine possible differences between orthonasal and retronasal aroma profile and document temporal changes of the retronsal profile, while coffee is kept in the mouth.

Introduction

An objective of coffee flavour research is to find chemical quality markers for a coffee brew, which correlate with the sensory assessment of expert coffee tasters and which drive consumer preferences. Currently the majority of analytical investigations on coffee aroma are performed under equilibrium or dynamic headspace conditions. The volatile flavour compounds are either stripped by a flow of gas or extracted with solvents to be subsequently analysed by gas chromatography. While this has been extremely valuable to expedite our understanding of coffee aroma, one might wonder how well this reflects the coffee aroma profile as it is experienced during the actual situation of coffee consumption. Coffee drinking conditions have additional important factors such as mixing, mastication and salivation, heating and interactions with mouth mucousa. This can lead to significant alterations of the physical and chemical state of its constituents (e.g. melting, emulsification, adsorption) induce chemical transformations, and modify the release of volatile flavour compounds relative to headspace (HS) studies.

Here, we discuss some new developments of nose-space analysis. We present a method to sample and analyse on-line volatile organic compounds (VOC) directly released from humans through the nose when consuming food [1-4]. The main benefit of on-line nose-space analysis is the ability to investigate the aroma during the actual situation of consumption. We present a novel approach to breath-by-breath analysis of volatiles exhaled through the nose based on Proton-Transfer-Reaction Mass-Spectrometry (PTR-MS). First we outline the method and then go on presenting breath-by-breath nose-space results on a series of volatile coffee compounds.

Nose-Space Analysis

The aroma (odour) of food products is related to VOCs that are released from foods and reach the olfactive epithelium in the upper part of the nose. When flavour active compounds interact with olfactive receptors, a sensory perception is triggered. VOCs can reach the olfactory epithelium from two distinct directions. Either they are sniffed directly through the nose, via the orthonasal pathway, or they reach the olfactive receptors through the oral cavity and the pharynx, via the retronasal pathway. The orthonasal aroma corresponds to an aroma, as it is perceived from a food held in front of the nose (sniffing). In contrast, the retronasal aroma corresponds to the aroma of a food, as it is perceived during food consumption (while drinking or eating). Nose-space analysis samples the air exhaled through the nose as food is

---

[*] Corresponding author: martin.graus@uibk.ac.at

being consumed and reflects the retronasal aroma composition. Hence by comparison of a HS VOC profile with a nose-space profile, we address the question how closely a HS profile reflects the odor of food being consumed.

The first real-time breath-by-breath analysis dates back to 1988 [5]; a recent review discussed the various methods for nose-space (in-vivo) analysis [6].

Experimental

Nose-space analysis aims at sampling and analysing the air exhaled through the nose while food is being consumed. For this, nose-space air is sampled via two glass tubes fitted into the nostrils (see Figure 1). The separation and diameter of the tubes are adapted in order to allow the person to breathe and eat freely. The air from both tubes is combined and a small fraction of the nose-space air (15 sccm/min analysis flow plus 15 sccm/min bypass flow) is sampled and introduced into the drift-tube of the PTR-MS. The nosepiece is heated to 38°C to prevent condensation on the glass tubes.

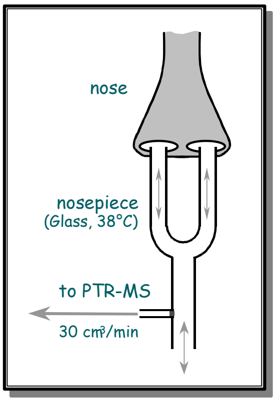

***Figure 1**: Nosepiece. The air exhaled during food consumption is sampled via the nosepiece and a small fraction introduced into the PTR-MS for on-line VOC analysis.*

The PTR-MS technique has been extensively discussed in a series of review papers [7-10]. Briefly, it combines a soft, sensitive and efficient mode of chemical ionisation (CI), adapted to the analysis of trace VOCs, with a mass filter. In this study, 15 sccm/min gas is continuously introduced into the CI-cell (drift-tube). The drift-tube contains besides buffer gas a controlled ion density of H_3O^+. VOCs that have proton affinities larger than water (proton aff. of H_2O: 166.5 kcal/mol) are ionised by proton transfer from H_3O^+, and the protonated VOCs are mass analysed.

Results

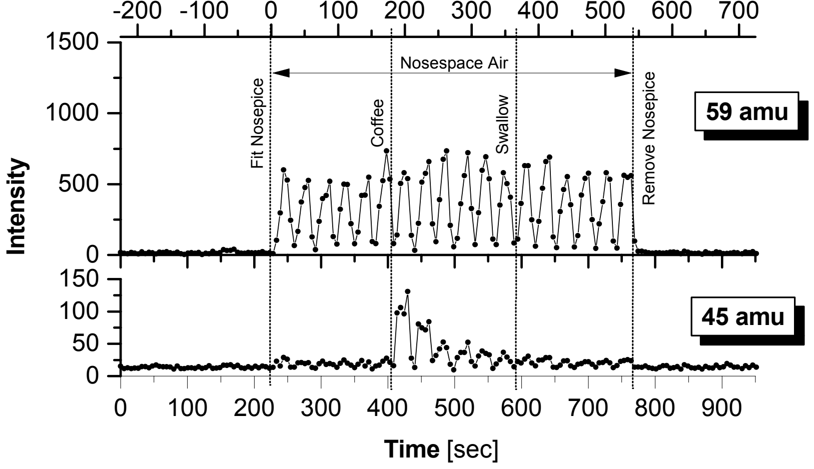

***Figure 2**: PTR-MS time-intensity profiles of VOCs during a typical nose-space experiment with coffee brew, for two selected masses - 59 and 45 amu. The experiment can be divided into five consecutive phases. First indoor air was sampled through the nosepiece in order to assess contributions from the laboratory background. We then measured the VOC composition of human breath during six consecutive breathing cycles, with the nosepiece being inserted into the nostrils, but without having coffee in the mouth. After approximately 410 sec, 5 ml coffee at 50°C were taken into the mouth and the nose-space air sampled for six additional breathing cycles, after which the coffee was swallowed and further six cycles monitored. At the end of the experiment, the nosepiece was removed from the nostrils and the indoor-air measured again. During the experiment, the nosepiece was heated to 38°C to avoid condensation.*

As a starting point of the study, the HS profile of a coffee brew was measured by stripping the brew with indoor air. The coffee was prepared as follows. Using a standard coffee filter machine, 25 gram of roast&ground coffee was extracted with 500 ml water (Vittel 'Bonne Source'). 265 ml of the brew were put into a stripping vessel and the VOCs were stripped at

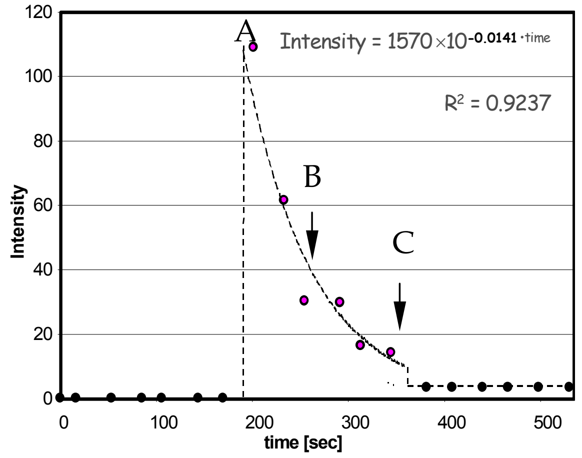

***Figure 3**: Exponential fit-curve to the intensity decrease of mass 45 as a function of time. Time zero was set at the moment where the nosepiece was put into the nostrils. Furthermore, we subtracted the averaged intensity originating from the human breath and the indoor-air from the raw data. Hence the intensity prior to taking coffee in the mouth is zero. Once coffee is taken into the mouth, the intensities at masses corresponding to coffee volatiles increased initially abruptly, but then decreased gradually as coffee was kept in the mouth. In order to assess quantitatively this decrease, we determined the maximum intensities at the individual breathing cycles and fitted an exponential function through these points. Once the coffee was swallowed, the nose-space intensities dropped to a value close to the one prior to taking coffee into the mouth.*

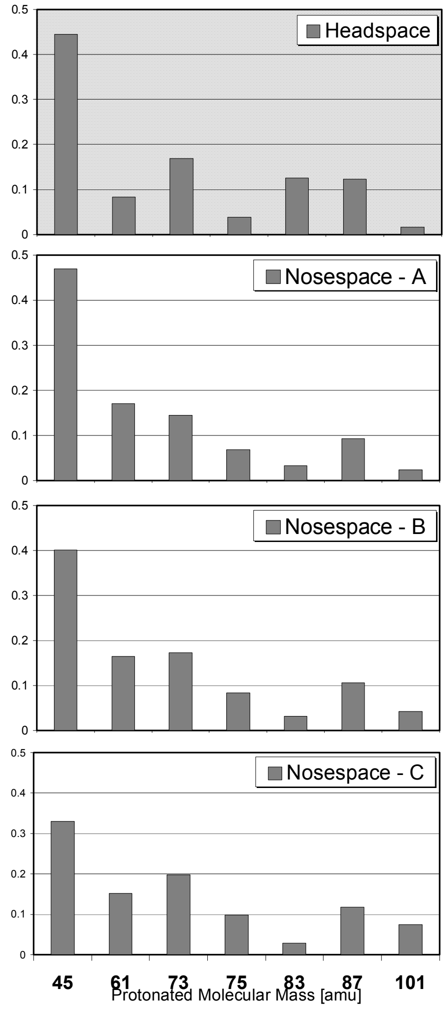

***Figure 4**: The top two frames allow comparing the orthonasal to the retronasal volatile profile. They are quite distinctive, indicating that traditional HS analysis might not reflect accurately the volatile profile, as it is experienced by consumer. The three bottom frames illustrate the evolution of the nose-space profile with time. A significant change with time is observed.*

36 °C with an airflow of 15 sccm/min through the liquid for a period of one hour. The VOCs in the stripped gas were measured by PTR-MS. This spectrum represents an orthonasal reference profile to be compared with the retronasal data discussed below.

The brew used for the nose-space experiments was prepared similarly to the brew for the HS experiments. In order to minimize the experimental variability, a precise protocol was develop for the preparation and drinking of the coffee. A series of time-intensity profiles were taken by recording the intensities of a series of 14 masses using PTR-MS. The temporal course is shown in figure 2.

Discussion

The most striking observation of the nose-space time-intensity profiles is the strong decreases of signal intensity with time, while the coffee is kept in the mouth. In order to quantify the decrease we fitted an exponential decay curve through the maxima of the individual breathing peaks for each individual mass and determined the exponent, as shown for mass 45 in Figure 3.

Several processes can in principle be responsible for this decrease. One is stripping of volatiles from the liquid coffee. Based on measured partition coefficients and stripping experiments [11], we have to conclude that the observed decrease (exponents) is at least one order of magnitude too fast than can be explained by a simple volatile stripping argument. In fact, we observe for mass 45 (as well as for the others) a decrease of nose-space intensity by more than 50% within 2 min. In contrast, we measured reduction by just a few percent when stripping a liquid or a coffee solution with 100 sccm air for about 5 min. Hence this can only account for a marginal contribution to the decrease of nose-space intensity.

Two other reasons for the fast decrease of VOCs in the nose-space can be put forward. (i) Diffusion of VOCs into the mouth mucosa will deplete the liquid coffee phase from volatiles, and hence reduce their nose-space concentrations. These compounds can be released back from the mucosa into the mouth-space once the coffee is swallowed and contribute to the lasting coffee-odour in the mouth. Currently we can hardly assess the quantitative importance of this effect, although experiments by Buettner et al. have shown that this can be quit significant [12,13]. (ii) The coffee that is taken into the mouth has a temperature of 50°C. Once in contact with the mouth tissue, the liquid starts to cool down and eventually reach 37°C. In a separate study we measured the temperature dependence of the partition coefficient for a series of coffee volatiles [14] and found that this phenomena can account for a significant if not for most of the decrease of the nose-space concentration. Quantitative studies are on the way to assess the relative contributions to the decrease of nose-space concentration with time.

Since we determined the exponents for the individual masses (Figure 3), we can calculate the volatile profile in the mouth as a function of time and follow the evolution of the mouth/nose-space. This is shown in Figure 4 for three selected times. The three bottom frames show the nose-space profiles for 0 (A), 85 (B) and 170 (C) sec after taking the coffee into the mouth. The frame Nosespace A corresponds to the nose-space profile as the coffee was just taken into the mouth. The spectra are normalised on the sum of the selected masses' intensities. While the coffee is kept in the mouth we can distinguish intensity changes that occur with time. This demonstrates at an analytical level and based on just a few selected compounds that the volatile profile is evolving rapidly in the mouth. It also suggests that a dynamic description of flavour might be more relevant to the situation of consumption than a static HS profile.

The top frame shows the intensities of the orthonasal profile (HS) at the same masses as for the nose-space at time zero, just below. Comparing both profiles, we see that they are distinctively different. This implies that the orthonasal HS profile is not an accurate description of the volatile profile as perceived during consumption.

Conclusions

The objective of this study was twofold. From an analytical perspective, we wanted to establish a nose-space method based on PTR-MS. From a flavour perspective we addressed two specific questions. First we wanted to assess the relation between the orthonasal and retronasal volatile profile. Second we were interested to see whether and how fast the retronasal volatile profile evolves with time.

Based on the results presented in this study, we believe that we have established a powerful approach that combines nose-space sampling with PTR-MS, to monitor at high time resolution the nose-space volatile profile. Considering flavour aspect, we have observed a fast exponential decrease of nose-space volatile intensities. For all VOCs discussed here, the intensities decreased by more than 50% within the two minutes of keeping coffee in the mouth. While several physical phenomena can contribute to this fast decrease, the most significant is probably the cooling of the coffee from the starting 50°C to 37°C in the mouth, although absorption on the mouth mucousa might also be important. More quantitative studies are needed to ascertain the relative contributions. The other flavour aspect is the comparison of the orthonasal (HS) with the retronasal volatile profile. This work revealed important differences between both profiles, documenting the value of analysing coffee flavour under conditions close to the situation of consumption.

Hence these first results, based on a limited number of volatile compounds, have demonstrated significant differences between orthonasal and retronasal volatile profiles and revealed strong changes of the nose-space profiles while coffee is kept in the mouth. Further studies are on the way to extend these findings.

Acknowledgement

We thank D. Roberts for advise and support, and acknowledge P. Pollien, A. Hansel and T.D. Märk for stimulating discussions.

References

---

[1] Linforth, R.S.T., Savary, I.; Pattenden, B.; Taylor, A.J. *J. Sci. Food Agric.,* **,** 65, 241-247 **(1994)**

[2] Ingham, K.E.; Linforth, R.S.T.; Taylor, A.*J. Food Chem.*, 54, 283-288 **(1995)**

[3] Linforth, R.S.T. and Taylor, A.J. European Patent EP 0819 937 A2 **(1998)**

[4] Taylor, A.J.; Linforth, R.S.T. In *Flavor Release*: Roberts, D.D. and Taylor A.J., Eds.; American Chemical Society: Washington, D.C., pp. 8-21 **(2000)**

[5] Seoting W.J., Heidema J., *Chem. Senses*, 13, 607-617 **(1988)**

[6] Taylor, A.J.; Linforth, R.S.T. In *Flavor Release*: Roberts, D.D. and Taylor A.J., Eds.; American Chemical Society: Washington; pp. 8-21 **(2000)**

[7] Yeretzian C., Jordan A., Brevard H., Lindinger W.; 218th ACS National Meeting on Flavor Release: Linking Experiments, Theory and Reality, New Orleans, Roberts D., Taylor A.J., Eds.; American Chemical Society: Washington pp. 8-21 **(2000)**

[8] Lindiger W., Hansel A., Jordan A.; *Int. J.Mass Spectrometry, Ion Processes,* 173, 191-241 **(1998)**

[9] Lindiger W., Hansel A., Jordan A.; *Chemical Society Review* 27, 237-354 **(1998)**

[10] Hansel A., Jordan A., Holzinger R., Prazeller P., Vogel W., Lindinger W.; *Int. J.Mass Spectrometry, Ion Processes*, 149/150, 609-619 **(1995)**

[11] Pollien P., Yeretzian C.; at the 19th International Conference on Coffee Science (ASIC 2001); 14-18 May 2001, Trieste, Italy; **(2001)**

[12] Buettner A., Beer A., Hannig C., Settles M., Schieberle P.; ACS Symp. Ser. 2001, on *Flavour chemistry and heteroatomic compounds*; T. Reineccius T., Reineccius G., eds; in press.

[13] Buettner A., Schieberle P.; *Food Chemisty* 71, 347-354 **(2000)**

[14] Karl T., Yeretzian C., Jordan A., Lindinger W.; *Int. J.Mass Spectrometry, Ion Processes*, submitted

High resolution multiple electron impact ionization of helium, neon, argon, krypton and xenon atoms close to threshold: appearance energies and Wannier exponents

B. Gstir, M. Rümmele, T. Fiegele, G. Hanel, S. Denifl, M. Stano[1], L. Feketeova[1], P. Scheier, K. Becker[2] and T.D. Märk[3]

Institut für Ionenphysik, Leopold-Franzens Universität, Innsbruck, Austria

[1] *Dept. Plasma Physics, Comenius University, SK-84248 Bratislava, Slovakia*
[2] *Department of Physics, Stevens Institute of Technology, Hoboken, NJ, 07030, USA*
[3] *Also: Adjunct Professor, Dept. Plasma Physics, Comenius University, SK-84248 Bratislava, Slovakia*

Abstract

We report the results of the experimental determination of the appearance energies (AEs) for the formation of multiply charged Ne^{n+} (up to n = 4), Ar^{n+} (up to n = 6) and Xe^{n+} (up to n = 8) and its fragments in a crossed-beam apparatus. The data analysis uses the Marquart-Levenberg Algorithm (MLA), which involves an iterative, non-linear least-squares fitting routine, in conjunction with either a 2-function or a 3-function fit based on the Wannier threshold law. The values of the AEs determined in this work and the extracted exponents are compared with other available data and with the predictions of the Wannier model. We will also present recent data on multiple ionisation of He and Kr.

Introduction

The ionisation of the rare gases He, Ne, Ar, Kr and Xe by electron impact is an important process in collision physics from a basic viewpoint. The energy dependence of the ionisation cross sections near the ionisation threshold is a complex many-body process whose rigorous quantum mechanical treatment is difficult, in particular in the case of a multiple ionisation process involving. The electron impact ionisation of rare gas atoms is also an important process in high-energy chemical processes e.g. in planetary atmospheres, pulsed power switching and gaseous dielectrics.

Experimental

The apparatus used in the present experiments has been described in detail in a previous publication [1]. Briefly, we used a molecular beam source in conjunction with a hemispherical electron monochromator (typical FWHM energy resolution 30 - 100 meV), a commercial quadrupole mass spectrometer, a deflector and a channeltron for detection. The target gas under study is injected directly into the collision chamber, so that higher target gas densities (corresponding to partial rare gas pressures of 10^{-5} – 10^{-6} Torr) can be achieved in the interaction region.

Results

3.1. Appearance energies of the rare gases Ne, Ar and Xe

The appearance energies extracted from our measured data sets using a fit function based on Wannier type power threshold law $\sigma(E) = (E - E_0)^n$ for the formation of Ne^{n+} (n = 1...4), Ar^{n+} (n = 1...6) and Xe^{n+} (n = 1...8) ions are summarised in Tables 1 to 3 and are compared to other available data including spectroscopically obtained AEs [2] and experimentally determined values obtained using a variety of other methods [3-7].

Ion	Spectroscopic Value [2]	Stuber [3]	Redhead [4]	This work
Ne^+	21.56	21.56	21.6	21.6±0.15
Ne^{2+}	62.53	62.50	62.6	62.6±0.10
Ne^{3+}	125.98	129.00	125.6	125.8±0.50
Ne^{4+}	223.09	246.00	219.6	226.2±4.50

Table 1: AEs in eV for multiply charged Ne^{n+} ions in comparison with other measured or calculated AEs (eV).

Ion	Spectroscopic Value [1]	Stuber [3]	Gerdom et al. [5]	Redhead [4]	Syage [6]	This work
Ar^+	15.759	---	---	---	---	15.76±0.01
Ar^{2+}	43.388	43.0	43.95±0.67	42.8	---	43.36±0.02
Ar^{3+}	83.14	85.0	84.50±0.88	80.8	84	84.3±0.4
Ar^{4+}	143.94	147.0	---	135.8	148	144.0±1.5
Ar^{5+}	218.96	285.0	---	208.8	225	222.5±3.7
Ar^{6+}	309.97	430.0	---	297.8	---	328.0±3.7

Table 2: AEs in eV for multiply charged Ar^{n+} ions in comparison with other measured or calculated AEs (eV).

Ion	Spectroscopic value [2]	Dorman et al. [7]	Stuber [3]	Redhead [4]	Syage [6]	This work
Xe^+	12. 13	12.1	12.1	12.1	---	12.1±0.01
Xe^{2+}	33.34	33.5±0.2	33.0	32.1	---	32.2±0.6
Xe^{3+}	65.40	64.8±0.5	65.0	61.1	64	61.8±2.6
Xe^{4+}	---	107.0±1.0	110.0	101.1	104	107.4±0.8
Xe^{5+}	---	160.0±1.0	172.0	152.1	166	160.8±3.7
Xe^{6+}	---	218.0±1.0	248.0	216.1	230	234.6±2.7
Xe^{7+}	---	---	362.0	308.1	---	355.2±3.8
Xe^{8+}	---	---	535.0	413.3	---	(545.6±11)

Table 3: AEs in eV for multiply charged Xe^{n+} ions in comparison with other measured or calculated AEs.

In the case of Ne, the agreement between the various sets of AE values is quite satisfactory except perhaps for the values of Stuber [3] whose AE values for Ne^{3+} and Ne^{4+} are significantly higher than all other reported data.

For Ar we are in good agreement with the spectroscopic values given by Rosenstock et al. [2] except for Ar^{6+}. Compared to the other electron impact results our values are much lower especially in the case of higher charged ions.

The situation in Xe is even less satisfactory. While Xe has been investigated more thoroughly than any other rare gas, there are discrepancies that exceed the quoted uncertainties already for the various reported values of AE for Xe^{3+}, where the highest reported AE lies 5 eV above the lowest reported value.

3.2. Exponents of the rare gases Ne, Ar and Xe

The exponents n extracted from our measured data sets for the formation of Ne^{n+} (n = 1 – 4), Ar^{n+} (n = 1 – 6) and Xe^{n+} (n = 1 – 8) ions are summarised in Table 4 and are also compared to other available data including predictions following the signal ideas of Wannier [8] for n = 1 – 4, and several experimentally determined values [9,10,11].

Ion	Wannier-Geltman	Generalized Wannier	Lebius et al. [9,10]	This work
Ne^{+}	1	1.127	1.06±0.05	1.24±0.01
Ne^{2+}	2	2.270	2.04±0.07	1.99±0.02
Ne^{3+}	3	3.55	3.16±0.1	3.21±0.05
Ne^{4+}	4	> 4.70	4.15±0.15	3.28±1.07

Ion	Wannier-Geltman	Generalized Wannier	Statistical approach	Koslowski et al. [11]	This work
Ar^{+}	1	1.127	---	---	1.40±0.2
Ar^{2+}	2	2.27	1.86	2.6 (2.0)	2.00±0.3
Ar^{3+}	3	3.5	2.89	3.0 (1.7)	2.75±0.5
Ar^{4+}	4	> 4.7	---	2.5	3.15±0.9
Ar^{5+}	5	> 4.7	---	---	4.01±1.4
Ar^{6+}	6	> 4.7	---	---	3.89±1.4

Ion	Wannier-Geltman	Generalized Wannier	Statistical approach	Lebius et al. [20,21]	This work
Xe^{+}	1	1.127	1.13	1.13	1.33±0.05
Xe^{2+}	2	2.27	1.83	1.85±0.1	2.17±0.14
Xe^{3+}	3	3.5	2.82	2.80±0.14	2.28±0.15
Xe^{4+}	4	> 4.7	3.70	2.62±0.26	3.05±0.06
Xe^{5+}	5	---	---	---	3.54±0.11
Xe^{6+}	6	---	---	---	3.46±0.10
Xe^{7+}	7	---	---	---	2.39±0.06
Xe^{8+}	8	---	---	---	(1.18)

Table 4: Exponent n for multiply charged Ne^{n+}, Ar^{n+} and Xe^{n+} ions in comparison with results of other groups.

In Ne, there is satisfactory agreement between our values and those from Lebius et al. [9] for Ne^{2+} and Ne^{3+}, whereas the agreement between the two experimentally determined exponents is less satisfactory for Ne^{+}. In the case of Ne^{4+}, both experiments are lower than the Wannier prediction. In the case of Ar, except for Ar^{+}, our exponent is again much lower.

In case of Xe, the present values for Xe^{+} is slightly larger than the Wannier prediction as well as the data of Lebius et al. [9, 10] and Russek [12], which both agree well with the Wannier exponent of 1.127. For Xe^{2+} our "n" value is consistent with the Wannier prediction and as the charge state of the Xe ion increases, all experimental values fall below the corresponding Wannier prediction.

Summary

The values of the AEs determined in this work when compared with other available experimental and spectroscopic values of the AEs reveal generally good agreement for charge states n < 4, but few, if any, systematic trends can be found for the experimentally determined

AEs for the formation of more highly charged ions. This is a reflection of the fact that the reliable experimental determination of AEs for such ions is very difficult.

The level of agreement between our extracted exponents “n” in a power law when compared with other available experimental data and the predictions of *n*-th power Wannier-Geltman and the generalized Wannier law is generally good only for very low charge states, n=1 and 2. Significant discrepancies were found for larger values of n. One observation, however, is particularly, noteworthy, namely the fact that none of the available experimental data seems to support the large values of “n” predicted by the Wannier-Geltman and the generalized Wannier law for $n > 2$. This might indicate that the extension of these threshold laws to the formation of highly charged ions, for which it was not originally derived, may be questionable. We are presently extending these studies to He and Kr and we are in particular revisiting charge state n = 1 and 2 under very high resolution conditions in order to confirm discrepancies between experimental values and theoretical predictions for the exponent in the threshold power law.

Acknowledgements

This work has been carried out within the Association EURATOM-ÖAW. It was partially supported by the FWF, Austria and by the European Commission, Brussels.

References

---

[1] D. Muigg, G. Denifl, A. Stamatovic and T.D. Märk, *Chem. Phys.* **239** (1998) 409
[2] H.M. Rosenstock, K. Draxl, B.W. Steiner and J.T. Herron, “Energetics of Gaseous Ions”, *J. Phys. Chem. Ref. Data* **Vol 6**, Suppl. 1 (1977)
[3] F.A. Stuber, *J. Chem. Phys.* **42** (1965) 2639
[4] P.A. Redhead, *Can. J. Phys.* **45**, (1967) 1791
[5] K. Gerdom, J. Puerta and K. Wiesemann, *J. Phys. B* **27** (1994) 747
[6] J. Syage, *Phys. Rev. A* **46** (1992) 5666
[7] F.H. Dorman and J.D. Morrison, *J. Chem. Phys.* **34** (1961) 1407
[8] G.H. Wannier, *Phys. Rev.* **90** (1953) 817
[9] H. Lebius, B.A. Huber, H.R. Koslowski and K. Wiesemann, *J. Phys., C1 suppl.1*, **50** (1989) 399
[10] H. Lebius, H.R. Koslowski, K. Wiesemann and B.A. Huber, *Ann. Physik*, **48** (1991) 103
[11] H.R. Koslowski, J. Binder, B.A. Huber and K. Wiesemann, *J.Phys. B*20 (1987) 5903
[12] A. Russeck, *Phys. Rev.* **132** (1963), 246

Low energy electron attachment to the uracil molecule

G. Hanel, B. Gstir, S. Denifl, P. Scheier, B. Farizon[a)], M. Farizon[a)], T.D. Märk

Institut für Ionenphysik, Universität Innsbruck, Technikerstr.25, A-6020 Innsbruck, Austria

[a)]Institut de Physique Nuclair, Universite Claude Bernard Lyon-1, 43 Bd du 11 Novembre 1918 Villeurbanne Cedex, France

Using a recently constructed high resolution crossed beams apparatus involving a hemispherical electron monochromator [1] we have studied electron attachment to the $C_4H_4N_2O_2$ molecule, better known as uracil.

The experimental set-up consists of a hemispherical electron monochromator, a supersonic nozzle expansion source and a quadrupole mass spectrometer. With this electron monochromator we can achieve an electron energy resolution of up to 30meV FWHM. Two different electron attachment studies one producing Cl^- from CCl_4 for the dissociative attachment processes and the other producing SF_6^- out of SF_6 was used to test the set-up and to determine the electron energy resolution. For the present measurements the determination of the electron energy distribution mainly was done by producing Cl^- from CCl_4. This process was additionally used to calibrate the energy scale. The electron energy range investigated was in the region between 0 and 12eV.

Because uracil at room temperature is a white powder we used a modified C_{60} oven to introduce evaporated uracil into the apparatus. The most important point in modifying this oven was to attach an about 7cm long copper pipe to the open side of the oven. This helped us to guide the evaporated uracil directly into the collision chamber. The inside diameter of this pipe is about 0.8 mm. A typical temperature range of the oven during operation of the measurements is 180 to 185°C. Approximately 2mm further the crossing of uracil and the monochromatized electron beam occurs. The ions produced are extracted by a weak electric field either produced by one part of the collision chamber or by the entrance cone optics of the quadrupole mass spectrometer. After passing the mass spectrometer the ions are deflected and counted in single ion count mode with a channeltron.

In addition to series of electron impact ionization studies (in order to determine the mass spectrum and to obtain apperance energies) we did measurements on electron attachment to the uracil molecule $C_4H_4N_2O_2$. It is the first such study concerning the attachment of free electrons to the uracyl molecule (see also the pioneering study about bound electron attachment to uracil by Schermann and co-workers [3]). The only comparable measurements have been carried out at the Berlin Laboratory of Illenberger and co-workers [2] where they investigated electron attachment to the 5-bromouracil molecule.

The main interest of this work is to find out what will happen when slow electrons are colliding with the cellular RNA compound uracil. It is generally considered that the types of primary damage in DNA by ionizing radiation (electrons, photons, ions) leads to the most significant biological effects [4]. These effects are known as double-strand breaks (DSB) and clustered lesions. These types of lesions have the greatest relevance of cellular effects underlying both human cancer risk from radiation exposure and the cell killing action of radiation used in radiotherapy.

In the present measurements the following anion fragments of uracil have been detected within our detection limit $(C_4H_3N_2O_2)^-$, OCN^-, $(H_2C_3NO)^-$, CN^-, O^-. The most important result is that we cannot observe within our detection efficiency any traces of the parent anion (this has been confirmed by careful measurements of neighboring isotope peaks). The most intense fragment anion appears on a mass to charge ratio of 111 amu. Mass 111 corresponds to a uracil molecule missing one hydrogen. Moreover, the electron attachment spectrum for this anion exhibits in the energy range from 0 to 3eV (see Fig.1) a number of resonant structures.

The zero energy resonance is probably due to an s-wave attachment process. Other observed resonances appear at 0.68, 1.0, 1.44, 1.7, and 1.92eV. The error bars for these peak energy values are in the region of about ±40 meV.

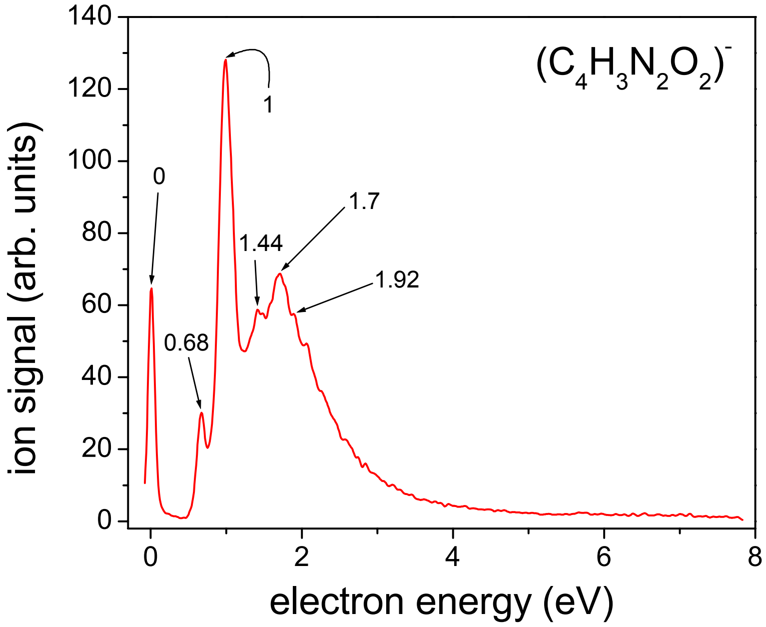

Fig. 1: Electron attachment spectrum for uracil producing the anion fragment $C_4H_3N_2O_2^-$.

It is interesting to note that this result, i.e. the missing of the parent anion is in contrast to recent observations by Schermann and co-workers [3], who observed the occurrence of the uracil parent anion when studying Rydberg electron attachment to gas phase isolated uracil molecules [3] and also in contrast to free electron attachment studies to bromouracil by Illenberger [2] who observed in these studies the parent bromouracil anion to be the major anion produced.

Another interesting observation is whereas the parent minus H anion is observed at zero electron energy, all other fragments do not appear in the zero energy range. The two most intense fragment anion species appear at mass 42 identified as OCN^- and at mass 68 identified as $(H_2C_3NO)^-$, the same fragment anions are also observed in [2]. In contrast to the measurements of Illenberger and co-workers [2] on the bromouracil, however, we see in addition the fragments CN^- and O^-. The intensity of these fragment anions is at least one order of magnitude lower than OCN^- yield. The onset of the first resonance for these anions appears at the relatively high electron energy of about 5eV for CN^- and at 9eV for the O^-, followed by two resonances with the maxima at approximately 7eV and 10eV for CN^- and in the case of the O^- production only one resonance at 10.2eV.

Acknowledgements

Work supported by the FWF, Wien, Austria, the Austrian-French Amadee program and the European Commission, Brussels.

References

[1] G. Denifl, D. Muigg, A. Stamatovic, T.D. Märk, *Chem. Phys. Lett.* **288** (1998) 105
[2] H. Abdoul-Carime, M. A. Huels, F. Brünik, E. Illenberger, *J. Chem. Phys.* **113** (2000) 2517
[3] C. Desfrancois, V. Periquet, Y. Bouteiller and J.P. Schermann, *J. Phys. Chem. A* **102** (1998) 1274
[4] B. Boudaiffa, P. Cloutier, D. Hunting, M.A. Huels and L. Sanche, *Science* **287** (2000) 165

Imaging the reactions of molecular dications: a new probe of dicationic reaction dynamics and energetics.

Sunny Wan-Ping Hu, Sarah M. Harper and Stephen D. Price

Chemistry Department, University College London, 20 Gordon Street,
London, UK. WC1H 0AJ

A. Overview

Small molecular doubly-charged ions (dications) are usually highly energy-rich and reactive metastable species.[1-3] However, despite their high internal energy content, several molecular dications have recently been shown to display considerable chemical reactivity with neutral species.[4-16] For example:

$$CF_2^{2+} + H_2 \rightarrow HCF_2^{+} + H^{+} \quad (1)$$

Initial studies of the chemical reactions of molecular dications were prompted by the mass-spectrometric observation of product channels from dication-neutral encounters which involved the formation of new chemical bonds.[10,17] Since these early observations many new chemical reactions between dications and neutrals have been documented. However, more detailed investigations of the dynamics of these reactions are scarce and restricted to pioneering angular scattering measurements in Prague[4,6,14] and studies of intermolecular and intramolecular isotope effects at UCL.[8,9,16] The angularly resolved data from Prague demonstrates the continued power of angularly resolved studies as a probe of ionic reaction dynamics. Hence, we have developed a new experiment which will generated angularly resolved data to probe the dynamics of dication chemical reactions. This new experiment does not use the traditional technique employing a rotatable angularly restricted detector. Instead we use the power of position sensitive coincidence (PSCO) experiments[18,19] to detect in coincidence both of the charged products from a dication chemical reaction. Such coincidence data should yield the initial velocity vectors of the charged products. From these vectors the complete kinematics of the reactive scattering process should be accessible. This poster will present the details of this new experiment and show that, as predicted, bimolecular position sensitive coincidence experiments provide a hugely detailed probe of the dynamics of dication reactions.

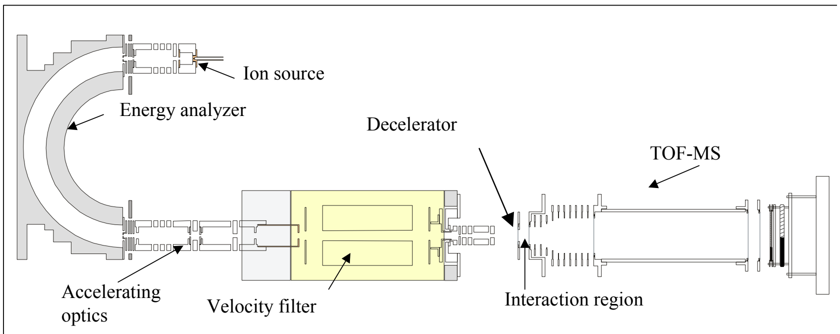

Figure 1 Schematic of the position sensitive coincidence spectrometer used to study dication reaction dynamics.

B. Experimental details

The position sensitive coincidence apparatus is illustrated in Figure 1. Briefly, a beam of ions is extracted from a home-built ion source. The translational energy, and energy spread, of the ions in the beam is controlled by a hemispherical energy analyser through which the beam passes. The reactant dications of interest e.g. CF_2^{2+} are selected from the ion beam and collide in the source region of a time-of-flight mass spectrometer (TOFMS) with the neutral reactant and the reactions of interest occur. We generate dication beams with excellent intensity and energy distributions. Typical beam currents are 1 pA at an energy of 4 eV in the source region with a translational energy spread of 0.1 eV. Following the interaction of the dication beam with the neutral target the ionic products are detected and analysed by pulsing an extraction voltage (30-50 kHz) in the source region of the TOFMS. The ions then fly down the TOFMS and are detected at a position sensitive detector interfaced to fast timing electronics. This position sensitive data can be interpreted to yield the initial velocity vectors of the two charged fragments from a dication reaction. From these velocity vectors the dynamics of the reaction can be determined. Experiments can be carried out with either a pulsed (~0.5 μs) or continuous beam of reactant dications. The pulsed beam produces higher quality data at the expense of longer run times.

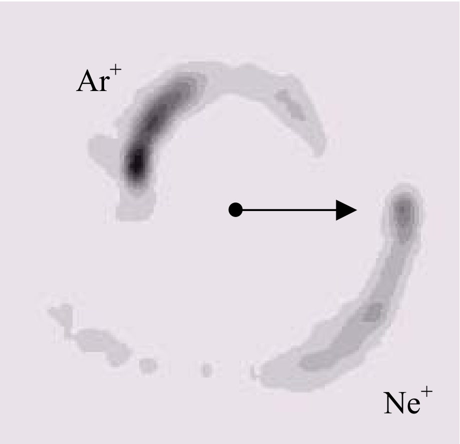

Figure 2 Scattering diagram from a PSCO spectrum of collisions of Ne^{2+} with Ar. The direction of the Ne^{2+} velocity is indicated by the arrow. The scattering centre is marked by a dot.

C Initial experiments

Initial experiments to test the performance of the apparatus have been performed on the atomic electron transfer reaction:

$$Ne^{2+} + Ar \rightarrow Ne^+ + Ar^+ \tag{2}$$

From the position sensitive data we can extract, as predicted, key quantities which characterise the dynamics of the reaction. For example:

- the angular distribution of each of the product ions
- the angle between the product ions as they separate
- the translational and internal energies of the product ions
- the scattering diagram
- the electronic states of the products and reactants from the energy balance.

For the Ne^{2+}/Ar reaction representative results are presented. Figure 2 shows the scattering diagram which demonstrates that the Ne^+ product is strongly "forward scattered". Figure 3 shows the individual angular distributions of the product ions, relative to the initial velocity of the reactant Ne^{2+} ions. For Ne^+ this distribution, as indicated in Figure 3, is strongly peaked in the forward direction (near 0^0), with a few ions back scattered. However, there is clear evidence of a bimodal (twin peaked) angular distribution even in the forward scattered ions. Such a bimodal angular distribution has been observed before for a electron transfer reaction of an atomic dication.[20] This bimodal

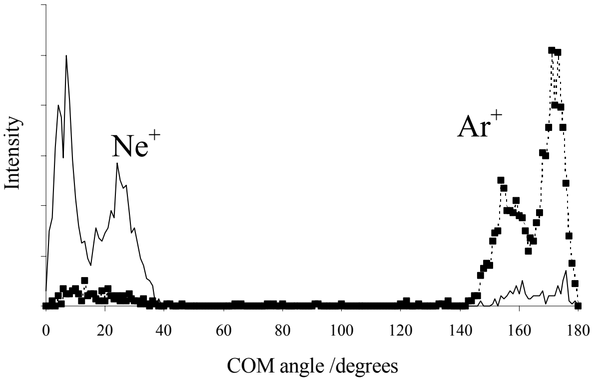

Figure 3 Centre of mass angular distributions of the products of reaction 3.

distribution is thought to result from the different angular scattering that occurs when the curve crossing between the reactant and product surfaces occurs on the approach or separation of the collision system.

In addition, from the energy balance of the reaction and the measured kinetic energies of the products, we can deduce which electronic states of the singly charged product ions are populated in the reaction.

D. Recent work

The above data shows that the potential power of the PSCO experiment to study ion energetics has been realised. The next step is to use this experiment to study the dynamics of chemical reactions of molecular dications and this poster will present the first studies of molecular dication chemical reactions using the PSCO technique. In addition, the results from PSCO studies of the electron transfer reactions of molecular dications with the rare gases will be presented. Such studies will allow a determination of the energy levels of previously uninvestigated dications from the energy balance of the electron transfer process.

E. Acknowledgements

SH thanks the EPSRC for the award of a studentship. This experiment was supported by the EPSRC under Grant GR/K11222. SDP thanks the Leverhulme Trust for a Research Fellowship. This study is a part of the European Network RTN1-1999-00254 "Generation, Stability and Reaction Dynamics of Multiply Charged Ions" (MCInet).

References

---

[1] D. Schröder and H. Schwarz, *J. Phys. Chem. A* **103,** 7385-7394 (1999).
[2] D. Mathur, *Phys. Rep.* **225,** 193-272 (1993).
[3] S. D. Price, *J. Chem. Soc. Faraday Trans.* **93,** 2451-2460 (1997).
[4] Z. Herman, J. Zabka, Z. Dolejsek, and M. Farnik, *Int. J. Mass Spectrom.* **192,** 191-203 (1999).
[5] Z. Herman, *Int. Rev. Phys. Chem.* **15,** 299-324 (1996).
[6] L. Mrazek, J. Zabka, Z. Dolejsek, J. Hrusak, and Z. Herman, *J. Phys. Chem. A* **104,** 7294-7303 (2000).
[7] K. A. Newson, N. Tafadar, and S. D. Price, *J. Chem. Soc. Faraday Trans.* **94,** 2735-2740 (1998).
[8] K. A. Newson and S. D. Price, *Chem. Phys. Lett.* **294,** 223-228 (1998).
[9] K. A. Newson and S. D. Price, *Chem. Phys. Lett.* **269,** 93-98 (1997).
[10] S. D. Price, M. Manning, and S. R. Leone, *J. Am. Chem. Soc.* **116,** 8673-8680 (1994).
[11] P. Tosi, W. Y. Lu, R. Correale, and D. Bassi, *Chem. Phys. Lett.* **310,** 180-182 (1999).
[12] P. Tosi, R. Correale, W. L. Lu, S. Falcinelli, and D. Bassi, *Phys. Rev. Lett.* **82,** 450-452 (1999).
[13] W. Y. Lu, P. Tosi, and D. Bassi, *J. Chem. Phys.* **112,** 4648-4651 (2000).
[14] Z. Dolejsek, M. Farnik, and Z. Herman, *Chem. Phys. Lett.* **235,** 99-104 (1995).
[15 N. Tafadar, N. Kaltsoyannis, and S. D. Price, *Int. J. Mass Spectrom.* **192,** 205-214 (1999).
[16] N. Tafadar, D. Kearney, and S. D. Price, *J. Chem. Phys.* **115,** 8819-8827 (2001).
[17] B. K. Chatterjee and R. Johnsen, *J. Chem. Phys.* **91,** 1378-1379 (1989).
[18] S. Hsieh and J. H. D. Eland, *J. Phys. B.* **29,** 5795-5809 (1996).
[19] S. Hsieh and J. H. D. Eland, *J. Phys. B.* **30,** 4515-4534 (1997).
[20] B. Friedrich and Z. Herman, *Chem. Phys. Lett.* **107,** 375-380 (1984).

A Statistical Analysis of Volatile Organic Compounds Observed During the TEXAQS2000 Air Quality Study at LaPorte, Tx, Using Proton-Transfer-Reaction Mass Spectrometry.

Thomas Karl[1], Bill Kuster[2], Tom Jobson[2,3], Eric Williams[2], Ray Fall[4], Fred Fehsenfeld[2] and Werner Lindinger[5]

[1] *ACD/ASP National Center for Atmospheric Research; tomkarl@ucar.edu*
[2] *Aeronomy Laboratory, National Oceanic and Atmospheric Administration*
[3] *Pacific Northwest Laboratories*
[4] *Cooperative Institute for Research in Environmental Sciences, University of Colorado*
[5] *Institute for Ionphysics, University of Innsbruck*

Abstract:

Statistical analysis of online VOC measurements obtained by Proton-Transfer-Reaction Mass Spectrometry (PTR-MS) during the TEXAQS2000 intensive period is presented. The experiment was based at the La Porte site, near the Houston ship channel (HSC), and deployed for continuous long-term monitoring. Multivariate techniques helped to identify various VOC sources in the vicinity of HSC and distinguish between different anthropogenic emissions. An assessment is given of the selectivity and interpretation of mass scans from this online technique in a complex urban and industrial VOC matrix.

1. Introduction

The greater Houston-Galveston metropolitan area is characterized by a high diversity of VOC, CO and NO_x sources, especially near the Houston ship channel (HSC). As a consequence, a great portion of potential O_3 precursors released within and around the HSC cause not only relatively high ozone formation rates but also highly variable ozone concentrations. The unique VOC mix in and around Houston represents a major difference from other metropolitan areas such as Nashville, Los Angeles and New York, which have been the focus of previous field studies to assess urban air quality. The observed VOC/NO_x ratios around Houston, for example, are significantly larger than expected from emission inventories and when compared to ratios obtained in other urban areas in the U.S. A significant portion of atmospheric emissions around the HSC area comes from petroleum refineries, synthetic organic chemical manufacturing plants and various mobile sources. Together with characteristic meteorological events such as the land-sea breeze flow reversal, the complex chemical mixture in southern Texas leads to a persistent ozone problem, which typically led to 20 days of NAAQS (National Ambient Air Quality Standard) exceedances within a 3 month period during the COAST study in 1993. Ground level ozone is considered as one target pollutant for control by the Clean Air Act in affected U.S. urban areas. As Houston, TX, is now generally recognized having the second highest ambient ozone problem among U.S. cities[1, 13], there is a current interest in developing strategies to bring this area into compliance with the NAAQS. State Implementation Plans required for noncompliant regions have to be based on a detailed knowledge of key-variables that govern ozone formation. VOCs in an high NO_x environment act as 'fuel' in the process of ozone production and thus are considered as target pollutants. VOC monitoring at the La Porte site during the TEXAQS2000 study addressed several issues:

- assess the main VOC reactivity in and around the HSC

- document large, unscheduled VOC releases near the HSC, that might contribute to unusually high ozone events
- see if the high observed VOC/NO_x ratios are due to inaccurate emission estimates of VOCs or NO_x
- evaluate the importance of chlorine chemistry on ozone formation
- investigate how VOC plumes influence the local radical budget and ozone formation
- compare measured VOC concentrations with existing emission inventories
- give an estimate of the magnitude of VOCs released by various point sources in the HSC

Here we present and evaluate the VOC dataset obtained by Proton-Transfer-Reaction Mass Spectrometry (PTR-MS)[3] at the La Porte site. We assess the selectivity of this on-line technique and give an interpretation of mass scans in a complex urban and industrial VOC matrix. Principal component analysis allowed us to identify various HSC sources and distinguish between different anthropogenic emissions.

2. Results

Table 1 Observed VOCs at La Porte (compound assignment in parenthesis is based on the TRI emission inventory); the rest were verified by GC intercomparison or isotopic analysis.

Mz+1 ion	**Compound**	Concentrations		
		Mean	Max	Median
M28*	HCN	0.3	6.0	0.2
M33	Methanol	10.8	574	6.2
M45	Acetaldehyde	3.4	79	2.3
M54	Acrylonitrile	0.4	56.8	0.1
M59	Acetone	4.0	69	3.3
M69	Isoprene	0.4	26.5	0.3
M79	Benzene	0.6	27.7	0.3
M93	Toluene	0.8	13.0	0.4
M105	Styrene	0.1	4.2	0.1
M107	Xylenes, Ethylbenzene	0.6	6.4	0.4
M121	C_{10}-Benzenes	0.4	5.3	0.2
M135	C_{11}-Benzenes	0.2	6.6	0.1
M149	C_{12}-Benzenes	0.02	0.5	0.02
M163	C_{13}-Benzenes	0.03	1.0	0.02<
M43	Propylene+Fragment M61	7.3	315	3.3
M61	$C_2H_4O_2$ (Acetic acid, Glycolaldehyde)	3.4	67.9	2.9
M83	C_6H_{10}	0.2	6.1	0.2
M85	C_6H_{12}	0.3	28.0	0.2
M87	$C_4H_6O_2$ (Vinyl acetate)	0.5	9.2	0.3
M89	$C_4H_8O_2$ (Dioxane)	0.1	12	0.0
M115	$C_7H_{14}O$ C_7-Ketone	0.4	155	0.2
M91/M73	$C_4H_{10}O_2$ (Ethoxyethanol)	0.1	1.2	0.1

* lower limit based on a reaction rate of 2e-9 cm^3s^{-1}

2.1 Meteorology

Surface winds at La Porte were characterized by north-westerly winds in the early morning (0:00 – 7:00) shifting during the day to the north and dominating from the east in the afternoon. Wind speeds at 10 m during the night generally varied between 2 and 5 m/s, with a slight decrease in the early morning. Along with the developing boundary layer, surface wind speeds increased around 9:00 and typically reached a maximum (6-8 m/s) during the afternoon and early evening (15:00 to 19:00). For wind speeds up to 4 m/s no distinct direction persisted and winds shifted corresponding to the daily land-sea breeze effect. Higher wind speeds, > 4 m/s, usually dominated from south to southeast (100-200°) and generally occurred in the afternoon. High ozone concentrations (August 30 and 31; ~200 ppbv) occurred during days with a surface high pressure region over the central Houston area drifting slowly to the southwest and causing low level winds from southwest to northwest at wind speeds around 1-3 m/s. Scattered thunderstorms occasionally caused heavy rain showers with wind speeds up to 20 m/s from various directions.

2.2 Dominant VOCs observed at LaPorte

Overall, 28 ions dominated the mass spectra obtained during August and September 2000. The 21 most important species are listed in Table 1. For many protonated species the selectivity of the PTR-MS instrument was good enough to identify a single compound attributing to the observed ion-density. In cases of mixed ions and higher molecular weight compounds typical fragmentation patterns, comparison with GC-MS and GC-FID measurements and the Toxic Release Inventory (TRI)[2] helped to identify individual compounds.

2.3 Statistical Analysis

Multivariate methods are widely used to estimate source-receptor relationships and are based on the mass conservation argument[5, 7, 8, 9]. Chemical mass balance models (CMB) describe a linear relationship between source activities (S), the relative source strength of source p (a) and measured properties such as the ambient concentration (C):

$$C_{ik} = \sum_{j=1}^{p} a_{ij} \cdot S_{jk} + \varepsilon_k , k = 1 ... m \tag{1}$$

where C_{ik} is the measured concentration of compound i at time k, a_{ij} the factor loading which is related to the source composition, S_{jk} the source activity and ε_k an error term to be minimized. Here we use two complementary approaches to extract source profiles and activities. Based on (1) the first method applies conventional principal component analysis (PCA)[6] of the standardized dataset. The obtained primary eigenvectors are the base of a new orthogonal coordinate system. When the transformed data set is plotted in this new coordinate system, every point can be assigned to the original observation. Corner points in the n subspaces represent occasions where a single emission source was predominantly active. By locating different vortices that bound the datacloud provisional source profiles can be obtained[11] . The second method involved factor analysis (FA) of the covariance matrix according to (2) using the VARIMAX rotation[13]:

$$\widetilde{C}_{ik} = \frac{C_{ik} - \overline{C}_i}{\sqrt{\overline{C_i^2} - \overline{C}_i^2}}, \widetilde{S}_{jk} = \frac{S_{jk} - \overline{S}_j}{\sqrt{\overline{S_j^2} - \overline{S}_j^2}}, \alpha_{ij} = a_{ij} \sqrt{\frac{\overline{S_j^2} - \overline{S}_j^2}{\overline{C_i^2} - \overline{C}_i^2}} , \tag{2}$$

where α_{ij} represent the 'factor loadings', which are related to the source compositions. Both approaches defined provisional source profiles that were further refined by an alternating least-square regression trimming towards positive factor loadings[11].

Figure 1 shows mixing ratios of a C_7-Ketone, aromatic source profile 1 and a substituted C_{12}-benzene plotted against wind-direction, and for all cases reveals a dominant polluted sector SSE for all cases which originated from a conglomerate of the synthetic organic industry in Harris located 5-8 km upwind. The typical signature of mobile sources with toluene/benzene ratios around two did not correlate with any distinct winddirection and reflected the nature of a more diffuse area source. The high correlation with CO also suggets that CO was mainly related to mobile sources at La Porte (benzene/CO= 9.8e-4). Diurnal plots were normalized according to the statistical model (3) (GLM),

$$\ln(c(i(t), j(t))) = a_1 + a_2 \cdot T(i(t), j(t)) + a_3 \cdot WD(i(t), j(t)) + a_4 \cdot ws(i(t), j(t)) , \tag{3}$$

where, i stands for half hour values of the day (i=1...48), j for the day of the week (j=1: Monday-Saturday, j=2: Sunday and holidays), t for time, T for Temperature, WD for wind direction and ws for windspeed.

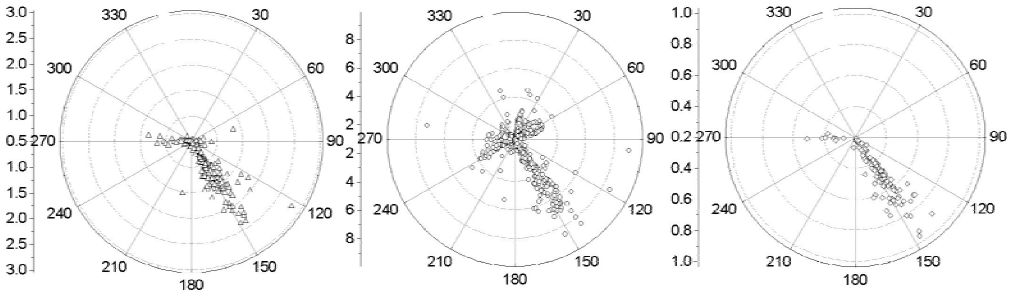

Figure 1 $C_7H_{14}O$ (Ketone M115$^+$) Benzene Source 1 (Harris) $C_{12}H_{18}$ (C_{12} benzene isomers)

The relative humidity was a perfect linear combination of ambient temperature and was not considered. Since VOCs exhibited a log-normal distribution, the logarithm of ambient concentrations were used in the GLM. All calculations were done with Systat10 (SPSS Inc.) and Matlab5.3 (Mathworks Inc.).

3. Conclusion

PTR-MS proved to be a valuable tool for realtime VOC monitoring of complex urban air chemistry. The main VOC reactivity in Houston originates from low molecular weight alkenes such as propene, which reached ambient concentrations up to 300 ppbv. Thus tropospheric ozone production is most likely driven by alkene-NO_x chemistry. The results suggest that the emission inventories currently used for regional air models in the greater Houston-Galvaston area need to be reevaluated and updated. Even well known pollutants such as C_9-C_{10}-benzenes seem to be underrepresented by at least one order of magnitude. Existing databases completely lack emission factors for some higher molecular weight compounds (for example C_7- ketones), which were present up to 3 ppbv. The PTR-MS technique could also trace some unusual compounds (e.g. acrylonitrile), that might not be important players for local ozone chemistry, but contribute to an increased regional VOC background. Some of these compounds, though, might have an impact on local air quality due to their toxicity.

Future PTR-MS deployments could involve mobile systems, that could be used to track down local polluters, or simply help to find leaks in the vast pipeline network and storage facilities. It could therefore become an attractive technique for the chemical and refining industry as well as environmental protection agencies.

4. References

[1] http://www.utexas.edu/research/ceer/texaqs/index.html
[2] http://www.epa.gov/triexplorer/facility.htm
[3] www.ptrms.com
[4] Andersson, C. A. and R. Bro. Chemometrics **2000**, 52, 1.
[5] Henry, C. H., Lewis, C. W., Hopke, P. K. and H.J. Williamson. Atmos. Environ. **1984**, 18, 1507.
[6] Jackson, J. E., A user's guide to principal components, Wiley & Sons, Inc., **1991.**
[7] Laurila, T., Hakola, H. and V. Lindfors. Phys. Chem. Earth (B) **1999**, 24, 689.

[8] Paatero, P. and P.K. Hopke, Chemometrics **2001**, in press.
[9] Paatero, P. and U. Tapper, Environmetrics **1994**, 5, 111.
[10] Singer, B. C. and R. A. Harley, Atmos. Environ. **1999**, 34, 1783.
[11] Stahelin, J., Locher, R., Moenkeberg, S. and W. A. Stahel, Int.J of Vehicle Design, in press.
[12] U.S. Environmental Protection Agency, Office of Air Quality. National Air Quality and Emissions Trends Report, 1995; U.S. Government Printing Office: Washington, DC, October **1996**; EPA 454/R-96005.
[13] Yu. T. and L. W. Chang. Atmos. Environ. **2000**, 34, 4499.

5. Acknowledgements

This work was funded by the U.S. EPA (Southern Oxidants Study), the Austrian Fonds zur Förderung der wissenshaftlichen Forschung (Project 14130), and NOAA grant NA06GP0483. T.K was also supported by the Atmospheric Chemistry Division and the Advanced Study Program at the National Center for Atmospheric Research, and thanks Alex Guenther and Al Cooper for their support.

Reactions of H_3O^+ with a number of bromine containing fully and partially halogenated hydrocarbons

Richard A. Kennedy[a], Chris A. Mayhew[b], Richard Thomas[b], and Peter Watts[c]

[a]School of Chemical Sciences, [b]School of Physics and Astronomy, University of Birmingham, Edgbaston, Birmingham B15 2TT, UK
[c] RSG Consulting, Salisbury, Wiltshire SP5 1SP, UK

The ion chemistry of bromine containing molecules is essentially unexplored. This lack of information, and the use of H_3O^+ as the reagent ion in the proton transfer reaction mass spectrometer (PTR-MS) developed by the late Professor W Lindinger and his colleagues at the Institut für Ionenphysik der Leopold-Franzens-Univeristat provide the motivation for this study. Here we present results on the reactions of the reagent ion H_3O^+ with the following halaogenated methanes; CH_3Br, CH_2Br_2, CH_2FBr, CHF_2Br, $CHFBr_2$, CH_2BrCl, $CHBrCl_2$, and $CHBr_2Cl$, together with a series of bromine containing ethanes; CH_3CH_2Br, CH_2BrCH_2Cl, CH_2BrCH_2Br, CF_3CF_2Br and CF_2BrCF_2Br. Fundamental studies of the reactions of H_3O^+ with molecules are essential for underpinning the use and development of this mass spectrometer. To our knowledge the majority of the data is being presented here for the first time, with a few exceptions. Only the reactions of H_3O^+ with CHF_2Br [1] and with CH_3Br and CH_3CH_2Br [2] have been reported before.

The experimental rate coefficients, k_{exp}, the product ions, and product ion branching ratios for the reactions of H_3O^+ with the bromine containing methane molecules CH_3Br, CH_2Br_2, CH_2FBr, CHF_2Br, $CHFBr_2$, CH_2BrCl, $CHBrCl_2$, $CHBr_2Cl$ are presented in table 1. Table 2 provides the rate and branching ratio data for the reactions of H_3O^+ with the bromine containing C_2 molecules CH_3CH_2Br, CH_2BrCH_2Cl, CH_2BrCH_2Br, CF_3CF_2Br. Included in these two tables are the collisional rate coefficients (k_c).

Charge transfer, which is a commonly encountered mechanism in the reactions of molecules with positive ions resulting in a transfer of an electron from the neutral to the reagent cation is ruled out because of the low recombination energy associated with H_3O^+. However, H_3O^+ is observed to react in a number of other ways, namely:

(i) *Association Reactions.* Three-body associative process with H_3O^+ is the reaction channel observed for M = CH_3Br, CH_2FBr, CHF_2Br, CF_3CF_2Br, and, in trace amounts, CF_2BrCF_2Br. It is also observed, but not as the only product ion, with CH_3CH_2Br.

(ii) *Proton transfer.* Proton transfer was not observed to be a major reaction channel in this study. None of the reactions with the C_1 molecules resulted in proton transfer. For the C_2 molecules the proton transfer product MH^+ was only observed for two of the reactant molecules and then not as the only product ion.

(iii) *Hydrogen halide elimination and associated reactions.* These are observed for the compounds $CHFBr_2$, $CHBrCl_2$, $CHBr_2Cl$, CH_2BrCH_2Br, CH_2BrCH_2Cl, and CH_3CH_2Br. In general a common pattern is observed; one or two pairs of ions are observed, a carbocation, formed by the loss of a halogen (as the hydrogen halide), and the corresponding protonated alcohol where the water from the H_3O^+ is retained. An exception is $CHBrCl_2$ where two protonated alcohols are formed but only one carbocation observed. It is suggested that in all cases the protonated alcohol is the initial product ion and that if this has sufficient internal energy it can fragment into water and the carbocation before being collisionally stabilised.

	CH_3Br	CH_2Br_2	CH_2FBr	$CHFBr_2$
k_{exp}[a]	0.04	NR	0.28	1.9
k_c[a, b]	2.7	2.4		
Product ion(s)[c]	$CH_3Br.H_3O^+$ (100)	-	$CH_2FBr.H_3O^+$ (100)	$CHBr_2^+$ (54) $CHBr_2O^+H_2$ (40) $CHFBr^+$ (5) $CHFBrO^+H_2$ (1)

	CHF_2Br	CH_2BrCl	$CHBrCl_2$	$CHBr_2Cl$
k_{exp}[a]	0.02	NR	1.7	1.7
k_c[a, b]	1.4			
Product ion(s)[c]	$CHF_2Br.H_3O^+$ (100)	-	$CHBrClO^+H_2$ (69) $CHBrCl^+$ (22) $CHCl_2O^+H_2$ (7) $CHClOH^+$ (1) $CHBrOH^+$ (1)	$CHBr_2^+$ (38) $CHBr_2O^+H_2$ (35) $CHBrCl^+$ (20) $CHBrClO^+H_2$ (6) $CHBrOH^+$ (1)

Table 1. Reaction rate coefficients, the product ions, and the branching percentages for the reactions of H_3O^+ with CH_3Br, CH_2Br_2, CH_2FBr, $CHFBr_2$, CHF_2Br, CH_2BrCl, $CHBrCl_2$ and $CHBr_2Cl$ at 300 K. NR refers to no observable reaction, which provides an upper limit of 10^{-13} cm^3 $molecule^{-1}$ s^{-1}.

[a] The reaction rate coefficients, both experimental (k_{exp}) and calculated (k_c) are given in units of 10^{-9} cm^3 $molecule^{-1}$ s^{-1}, and are considered to be accurate to ± 20%. [b] The calculated 300 K collisional reaction rate coefficients are given for reactant neutral molecules with known polarizabilities and dipole moments. For CHF_2Br only the polarizability is available, and hence the collisional rate refers to the Langevin value. [c] Ion branching percentages are given in parentheses.[16]

	CH_3CH_2Br	CH_2BrCH_2Cl	CH_2BrCH_2Br
k_{exp}[a]	1.2	1.8	1.9
k_c[a, b]	3.0	2.3	2.4
Product ion(s)[c]	$CH_3CH_2Br.H^+$ (46) $CH_3CH_2O^+H_2$ (32) $CH_3CH_2Br.H_3O^+$(22)	$CH_2BrCH_2O^+H_2$ (78) $CH_2BrCH_2^+$ (22)	$CH_2BrCH_2O^+H_2$ (92) $CH_2BrCH_2^+$ (7) $CH_2BrCH_2Br.H^+$ (1)

	CF_3CF_2Br	CF_2BrCF_2Br

k_{exp}[a]	< 0.0005	0.19
k_c[a, b]		
Product ion(s)[c]	$CF_3CF_2Br.H_3O^+$ (100)	$CF_2BrCF_2Br.H_3O^+$ (100)

Table 2. Reaction rate coefficients, the product ions, and the branching percentages for the reactions of H_3O^+ with CH_3CH_2Br, CH_2BrCH_2Cl, CH_2BrCH_2Br, CF_3CF_2Br and CF_2BrCF_2Br at 300 K.

[a] The reaction rate coefficients, both experimental (k_{exp}) and calculated (k_c) are given in units of 10^{-9} cm^3 $molecule^{-1}$ s^{-1}, and are considered to be accurate to ± 20%. [b] The calculated 300 K collisional reaction rate coefficients are given for reactant neutral molecules with known polarizabilities and dipole moments. [c] Ion branching percentages are given in parentheses.

This present study illustrates that the reactions of H_3O^+ with molecules can be more varied than just simple proton transfer. Such reactions have the potential of extending the use of the PTR-MS for trace gas detection and other applications. This study also serves to illustrate the need for fundamental studies of ion-molecule studies to provide rate data, product ion distributions, and mechanistic information. These feed into the applied areas of trace gas detection to which the PTR-MS is so well suited. This parallels the research activities Professor W Lindinger, drawing extensively from the fundamental and applied sciences.

Acknowledgements

We are grateful to the Technological Plasmas Initiative Program, EPSRC, (Grant Reference: GR/L82083) and a JREI grant GR/R06489/01 for the financial support of this study.

References

---

[1] R. A. Morris, A. A. Viggiano, S. T. Arnold, J. F. Paulson, and J. F. Liebman, *J. Phys. Chem.* **99** (1995) 5992.

[2] P. Španel and D. Smith, *Int. J. Mass Spectrom.* **189** (1999) 213.

Investigation of Aluminum Surface Cleaning Using a Novel Capillary Non-Thermal Ambient Pressure Plasma

G. Korfiatis[1], L. Moskwinski[2], N. Abramzon[2,3], K. Becker[2], C. Christodoulatos[1], E. Kunhardt[2], R. Crowe[3], and L. Wieserman[4]

[1] *Center for Environmental Engineering, Stevens Institute of Technology, Hoboken, NJ 07030, USA*
[2] *Department of Physics, Stevens Institute of Technology, Hoboken, NJ 07030, USA*
[3] *PlasmaSol Corporation, Hoboken, NJ 07030, USA*
[4] *ALCOA Technical Center, Alcoa Center, PA 15069, USA*

Abstract

It is the objective of this project to investigate the interaction of a novel capillary non-thermal ambient pressure plasma with contaminated Al surfaces and to develop a new technology based on this concept that is suitable for the destruction and removal of organic contaminants from Al surfaces for industrial applications. Our new approach, which is intended to replace the current solvent-based cleaning process, offers three important advantages over other existing plasma-based methods: (i) a more efficient energy utilization, (ii) ambient-pressure operation, and (iii) easy scalability from laboratory scale to in-line industrial scale.

1. Introduction

The cleaning of metal surfaces such as aluminum (or stainless steel) surfaces, both during manufacturing and prior to their use in specific applications has been a significant environmental challenge for industry. The main contaminants on Al surfaces are volatile and non-volatile hydrocarbons and residual hydraulic fluids from leaks. Chemically, the contaminants are primarily aliphatic hydrocarbons, branch-chain hydrocarbons, and ester-compounds. Vapor cleaning using chlorinated or chloro-fluoro compounds, though effective, has become undesirable as are processes using aqueous cleaning baths of acids or bases, since the compounds and/or some of the by-products represent serious environmental hazards. The industry has generally welcomed research and development on more advanced cleaning techniques that eliminate or minimize undesirable and/or environmentally harmful by-products.

Industry experiments in the past with plasma-based Al surface cleaning methods utilized for the most part low-pressure discharge plasmas. The effort was terminated because of concerns relating to the prohibitive costs of vacuum enclosures for any production-line plasma-based cleaning reactor. Recent progress in the generation and maintenance of atmospheric-pressure discharge plasmas in ambient air make it desirable to re-visit the possibility of using plasma-based Al surface (and more generally speaking, metal surface) cleaning methods on an industrial scale. Researchers at Stevens Institute of Technology have achieved a novel method to generate and maintain stable, large volume, uniform atmospheric-pressure discharge plasmas by employing a novel capillary electrode structure [1]. This capillary dielectric electrode structure provides dynamic feedback stabilization of the current density in the cathode region of the discharge reactor and thus prevents the non-uniform growth of the current density, which is the precursor to discharge instabilities that eventually result in a glow-to-arc transition and the termination of the discharge.

2. Project Goals

The current project, which is carried out as a collaborative effort between Stevens Institute of Technology, PlasmaSol Corporation, and ALCOA has five main objectives:

- Characterization of the discharge plasma used in the present application
- Development of a laboratory-scale experimental system
- Investigation of plasma jets firing against conductive and non-conductive surfaces
- Investigation of an atmospheric-pressure plasma discharge system for controlled cleaning of Al surfaces contaminated with selected hydrocarbons
- Consideration scale-up of experimental system for in-line industrial use.

Consistent with the objectives of the project the following tasks were executed up to now and the pertinent results will be reported at the Conference :

- Construction of a discharge plasma reactor that fires the atmospheric-pressure plasma jets on non-conductive surfaces
- Characterization of the plasma jets
- Assessment of destruction of oils and volatile organics on non-conducting surfaces
- Modification of plasma jet reactor for firing against conducting surfaces
- Preliminary assessment of destruction of oils on conducting surfaces

3. The Capillary Electrode Plasma at Atmospheric Pressure

The basis for the atmospheric-pressure operation of the capillary electrode plasma is a novel electrode design that uses dielectric capillaries that cover one or both electrodes of the discharge reactor. The capillaries, with diameters in the range from 0.01 to 1 mm and length-to-diameter ratios of the order of 10:1, serve as plasma sources which produce jets of high-intensity plasma at atmospheric pressure under the right operating conditions. The plasma jets emerge from the end of the capillary and form a "plasma electrode" for the main discharge plasma. The field inside the capillary does not collapse after the formation of the streamer discharge due to the fact that the high electron-ion recombination at the wall of the capillary requires a large ion production rate along the axis of the capillary in order to sustain the current. Under the right combination of capillary geometry, dielectric material, and exciting electric field, a steady state can be achieved. Run-away into the arc is prevented by the fact that the current through the capillaries is self-limiting, i.e. the gas density inside the capillary decreases with time due to gas heating which puts an upper limit to the conductivity as a result of gas starvation. Compared to other atmospheric-pressure discharge plasmas, the capillary plasma requires a lower sustaining voltage, lower energy input per cm^3 of plasma generated, and achieves a higher average energy of the plasma electrons (up to 6 eV) at a lower gas temperature (approximately 350 - 400 K) and higher electron densities (up to 10^{14} cm^{-3}). These parameters were obtained from optical emission spectroscopic studies and from other standard plasma diagnostic techniques applied to a prototype laboratory capillary electrode discharge plasma.

4. Interaction of Plasma Jets with Conductive Surfaces

A significant challenge of this project was the development of a working system that can fire an array of plasma jets against a conductive surface consistently in a non-destructive manner. This is a much more challenging task than constructing a working plasma reactor that fires an array of jets again an insulating surface where shorting and arcing are not a problem. A prototype of such a device was recently constructed that overcomes the difficulties associated with maintaining an array of stable plasma jets firing against conductive surfaces. This device, which is a modified version of PlasmaSol's patented "plasma shower" reactor, ensure repeatable and reliable operation when firing against conductive surfaces. Figure 1 shows a prototype of the actual capillary electrode plasma reactor firing against a conductive surface (here a stainless steel surface). As the plasma strikes the surface, it diffuses more or less uniformly across the treated surface. In an initial proof-of-principle experiment, we demonstrated that the plasma depicted in fig. 1 can completely remove a layer of pump oil from a stainless steel surface with an exposure time of less than 1 minute. Additional preliminary results indicate that this new device has the ability to operate at different plasma intensities and the ability to tailor the plasma jet intensity to a given application.

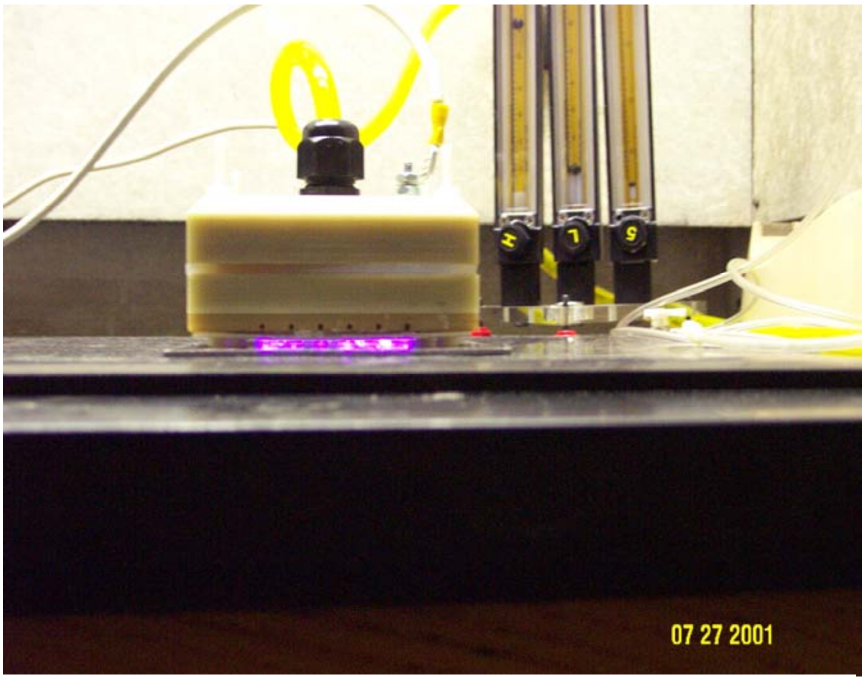

Fig. 1: Capillary electrode discharge plasma reactor firing against a conducting surface.

We characterized the hydrocarbon removal process from various surfaces by standard surface characterization studies supported by a detailed mass balance. These studies were carried out for both conductive and non-conductive. The macroscopic properties and the spatial distribution of the capillary plasma were examined for conductive and non-conductive surfaces in order to determine the effects of the treated material on the characteristics of the plasma (back-diffusion of volatile surface reaction products into the plasma !). Plasma generation was achieved using He, air, and various combinations of He and air as carrier gases. The experiments were performed by inserting uncontaminated surfaces into the plasma region and by subsequently monitoring the pertinent parameters (plasma distribution, plasma stability, current, voltage, etc). This assisted in determining distances between the treated surface and the electrodes that maximize surface exposure under a given set of operating conditions (power input, carrier gas, etc).

In order to characterize the effect of the plasma on a treated surface, we used an SEM analysis of the surface. Several samples of Al alloy 6061 were prepared for testing. A control sample was prepared and was always compared to the treated samples. The samples were subjected to the following conditions:

- Sample 1: control – no plasma; one hour elapsed - ambient air oxidation
- Sample 2: Plasma treated for two minutes at high power.

- Sample 3: Plasma treated for five minutes at low power.
- Sample 4: Plasma treated for five minutes at high power.
- Sample 5: Plasma treated for twenty minutes at high power.

The surfaces were analyzed using energy dispersive x-ray spectroscopy (EDXS) to determine the “before” and “after” effects of the plasma. We measured the electron ejection rate of a sample treated with a plasma for twenty minutes at high plasma density versus the control surface. This sample as well as other samples exposed for a shorter time and a lower power had no appreciable difference in the surface characteristics.

5. Summary

We have developed a prototype atmospheric-pressure plasma reactor based on the novel capillary dielectric electrode discharge concept [1] that is capable of firing an array of high-density plasma jets against a conductive surface such as Al in a reliable, reproducible, non-destructive manner. This reactor was subsequently used in a series of preliminary experiments aimed at the determination of the optimum operating conditions for the destruction and removal of hydrocarbon contaminants on Al surfaces. We have so far demonstrated that our method is capable of removing hydrocarbon contaminants efficiently without affecting the underlying Al surface. Further experiments are currently underway.

6. Acknowledgment

This work was supported by the US National Science Foundation under award DMI-9985359.

References

[1] E.E. Kunhardt and K. Becker, US Patent No. 5,872,426; US Patent No. 6,005,349; US Patent No. 6,147,452

ESI Mass Spectrometry applied to enantiodiscrimination of chiral systems.

A. Laganà[a], A. Paladini[a], A. Filippi[c], D. Catone[a], A. D'Ettole[c], M. Speranza[c], A. Giardini[a,b]

[a] *Dipartimento di Chimica, Università di Roma "La Sapienza", pl. A. Moro 5, I-00185 Roma, Italy*

[b] *CNR-Istituto Materiali Speciali, I-85050 Tito Scalo (Pz), Italy*

[c] *Facoltà di Farmacia, Dipartimento di Chimica e Tecnologia delle Sostanze Biologicamente Attive, Università di Roma "La Sapienza", pl. A. Moro 5, I-00185 Roma, Italy*

Chiral recognition in biological systems is based upon the aggregation of a target chiral molecule and a chiral selector [1]. Diastereomeric aggregates are held together by non covalent interactions and, therefore, are endowed with a different stability and reactivity. Various methodologies have been developed to evaluate these differences, including polarimetry, circular dichroism, nuclear magnetic resonance, chromatography and capillary electrophoresis [2]. Attention has been paid recently to the measure of the stability of diastereomeric aggregates under solvent free conditions through the use of resonant laser spectroscopy [3,4] and mass spectrometry [5]. The technique involving mass resolved resonant two photon ionization R2PI [3] coupled with supersonic molecular beam allowed to explore the intrinsic forces in isolated chiral clusters through the measure of ionization and fragmentation potentials and binding energies of some diastereomeric pairs such as chiral aromatic alcohols (reference) clustered with chiral aliphatic alcohols and amines (analyte) [6-8]. Unfortunately, it is difficult to apply this technique to the study of biomolecules in gaseous phase because most of them are non-volatile and thermally labile. Many efforts have been made to find new vaporization methods. Among them, electrospray ionization, coupled with mass spectrometric detection (ESI-MS), proved most suitable since it provides precious information on the stability of chiral clusters simply through the measure of ion abundances [5-8].

According to the foundations of Cooks' kinetic method [9,10], gas phase discrimination of chiral analytes ($\mathbf{A_R}$ and $\mathbf{A_S}$) is obtained by measuring of the relative stability of their diastereomeric complexes with a chiral reference selector (**ref**). Collisionally induced dissociation (CID) of the diastereomeric cluster ions $[\mathbf{M}\cdot(\mathbf{ref})_2\cdot\mathbf{A_R}]^+$ and $[\mathbf{M}\cdot(\mathbf{ref})_2\cdot\mathbf{A_S}]^+$, where $\mathbf{M}$ = H^+, Li^+, Na^+ and K^+, may produce different fragmentation patterns reflecting the relevant $[\mathbf{M}\cdot\mathbf{ref}\cdot\mathbf{A_R}]^+$ and $[\mathbf{M}\cdot\mathbf{ref}\cdot\mathbf{A_S}]^+$ vs.$[\mathbf{M}\cdot(\mathbf{ref})_2]^+$ stability (ΔG_R and ΔG_S, respectively). It is convenient to define the cluster ions as "homo" when the analyte and **ref** have the same configuration, and "hetero" in the opposite case. Measurement of the ratio of the "homo" vs. "hetero" ion abundance ratios provides the chiral selectivity R_{chiral}, i. e.:

$$R_{chiral} = \frac{R_{homo}}{R_{hetero}} = \frac{[\mathbf{M{\cdot}ref{\cdot}A_S}]^+/[\mathbf{M{\cdot}(ref)_2}]^+}{[\mathbf{M{\cdot}ref{\cdot}A_R}]^+/[\mathbf{M{\cdot}(ref)_2}]^+} \tag{1}$$

if the *S* enantiomer of **ref** is employed. The relative stability of the "homo" vs. the "hetero" $[\mathbf{M}\cdot\mathbf{ref}\cdot\mathbf{A}]^+$ cluster ion ($\Delta\Delta G$) is calculated from eq. 2, where T_{eff} is the effective temperature [11] and R is the gas constant.

$$\ln R_{chiral} = \frac{\Delta\Delta G}{RT_{eff}} \tag{2}$$

Here we report several examples of the application of the ESI-MS^2-CID technique to the enantiodiscrimination of chiral α-aminophosphonic acids. α-Aminophosphonic acids are the analogues of natural α-aminocarboxylic acids in biological systems. The biological activity of these chiral compounds is governed by the stability of their unsolvated inclusion complexes into the chiral cavity of an enzyme, normally containing also metal ion centers. For this reason, we deemed it important to investigate the affinity of α-aminophosphonic acids towards first-group metals in gaseous phase and how this can be affected by the ligands configuration. The results are discussed in the light of structure calculation performed by using an empirical force field.

Figure 1 reports typical CID fragmentation spectra of diastereomeric clusters containing one of the (1-amino-2-methylpropyl)phosphonic acid enantiomers ($\mathbf{P_R}$ and $\mathbf{P_S}$), as analytes, the (S)-(+)-(1-aminoethyl)phosphonic acid $\mathbf{E_S}$, as **ref**, and a sodium ion ($[\mathrm{Na}\mathbf{P_R}(\mathbf{E_S})_2]^+$ and $[\mathrm{Na}\ \mathbf{P_S}\ (\mathbf{E_S})_2]^+$). Their fragmentation leads essentially to the $[\mathrm{Na}\mathbf{P_{S,R}}\mathbf{E_S}]^+$ and $[\mathrm{Na}(\mathbf{E_S})_2]^+$. The dissociation patterns were found to be rather insensitive to the collision gas (N_2) pressure (5-15 mbar) and moderately sensitive to the collision energy (2-18 eV lab frame). Analogous results are found for the other α-aminophosphonic mixtures investigated [12,13].

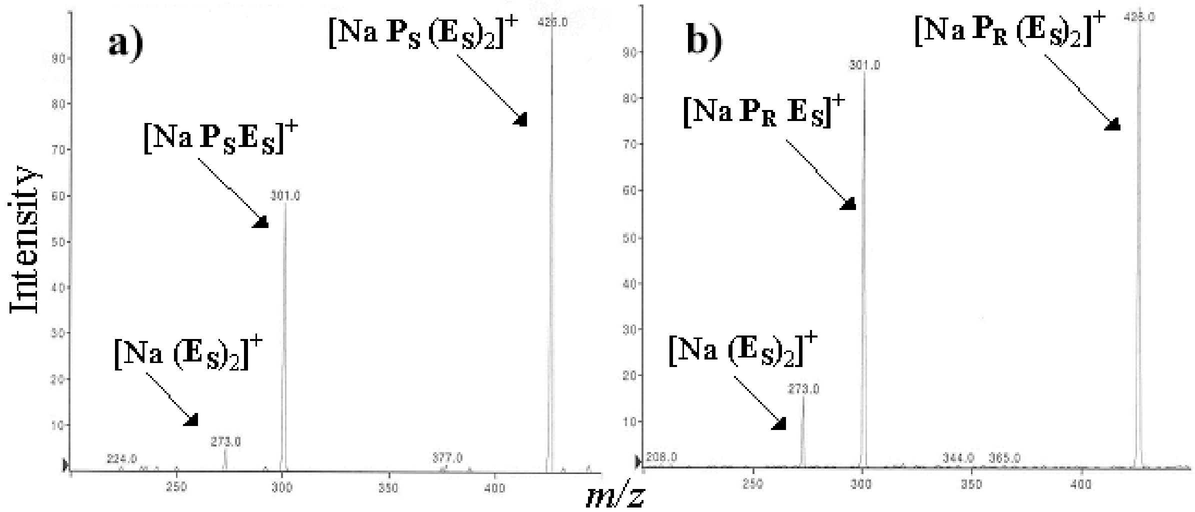

Fig.1 ESI-MS^2-CID spectrum of $[\mathrm{Na}\ \mathbf{P_S}\ (\mathbf{E_R})_2]^+$ (a) and $[\mathrm{Na}\ \mathbf{P_R}\ (\mathbf{E_R})_2]^+$ (b). The spectra are the result of 300 scans at 8 eV collision energy (lab frame).

The chiral resolution factors R_{chiral} for the diastereomeric clusters investigated are reported in Table 1. An $R_{chiral}<1$ value indicates that the heterochiral $[\mathbf{MA_{R,S}ref}]^+$ complex is more stable than the homochiral $[\mathbf{MA_{S,R}ref}]^+$ one. For $R_{chiral}=1$ there is no stability differences and chiral discrimination is unattainable by this method. Within the reasonable assumption that entropy effects on fragmentation are negligible, the ΔΔG term represents the difference in binding energy of the homochiral vs. the heterochiral cluster ($\Delta\Delta H = \Delta H_{HOMO}-\Delta H_{HETERO} = -RT\ln R_{chiral}$).

The reproducibility of the present method was investigated changing the chirality of the reference acid **ref**. The results obtained using the other **ref** enantiomer was within ca. 10% error and the uncertainty associated with consecutive measurements of the same system was within 5%.

M^+	**A**	**ref**	$\mathbf{R_{chiral}}$	**Average** $\mathbf{R_{chiral}}$	$\Delta\Delta H_{950}$ **(KJ mol^{-1})**
H^+	**E**	$\mathbf{P_S}$	0.87±0.05	0.83 ±0.08	1.5±0.7
	E	$\mathbf{P_R}$	0.80±0.08		
	P	$\mathbf{E_S}$	0.79±0.08		
	P	$\mathbf{E_R}$	0.85±0.04		
Li^+	**P**	$\mathbf{E_S}$	1.25±0.05	1.25±0.08	-1.8±0.7
	E	$\mathbf{P_S}$	1.25±0.05		
Na^+	**P**	$\mathbf{E_S}$	0.75±0.07	0.79±0 .07	1.9±0.7
	E	$\mathbf{P_S}$	0.87±0.05		
	E	$\mathbf{P_R}$	0.75±0.08		
	P	$\mathbf{E_R}$	0.80±0.04		
K^+	**P**	$\mathbf{E_S}$	0.90±0.05	0.90±0.07	0.7±0.5
	E	$\mathbf{P_S}$	0.90±0.05		

Table I . Enantiodifferentiation of chiral α-aminophosphonic acids (A_S and A_R) by ESI-MS^2-CID fragmentation of their diastereomeric clusters $[M\ A_S\ (ref)_2]^+$ and $[M\ A_R\ (ref)_2]^+$ (M= proton or first-group metal; ref = reference α-aminophosphonic acids of defined configuration).

From the table it appears that the stability difference is ranging from +1.9 to –1.8 KJ/mol and there is not evidence that the homochiral cluster is more stable than the heterochiral, as found in neutral [$\mathbf{A_{R,S}ref}$] aggregates obtained in supersonic beam expansion. Stability difference seems to be related to the nature of the metal center. From the calculated structure it appears that the most probable configuration is the one with reference molecules directly bounded to the metal center [13].

References

[1] W. H. Pirkle, T. C. Pochapsky. Three point model for chiral recognition. *Chem. Rev.*, 1989, **89**, 327-338.

[2] E. Eliel, S. H. Wilen, N. L. Menden. Stereochemistry of Organic Compounds, Wiley-Interscience, N.Y. 1994.

[3] S. Piccirillo, C. Bosman, D. Toja, A. Giardini Guidoni, M. Pierini, A. Troiani, M. Speranza. Gas Phase enantiodifferentiation of chiral molecules. Chiral recognition of 1-phenyl-1-propanol/2-butanol clusters by resonance enhanced multiphoton ionisation spectroscopy. *Angew. Chem. Int. Ed. Engl.*, 1997, **36**, 1729-1731.

[4] A. R. Al-Rabaa, E. Bréhéret, F. Lahmani, A. Zehnacker. Enantiodifferentiation in jet-cooled van der Waals complexes of chiral molecules. *Chem. Phys. Lett.*, 1995, **237**, 480-484.

[5] K. Vékey, G. Czira. Distinction of amino acid enantiomers based on the basicity of their dimers. *Anal. Chem.*, 1997, **69**, 1700-1705.

[6] A. Giardini Guidoni, S. Piccirillo, D. Scuderi, M. Satta, T. M. Di Palma and M. Speranza. Chirality and intermolecular forces: studies using R2PI experiments in supersonic beams. *Phys. Chem. Chem. Phys.*, 2000, **2**, 4139-4142.

[7] A. Latini, M. Satta, A. Giardini Guidoni, S. Piccirillo and M. Speranza. Short-range interactions within molecular complexes formed in supersonic beams: structural effects and chiral discrimination. *Chem. Eur. J.*, 2000, **6**, 1042-1049.

[8] A. Latini, D. Toja, A. Giardini Guidoni, A. Palleschi, S. Piccirillo and M. Speranza. Spectroscopic enantiodifferentiation of chiral molecules in the gas phase. *Chirality*, 1999, **11**, 376-380.

[9] W. A. Tao, D. Zhang, E. N. Nikolaev, R. G. Cooks, *J. Am. Chem. Soc.* 2000, **122**, 10598.

[10] W. Y. Shen, P. S. H. Wong, R. G. Cooks, *Rapid Commun. Mass Spectrom.* 1997, **11**, 71.

[11] J. Laskin, J. H. Futrell, *J. Phys. Chem.* 2000, **104**, 8829.

[12] G. Fago, A. Filippi, A. Giardini, A. Laganà, A. Paladini, M. Speranza. Chiral Recognition of O-Phospho-serine by Mass Spectrometry. *Angew. Chem. Int. Ed.* 2001, **40** (21), 4051-4054.

[13] A. Paladini, C. Calcagni, M. Satta, T. Di Palma, M. Speranza, A. Laganà, G. Fago, A. Filippi, A. Giardini Guidoni. Enantiodiscrimination of chiral α-aminophosphonic acids by mass spectrometry. *Chirality* 2001, **13**, 707-711.

Successive ligand substitutions in the $Fe(CO)_n^+/H_2O$ systems (n=1-5) observed in a triple cell FT-ICR mass spectrometer

Sophie Le Caër, Michel Heninger, Hélène Mestdagh

Laboratoire de Chimie Physique (UMR 8000, associated to CNRS),
Bât. 350, Université Paris-Sud, 91405 Orsay cedex, France

The reactivity of various iron carbonyl cations $Fe(CO)_n^+$ (n=1-5) with water has been investigated in an early work by Foster and Beauchamp [1] [2]. They measured the rate constants for the primary reactions of $Fe(CO)_n^+$ with water in a mixture of $Fe(CO)_5$ with H_2O. However, it is interesting to study separately the reactivity of the $Fe(CO)_n^+$ ions on H_2O to obtain accurate information on the different ligand substitutions. Moreover, the energy dependence of rate constants was investigated, as various $Fe(CO)_n^+/L$ systems studied in our laboratory (L=methanol [3], dimethylether [4]) were found to be strongly dependent on the energy of the reacting ions.

Experimental device and data analysis:

It consists in three ICR cells which are differentially pumped. The first is used as an *ion source*: the ions are generated by electron impact ionization upon $Fe(CO)_5$, and are mass selected. They are then transferred into the *second cell*, in which they can be relaxed either radiatively or collisionally with Ar atoms, before going into the third cell (the *reaction cell*) in which they react with water molecules during various times at a constant pressure. In the case of $Fe(CO)_2^+$, a mixture of water with argon at different pressures in the third cell was studied too. Then, they are drifted back to the *second cell* in order to be mass detected, as an efficient differential pumping ensures a pressure drop of a factor of 250 between the central cell and the two adjacent cells. The drift energy of the ions remains negligible compared to thermal energy, so that the primary reactions take place at thermal kinetic energy.

The intensity of each ion signal is normalized to the total ion signal and plotted as a function of the reaction time. The reaction scheme is checked using selective ejection. The set of experimental curves is globally analyzed using a "home-made" program: the so-called KINET program. It enables to get the different rate constants along with their uncertainties as well as to know whether the different rate constants are well determined or not.

Results:

In all the $Fe(CO)_n^+/H_2O$ systems (n=1-4), ligand substitutions are the only reactions observed. No reaction was observed in the $Fe(CO)_5^+/H_2O$ system under our experimental conditions: 100 ms reaction time and 2.5 10^{-6} Torr of H_2O.

The different reactions along with the rate constants and uncertainties are reported in Table 1. In the $Fe(CO)_n^+$ systems, the only reactions observed for n=1-2 are the successive substitutions of one CO by one water molecule whereas for n=3-4, a second channel in which two CO ligands are directly replaced by one H_2O molecule is observed. In the latter case, the $Fe(H_2O)_n^+$ (n=3-4) ion is never detected.

It is interesting to note that in the case of reaction ***(R)***, the rate constant measured for the CO substitution on $Fe(CO)(H_2O)^+$ is more than twice larger in the $Fe(CO)_3^+$ system than in the $Fe(CO)_2^+$ system. This significant difference can be attributed to the difference in the average energy contents of the reacting $Fe(CO)(H_2O)^+$ ion, which is likely lower for ions arising from double substitution on $Fe(CO)_3^+$ than from single substitution from $Fe(CO)_2^+$. In order to check and study the negative energy dependence of this reaction, the $Fe(CO)_2^+/H_2O$

system was investigated in the presence of different pressures of argon, allowing to partly thermalize the intermediate $Fe(CO)(H_2O)^+$ ions.

Ion	Reaction	Rate constant (10^{-10} $cm^3.s^{-1}$)
$Fe(CO)^+$	$Fe(CO)^+ + H_2O \rightarrow Fe(H_2O)^+ + CO$	12.0 ± 0.1
$Fe(CO)_2^+$	$Fe(CO)_2^+ + H_2O \rightarrow Fe(CO)(H_2O)^+ + CO$	17.3 ± 1.0
	$Fe(CO)(H_2O)^+ + H_2O \rightarrow Fe(H_2O)_2^+ + CO$ ***(R)***	8.15 ± 0.6
$Fe(CO)_3^+$	**$Fe(CO)_3^+ + H_2O \rightarrow Fe(CO)_2(H_2O)^+ + CO$**	15.5 ± 0.7
	$Fe(CO)_3^+ + H_2O \rightarrow Fe(CO)(H_2O)^+ + 2CO$	3.0 ± 0.1
	$Fe(CO)_2(H_2O)^+ + H_2O \rightarrow Fe(CO)(H_2O)_2^+ + CO$	19.2 ± 0.9
	$Fe(CO)(H_2O)^+ + H_2O \rightarrow Fe(H_2O)_2^+ + CO$ ***(R)***	20.5 ± 1.2
$Fe(CO)_4^+$	**$Fe(CO)_4^+ + H_2O \rightarrow Fe(CO)_3(H_2O)^+ + CO$**	11.5 ± 0.5
	$Fe(CO)_4^+ + H_2O \rightarrow Fe(CO)_2(H_2O)^+ + 2\ CO$	3.3 ± 0.2
	$Fe(CO)_2(H_2O)^+ + H_2O \rightarrow Fe(CO)(H_2O)_2^+ + CO$	18.3 ± 1.3
	$Fe(CO)_3(H_2O)^+ + H_2O \rightarrow Fe(CO)_2(H_2O)_2^+ + CO$	10.1 ± 0.5
	$Fe(CO)_3(H_2O)^+ + H_2O \rightarrow Fe(CO)(H_2O)_2^+ + 2\ CO$	2.0 ± 0.2
	$Fe(CO)_2(H_2O)_2^+ + H_2O \rightarrow Fe(CO)(H_2O)_3^+ + CO$	83 ± 4

Table 1: Successive reactions of $Fe(CO)_n^+$ (n=1-4) with H_2O. For the first substitution in the $Fe(CO)_n^+$ system (n=3-4), the main channel is indicated in bold.

In Figure 1, the experimental dependence of the rate constant k as a function of the number of collisions with Ar atoms (N_c) in the third cell is presented. N_c is the average number of collisions (either with Ar or with H_2O) encountered by a $Fe(CO)(H_2O)^+$ ion before the substitution reaction. It is evaluated as $N_c = (k_c(Ar)P_{Ar} + k_c(H_2O)P_{H2O})/(k\ P_{H2O})$, where P_{Ar} is the argon pressure, P_{H2O} is the water pressure and $k_c(Ar)$ and $k_c(H_2O)$ are the capture rate constants for the $Fe(CO)(H_2O)^+/Ar$ and $Fe(CO)(H_2O)^+/H_2O$ systems respectively, estimated according to [5]. The experimental curve can be well fitted using the following expression:

$$k(N_c) = k_1 - k_2 \exp(-\alpha N_c)$$

k_1 is the thermal rate constant, independent of the argon pressure, corresponding to a very high number of collisions. This value has to be consistent with the experimental results concerning the $Fe(CO)_3^+/H_2O$ system. k_2 corresponds to the substitution rate constant of unthermalized $Fe(CO)(H_2O)^+$ ions directly arising from $Fe(CO)_2^+$. The parameter α is the average relative energy loss of the ion for one collision. The k_1 value is set to $20.5\ 10^{-10}\ cm^3.s^{-1}$, which is the substitution rate constant in the $Fe(CO)_3^+$ system. k_2 and α are the fitted parameters and are found equal to:

$k_2 = (13.0 \pm 0.2)\ 10^{-10}\ cm^3.s^{-1}$ and $\alpha = 0.020 \pm 0.005$

According to available thermochemical data [6] [7], the Fe^+-CO and Fe^+-OH_2 binding energies are very close to each other. Therefore there is a need of accurate experimental determination of the thermochemistry of substitution. Work is in progress in order to study the $Fe(H_2O)_n^+/CO$ systems for n=1 and n=2, and to determine the relevant equilibrium constants using a mixture of CO and H_2O in the reaction cell.

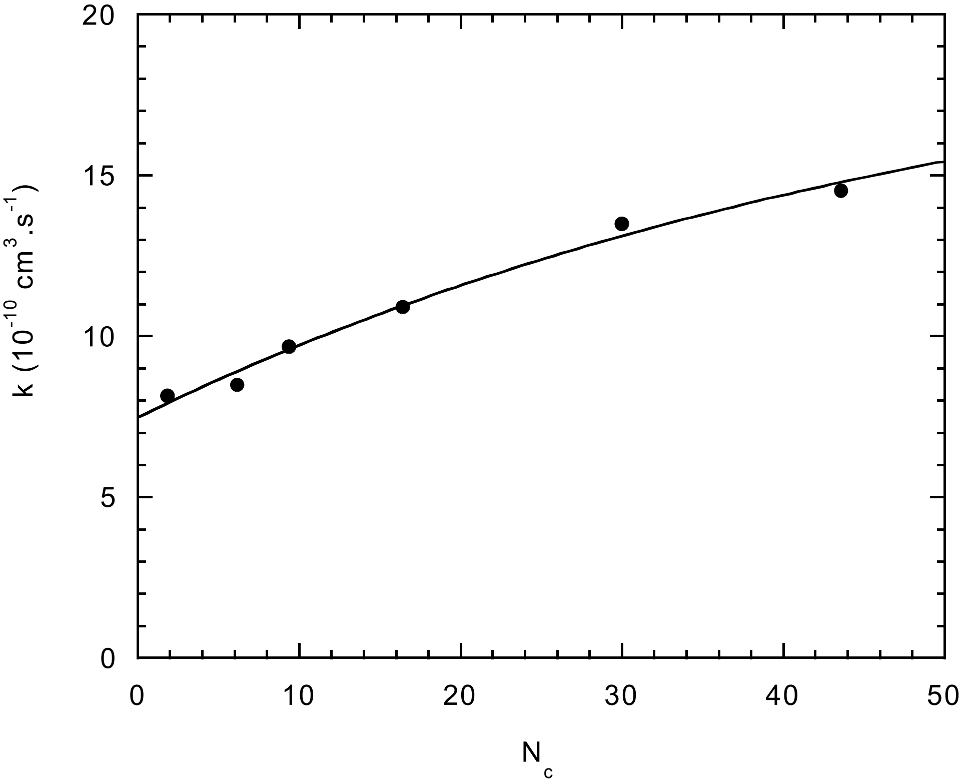

Figure 1: Dependence of k, the rate constant (in 10^{-10} $cm^3.s^{-1}$) of reaction ***(R)*** with the average number of collisions N_c. The solid line is a fit corresponding to the expression $k(N_c) = 20.5 - 13.0 \exp(-0.02N_c)$

References

---

[1] M.S. Foster, J.L. Beauchamp, *J. Am. Chem. Soc.* **93** (1971) 4924.

[2] M.S. Foster, J.L. Beauchamp, *J. Am. Chem. Soc.* **97** (1975) 4808.

[3] M. Heninger, P. Pernot, H. Mestdagh, P. Boissel, J. Lemaire, R. Marx, G. Mauclaire, *Int. J. Mass Spectrom.* **199** (2000) 267.

[4] S. Le Caër, M. Heninger, P. Pernot, H. Mestdagh, *Phys. Chem. Chem. Phys.* (2002), in press.

[5] T. Su, W.J. Chesnavich, *J. Chem. Phys.* **76** (1982) 5183.

[6] R.H. Schultz, P.B. Armentrout, *J. Phys. Chem.* **97** (1993) 596.

[7] R.H. Schultz, K.C. Crellin, P.B. Armentrout, *J. Am. Chem. Soc.* **113** (1991) 8590.

Reaction of gold cations with glycine studied in an FTICR cell

Joël Lemaire, Pierre Boissel, Gilles Ohanessian*

Laboratoire de Chimie Physique, Bâtiment 350, Université Paris-Sud, 91405 Orsay, France
(*) Laboratoire des Mécanismes Réactionnels, Ecole Polytechnique, 91128, Palaiseau, France

Because of their low volatility the study of reactions amino acids with bare metal ions is an experimental challenge. In this work we have studied in the gas phase using a FTICR mass spectrometer the reaction of gold cations with the simplest of the amino acid, glycine. Experimental results are compared with theoretical calculations for the energetics and the mechanism associated with the observed reactions. Gold cations are produced in the FTICR cell by laser ablation, focussing the tripled output of a NdYag laser on a target covered with a gold foil. The target is located outside the cell, in front of a 1mm diameter hole in the trapping plate. The gold cations, guided by the magnetic field penetrate in the cell where they are stabilised in the electrostatic trapping well. An effusive jet of glycine molecules is produced by heating a powder of solid glycine in an oven. This effusive jet pass through the ICR cell where the neutral molecule may collide with the stored gold cations. This is made possible by the open structure of the ICR cell (1) which is designed to give easy access to the center of the cell either for a molecular beam of neutral molecules or for the irradiation of the stored ions with photons.

The association complex $Au(Gly)^+$ is not observed on the mass spectra, due to the occurrence of reactive exothermic pathways. The main reaction pathways observed following the activation of glycine by gold cations (together with the calculated exothermicities) are :

		ΔH (kcal/mol)
$Au^+ + Gly$ ➔	$CH_2NH_2^+ + AuCOOH$	(-38.0)
	$Au(CH_2NH)(H2O)^+ + CO$	(-78.2)
	$Au(CH_2NH)(CO)^+ + H_2O$	(-91.5)
	$Au(CH_2NH)^+ + CO + H_2O$	(-33.2)

Reference

---

[1] J. Lemaire, M. Heninger, R. Marx, G. Mauclaire Int. J. Mass Spectrom. 189 (1999) 93-102

Flux Measurement of Methanol, Acetaldehyde and other Oxygenated VOCs from Crop Harvesting using Proton-Transfer-Reaction Mass Spectrometry and Surface Layer Gradient Method.

C. Lindinger[1], T. Karl[2], A. Guenther[2], A. Jordan[1], J. Tschiersch[3], F. Ruckerbauer[3], and H. Paretzke[3]

(1) Institute of Ionphysics, University Innsbruck, A-6020 Austria,
(2) ACD-NCAR, Boulder, CO, 80303,
(3) GSF-Forschungszentrum für Umwelt und Gesundheit, GmbH Ingolstädter Landstraße 1, D-85764 Neuherberg, Germany

Abstract:

PTR-MS technique was used to measure fluxes of various VOC's including oxygenates using surface layer gradient method. The VOC concentrations and temperatures were measured at heights of about 0.5m and 3.9m above ground at a field site in St. Johann in Tirol during and after grass cutting (24th and 25th of May 2000) in order to calculate fluxes. The sensible heat flux was obtained by a sonic anemometer with turbulence data analyzer. The major crop in this part of Austria are perennial grasses used for livestock farming. We observed VOC emission fluxes including methanol and acetaldehyde as the major volatile, C_5 and C_6 leaf wound compounds with lesser amounts and traces of acetone and butanone. This composition of VOC's is very similar to that released from slashed pasture grass [1]. At the same time, VOC fluxes were measured with PTR-MS and eddy covariance method [2]. Comparing the flux data of methanol and acetaldehyde of both days have shown very similar results.

Introduction:

A very important area of atmospheric research is the quantification of the impact of man made volatile organic compounds versus natural VOC emissions. In the last years, a huge effort was made to reduce man made VOC emissions all most at the same pace as they were rising by industrial pollution. To learn more about the influence of these VOC emissions to the chemistry of the atmosphere it is necessary to know more about the quantitative amount of natural VOC emissions. The vegetation on earth follows a living cycle were during all the time, dependent on the process (growing up, drying, cutting, decomposing), different amounts of VOC's are emitted. Living vegetation releases a large number of volatile organic compounds [3], and many of these VOCs can significantly alter the chemistry of the atmosphere [4,5]. For example, wounded plants release a mixture of C_6 hexyl and hexenyl compounds that are derived from major leaf fatty acids. These VOCs are primarily responsible for odour of grass cutting [6]. In addition to these C_6 compounds, a significant amount of other VOCs are released by grass and clover cutting [1]. The measurement of different VOC emission to the atmosphere was a major issue the last 10 years. For this many different methods were developed to get flux data of natural VOCs such as the surface layer gradient, the mixed layer gradient (e.g. with tethered balloons), the relaxed eddy accumulation (REA), the real time eddy covariance [2,7] and most recently the disjunct eddy covariance method (DEC) [8].

Field site description:

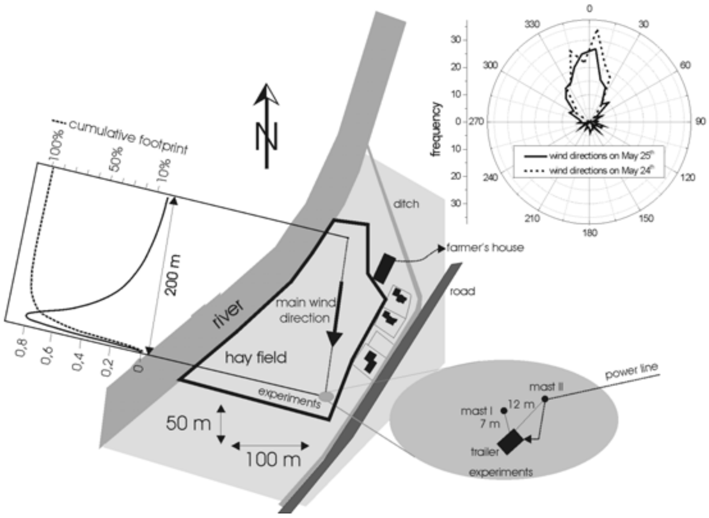

The field experiment was done on a 4 ha hay field in St. Johann in Tirol Austria in the time from May 23th to 26th 2000. Orchard grass, kentucky bluegras, timothy, red clover and rough bluegras, is the typical composition of alpine annual grasses used for hay production in this region. The map on the right side shows the site and the calculated cumulative footprint for a measurement height of 1m above ground level. The footprint for a measurement height of 3.9m (upper inlet height for gradient measurement) indicated that more than 90% of the cumulative footprint occurred within 200m. The experiments were situated at the south end of the field including a PTR-MS, sonic anemometer and meteorology-masts for surface layer gradient method, a second PTR-MS (fast responding) for real time eddy correlation (EC) and a second sonic-anemometer with relaxed eddy accumulation (REA) system. The REA as well as the EC system sampled at a height of 1m. The meteorology-masts provided wind, temperature and humidity gradients at heights of 3.9 and 10m. Turbulence data were obtained from a USA-1 T sonic anemometer with a built in turbulence kit.

Measurements and results:

Figure 2a and b show a summary of measured data on May 24th and May 25th. The hay field was cut on May 24th between 8:00 and 10:00. The local meteorological patterns resulted in northerly winds (optimal fetch) during most of the hours (see figure 1). Thus only fluxes obtained with the optimal footprint are presented. In the upper part of figure 2a and b, the fluxes of methanol, acetaldehyde, C_5-compounds, hexenal and other C_6-Compounds are shown as well as the most important events during the day. Following the figure, eddy coefficient, temperatures in different heights, humidity and sensible heatflux are shown together with the obtained methanol concentrations (not background corrected) as an example for the emissions during the day. While turning the hay significantly increasing VOC-concentrations and fluxes were observed. Methanol and acetaldehyde were highest around 15:30 with maximal fluxes of 9.9×10^{-6} gm^{-2} s^{-1} and 2×10^{-6} gm^{-2} s^{-1} respectively on May 24th. During the second day fluxes were generally lower with maximum at 4.6×10^{-6} gm^{-2} s^{-1} for methanol and 1.8×10^{-6} gm^{-2} s^{-1} for acetaldehyde. The farmer started collecting the hay at 15:45 on May 25th. By 16:30 no hay remained on the field and therefore VOC fluxes rapidly decreased. Fluxes of leaf-wounding compounds [1,3] such as hexanal, hexenals, hexenols, 3-methylbutanal, pentenols and butanone, were observed on both days too. Fluxes of 3(Z)-hexenal (fragment M81 and M99) peaked at 1.9×10^{-6} gm^{-2} s^{-1} on May 24th while the fluxes of C_5-compounds (mainly pentenols plus 3-methylbutanal) was observed to be in the range of $1\text{-}3.5 \times 10^{-6}$ gm^{-2} s^{-1}. M83 is a very important fragment of C_6-compounds like hexenols and hexenyl acetate while M85 is a fragment of hexanol and hexenyl acetate. The highest fluxes obtained for these compounds are in the range of 1 to 2.1×10^{-6} gm^{-2} s^{-1}. Integrated emissions for methanol and acetaldehyde are 65mg m^{-2} and 13mg m^{-2}. on May 24th and lower by a factor of 3 on May 25th. The average biomass density was measured to be 500gdw m^{-2} and thus yielding 130 µg methanol gdw^{-1} and 26 µg acetaldehyde gdw^{-1}. These numbers are in reasonable agreement with other measurements.

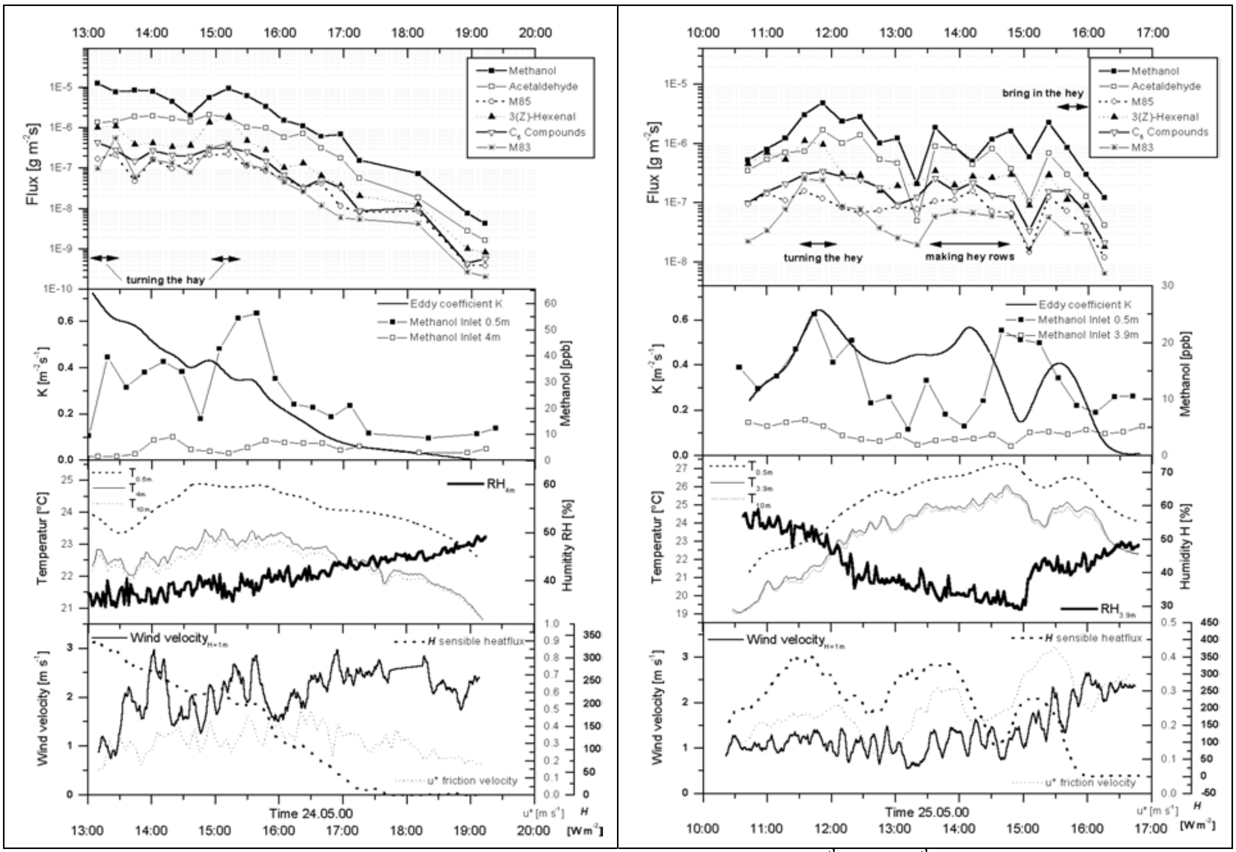

Figure 2a,b: Fluxes of various VOC like methanol, acetaldehyde on May 24th and 25th. Micrometeorological data like sensible heatflux, humidity and temperature were measured at the same time.

Comparing EC-data versus surface layer gradient data:

The flux data of methanol and acetaldehyde obtained by EC-method [2] and surface layer gradient method are shown for both days in figure 3a and b. Taking into account limiting factors due to meteorological conditions when measuring with the surface layer gradient method the correlation is very strong. This indicates the surface layer gradient method in combination with PTR-MS to be a very easy and useful technique to obtain fluxes of a large variety of VOCs at the same time.

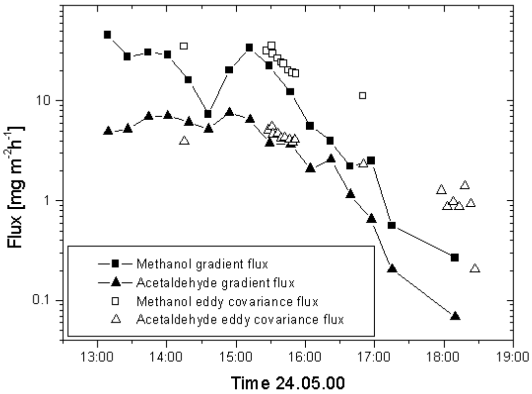

Figure 3a: Comparing flux data of methanol and acetaldehyde obtained by surface layer gradient method with EC-flux data on May 24th

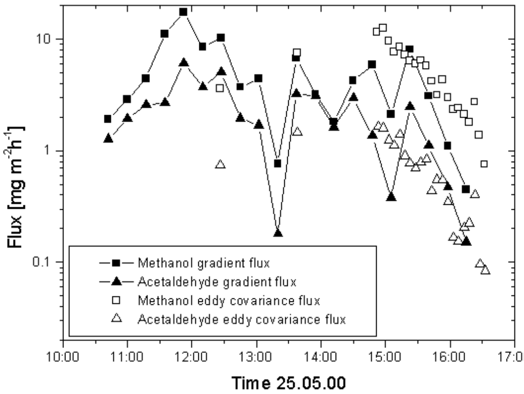

Figure 3b: Comparing flux data of methanol and acetaldehyde obtained by surface layer gradient method with EC-flux data on May 25th

Discussion:

These measurements demonstrate that the PTR-MS technique is a very useful tool to measure VOC-fluxes of biomass. Together with a detection limit of <2 x 10^{-6} gm^{-2} s^{-1} this instrument meets important requirement for measurements in field applications. The measurements were done in St. Johann (Tirol) which is situated in a 53 km^2 valley were about 50% of the area is used for hay production. The continued VOC releases during the drying of cut hay in periods of harvesting, is likely explained by the slow collapse of cellular structures which results in formation of leaf-aldehydes and leaf-alcohols [3]. The harvesting is done in 3 periods (April-May, June-July, August-September) each in only a few days due to sudden weather changes in this area. If 30% of the farming area around St. Johann is subjected to mowing activities and subsequently covered by drying vegetation this would give an input of about 6.7 x 10^{-6} gm^{-2} s^{-1} methanol, 1.3 x 10^{-6} gm^{-2} s^{-1} acetaldehyde and a total of 1.3 x 10^{-6} gm^{-2} s^{-1} for all other reactive compounds investigated in this work. High NO_x levels resulting from the traffic on B312 highway in this region in combination with peroxyradicals can play an important role in forming peroxyacetyl nitrate (PAN)-type compounds. Whereas acetaldehyde mainly reacts to form PAN, hexenals give rise to PPN (peroxypropionyl nitrate). Interestingly enough, high values of PPN were observed at field sites near areas subjected to intensive agriculture [9,10]. Antropogenic NO_x together with emissions of reactive VOCs described here, could influence the local air quality in many regions in the Alps on a short term basis and might have an impact on increasing ozone-levels that have been measured in the Alps [11].

References

[1] Kristine W., I. Galbally, Y. Ye, and M. Hooper, The emissions of volatile organic compounds (primarily oxygenated) from pasture, *J. Geophys. Res.,* 103, 10605-10619, 1998

[2] Karl, T., Guenther A., Lindinger C., Jordan A., Fall R., Lindinger W., Eddy covariance fluxes of Methanol, Acetaldehyde and other oxigenated VOCs using Proton-Transfer-Reaction-Mass-Spectrometry

[3] Fall, R., T. Karl, A. Hansel, A. Jordan, W. Lindinger, Volatile organic compounds emitted after leaf wounding: On-line analysis by proton-transfer-reaction mass spectrometry*, Journal of Geophysical Research*, Vol. 104, NO. D13, 15963 – 15974, 1999

[4] Fehsenfeld, F., et al., Emissions of volatile organic cornpounds from vegetation and the implications for atmospheric chemistry, *Global Biogeochem. Cycles*, 6, 389-430, 1992.

[5] Guenther, A., et al., A global model of natural volatile organic compound emissions, *J. Geophys. Res*., 100, 8873- 8892, 1995.

[6] Hatanaka, A., The biogeneration of green odour by green leaves – Review article number 85, *Phytochemistry*, Vol. 34, No. 5. 1201 – 1218. 1993

[7] Kaimal J. C., Wyngaard J. C., Izumi Y., Cote OR (1972) Spectral characeristicsof surface-layer turbulence. Q J Rmeteorol Soc 98: 563-589

[8] Rinne H. J. I., Delany A. C., Greenberg J. P., and Guenther A. B., A true eddy accumulation system for trace gas fluxes using disjunct eddy sampling method, *J. Geophys. Res., 105,* 24,791-24,798, 2000.

[9] Williams, J., et al., Regional ozone from biogenic hydrocarbons deduced frorn airborne measurements of PAN, PPN, and MPAN, Geophys. *Res. Lett*., 24, 1099 -1102, 1997.

[10] Roberts, J. M., S. B. Bertman, D. D. Parrish, and F. C. Fehsenfeld, Measurement of alkyl nitrates at Chebogue Point, Nova Scotia during the 1993 North Atlantic Regional Experiment (NARE) intensive, *J. Geophys. Res*., 103, 13,569-13,580, 1998.

[11] Prévôt, A.S.H., J.Dommen, M. Bäumle, M. Furger, Diurnal variations of volatile organic compounds and local ciculation systems in an Alpine valley, *Atmos. Environ., 34,* 1413-1423, 2000

Surface-Induced Dissociation of CO_2^{2+} Interacting with a Graphite Surface

A. Qayyum, C. Mair, T. Tepnual, W. Schustereder, P. Scheier, T.D. Märk

Institut für Ionenphysik, Leopold-Franzens Universität, A-6020 Innsbruck, Austria

Surface-induced dissociation of carbon dioxide molecular dication, CO_2^{2+} , is investigated by colliding this doubly charged ion with a graphite surface in the energy range of 0 to 30 eV. For this ion, mass and energy analyzed beam of CO_2^{2+} were focused on to the graphite surface and reaction products were monitored using a time-of-flight spectrometer. The only reaction product ions observed were O^+ and CO^+. Partial neutralization (charge exchange) for CO_2^{2+} to yield CO_2^+, was not observed.

So for surface-induced dissociation studies were mostly performed with singly charged molecular ions. There exit only a very few such studies on doubly charged molecular ions [1]. The present study has been undertaken to: (1) study the energetics of charge exchange between multiply charged molecular ions and surfaces and (2) to compare the nature and intensities of fragment ions for singly and multiply charged molecular projectiles. Previous experimental investigations on CO_2^{2+} include electron impact ionization mass spectrometry [2,3], double-charge-transfer spectroscopy [4] and collision-induced dissociation reactions with rare gases [5]. As for as our knowledge is concerned, no surface-induced dissociation experiment has been done with doubly-charged ions of this molecule.

The experimental apparatus used for present experiment is described in detail in Ref. [6]. Briefly, carbon dioxide molecular dications are produced in a Colutron ion source. The ions are extracted from source and accelerated to 3 keV for mass analysis and selection by a double focusing two sector field mass spectrometer. After passing the mass resolving slit of spectrometer, ions are refocused by an Einzel lens to the deceleration optics placed in front of the surface. The potential difference between the ion source and surface and hence the collision energy can be varied from almost zero to about 2 keV. Some of the secondary ions formed at the surface leave the shielded chamber through a 1 mm diameter orifice and are then subjected to the extraction and acceleration field of second mass spectrometer which is a linear time-of-flight mass selection with a flight tube of about 80 cm length. These secondary ions were then detected with micro channel plate.

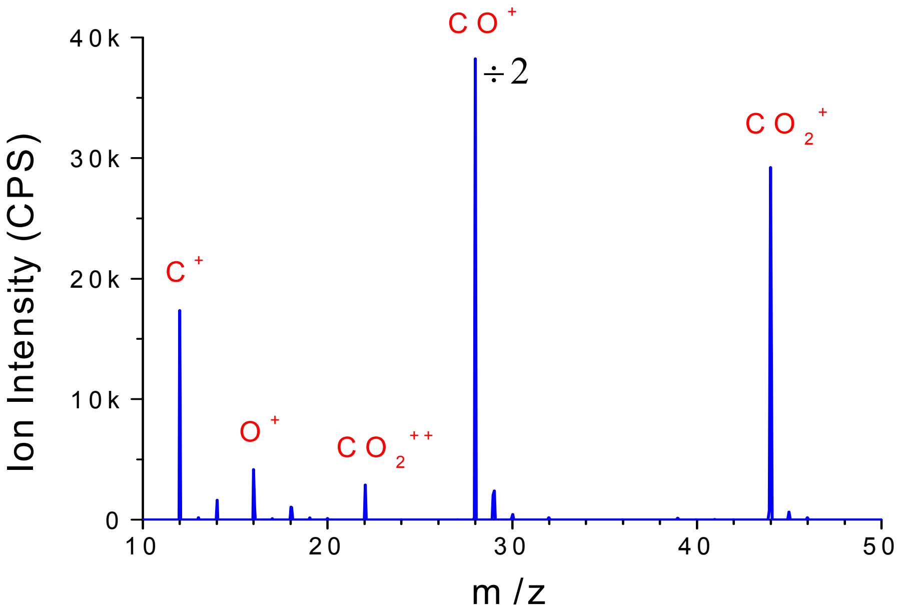

Fig. 1. Primary ion mass spectrum after ionization of CO_2 in Colutron ion source.

The primary ion mass spectrum obtained after optimization of the Colutron discharge for CO_2^{2+}, shown in Fig. 1, is dominated by the fragment ion CO^+, other fragment ions, in order of their decreasing intensities are C^+ and O^+ respectively. Doubly charged ion CO_2^{2+} (m/z = 22) is amount to be about 12% of the CO_2^+ intensity. Figure 2 shows the secondary ion mass spectrum for the interaction of doubly charged ion Co_2^{2+} with carbon tile from Tore Supra at a collision energy of 10 eV.

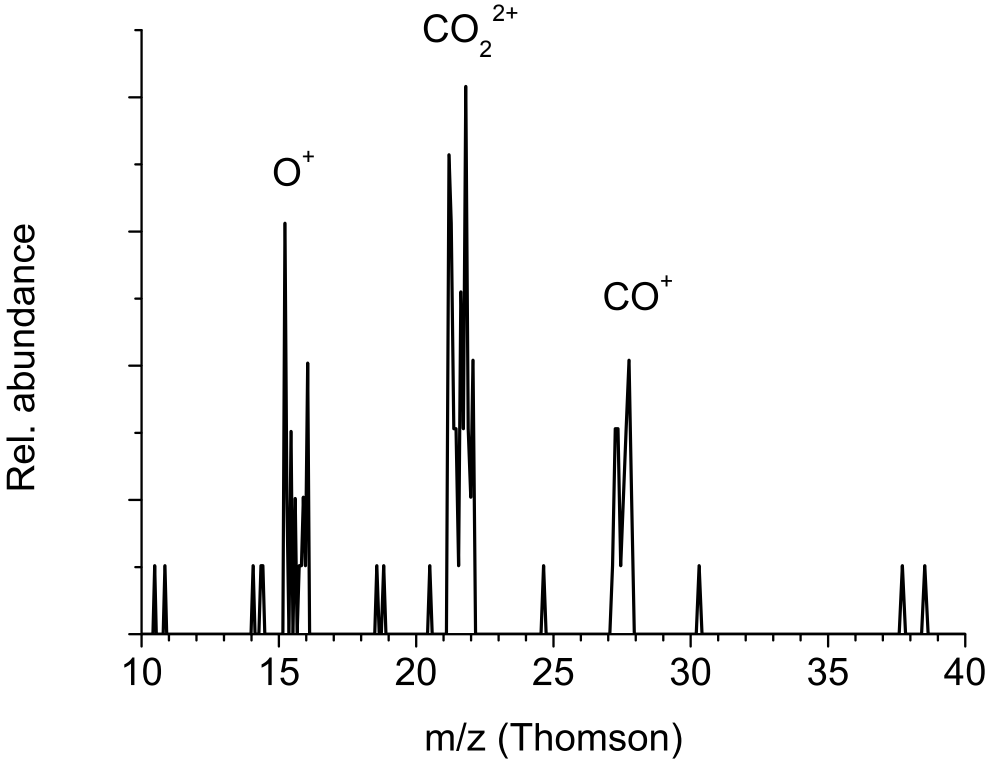

Fig. 2. Secondary ion mass spectrum for the interaction of doubly charged ion CO_2^{2+} with carbon tile from Tore Supra at a collision energy of 10 eV.

The collision energy dependence of intact parent and product ions is summarized in an Energy Resolved Mass Spectrum (ERMS) shown in Fig. 2. We observed only two product ions i.e., CO^+ and O^+ (see Fig. 3). The ion CO^+ has a slightly higher intensity as compared to O^+ and this effect appears to be increasing with collision energy greater than 10 eV. The breakup of CO_2^{2+} starts at about 5 eV collision energy. The above threshold for both product ions and the rather low threshold value (as compared for instance with 29 eV for surface-induced dissociation of H_3^+, see contribution of same conference) is on the one hand indicating that the undergoing reaction is very likely endothermic reaction. However, on the other hand with a rather low endothermicity. Assuming an energy transfer of about 10 % gives an upper limit of about 0.5 eV for this value. This nicely coincides with the relative binding energy of the metastable ground state of CO_2^{2+} ion. Thus likely undergoing dissociation mechanism for the product ions observed is the direct coulomb explosion of the CO_2^{2+} ion after transfer of enough energy to overcome the coulomb barrier. This obviously leads to a large amount of energy released to the two reacting singly charged product ions. The lighter ion O^+ receiving more energy than the heavier ion CO^+ and therefore likely being more discriminated against in the detection process than CO^+ and therefore slowing a slightly more abundance.

It is interesting to point out that partial neutralization to CO_2^+ is not observed in the present case. Neither is the production of doubly charged product ions such as O^{2+} and CO^{2+}.

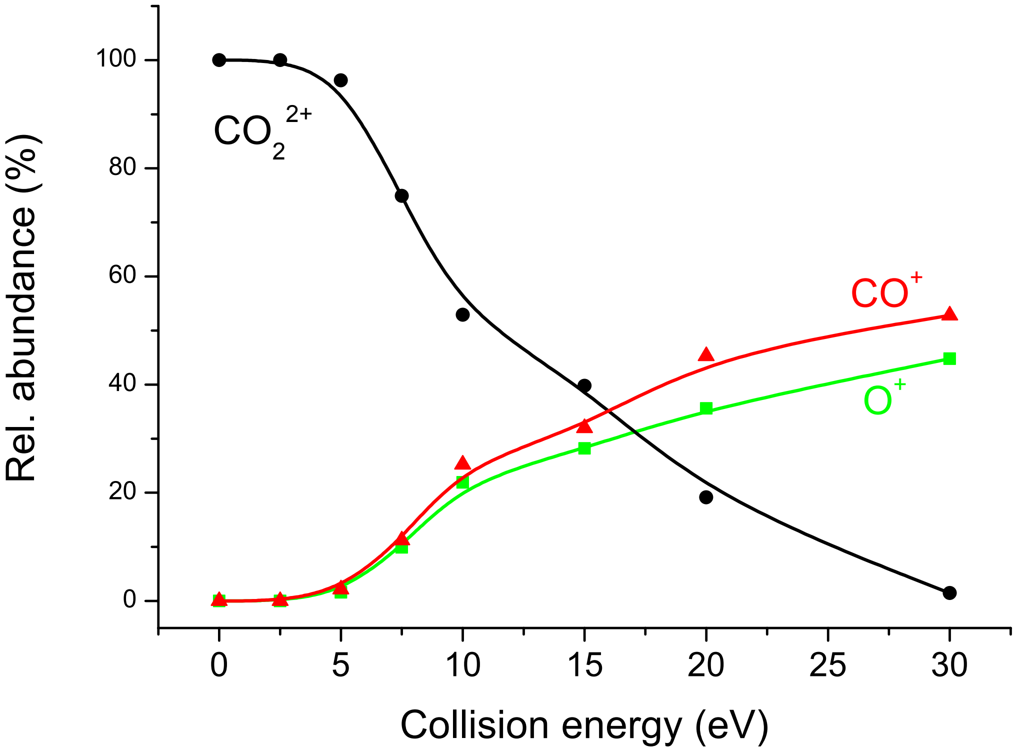

Fig. 2. Energy resolved mass spectrum after impact of CO_2^{2+} with a graphite surface.

This work has been supported by the FWF and ÖAW, Wien, Austria and the European Commission, Brussels.

References

---

[1] M. D. Mabud, M. j. Dekrey, R. G. Cooks, *Int. J. Mass Spectrom. Ion Process* **69** (1986) 277.
[2] B. Brehm, U. Frobe and H. P. Neitzke, *Int. J. Mass Spectrom. Ion Process* **57** (1984) 91.
[3] A. P. Hitchcock, C. E. Brion and M. J. Van der Weil, *J. Chem. Phys.* **45** (1980) 461.
[4] W. J. Griffiths and F. M. Harris, *Int. J. Mass Spectrom. Ion Process* **87** (1989) 349.
[5] S. D. Price, S. A. Rogers and S. R. Leone, *J. Chem. Phys.* **98** (1993) 9455.
[6] C. Mair, T. Fiegele, F. Biasioli, J. H. Futrell, R. Wörgötter, V. Grill, M. Lezius and T. D. Märk, *Plasma Source Sci. Technol.* **8** (1999) 1.

Flow Technique Study of Ion/molecule Reactions of CH_2OH^+ and CH_3CHOH^+ Ions with Ethanol at 1 Torr He Pressure.

P.S. Vinogradov and A.S. Misharin

Institute for Energy Problems of Chemical Physics, Russian Academy of Science.
Leninsky Prospect 38, bldg. 2, Moscow ,117829 Russia [*]

Abstract

A reaction of Xe^+ ion with ethanol and subsequent transformations of the product ions were studied A kinetic scheme describing the evolution of the ionic composition has been determined. The rate constants of the key reactions involved in the scheme have been evaluated. A competition of a low exoergic charge transfer with an association process was detected. The competition takes place due to a long lifetime of the collisional complex with respect to a reactive and reverse decay. A model describing an evolution of the collisional complex has been suggested.

Introduction

An interest to kinetics of ion/molecule reactions (IMR) is related with their importance in physics and chemistry of ionized gas. The data on IMR kinetics is important for the methods of analytic mass spectrometry in which ions are produced in the region with a high pressure (chemical ionization and atmospheric pressure ionization. When ions are produced by a bombardment of the surface by particles with high energy (SIMS, FAB methods) or by an intensive laser pulse (MALDI) the formation of the ionic composition takes place at a high density of particles, so the detected mass spectra may be affected by IMR.

The detailed information on reactivity in ionic systems can be obtained for simple organic particles using modern methods of kinetic mass spectrometry. The knowledge may be a basis for understanding details of the processes in more complicated systems.

The main goal of the present work is to study at what stage of ionic transformations a competition of particle rearrangement in ion complexes with the association processes may take place. Xe^+ + ethanol system is a simple example when a detailed information on the ionic transformations can be obtained.

Experimental

The experiments were carried out using the flow technique reactor apparatus described elsewhere [1]. Primary Xe^+ ions were produced in the ionizer by an electron impact. The neutral adduct (ethanol) was admixed to the flow via a capillary downstream. The concentration of ethanol was a varied kinetic parameter. The length of the reaction region L was defined by the distance between the edge of the capillary and the orifice in the first sampling cone. The calculated value of the effective time of reaction was equal to $0.91\ 10^{-3}$ s.

Results

Kinetic dependences of relative ion currents versus the product $[C_2H_5OH]t$ are presented in Fig.1 and Fig. 2. The products of reaction of Xe^+ ion with ethanol are protonated formaldehyde (CH_2OH^+, 75%, i_{31}) and protonated acetaldehyde (CH_3CHOH^+, 25%, i_{45}). The

---

[*] E-mail address for contacts pavel@chph.ras.ru and misharin@chph.ras.ru

product of the reaction of CH_2OH^+ with ethanol is protonated ethanol ($C_2H_5OHH^+$, i_{47}). In subsequent reactions the protonated dimer ($(C_2H_5OH)_2H^+$, i_{93}) and termer ($(C_2H_5OH)_3H^+$, i_{139}) are produced. The reaction of the other product has the association and proton transfer channels. A competition of the channels was also observed for the ternary product (CH_3CHOH^+ C_2H_5OH, i_{91}). The scheme of the main pathways of ionic transformations is shown in Fig. 3.

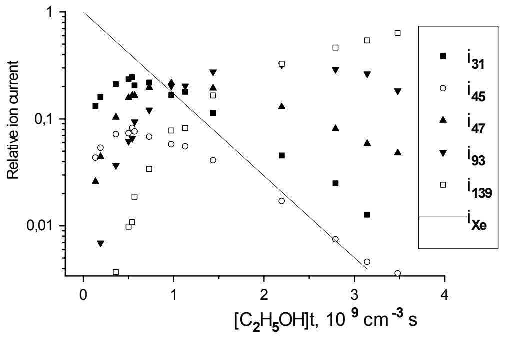

Fig.1. The kinetic dependences of the most abundant ions in mass spectra.

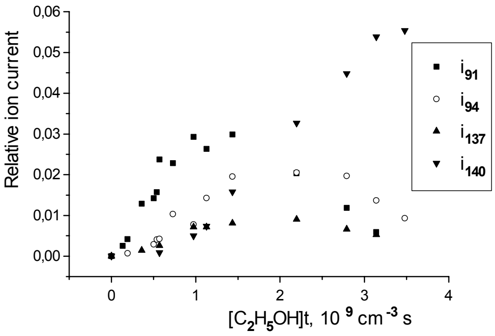

Fig.2. The kinetic dependences of ~~the~~ some of the small ionic constituents. i_{140} is the current of protonated termer of ethanol with one ^{13}C.

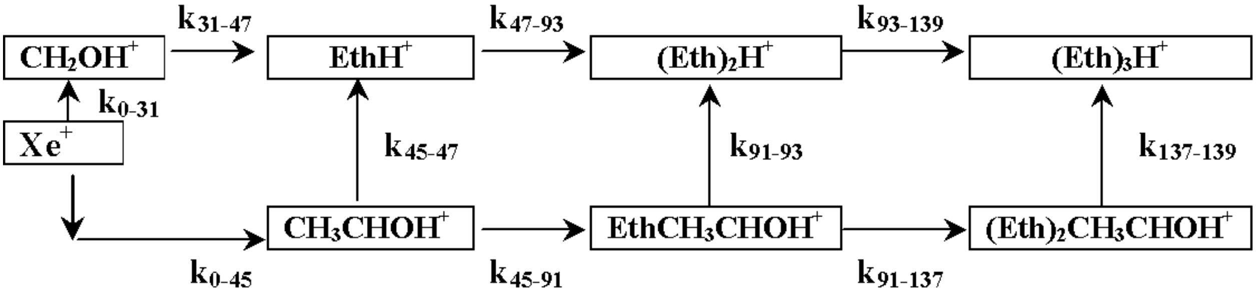

Fig. 3. The scheme of ionic transformations in Xe^+ + ethanol system

The absence of discriminations allowed ~~a~~ careful treatment of the kinetic dependences. The values of rate constants were determined from the fitting procedure. Expressions for ion currents were obtained from the solutions of differential equations of chemical kinetics for ionic concentrations in accordance with the given above scheme. The expressions were taken as fitting functions for the experimental dependences of ion currents. The rate constants were optimized parameters. In each procedure not more than two rate constants were determined. While fitting the dependences for the tertiary ions and the ions of the fourth generation the values of the rate constants determined in the previous fitting sessions for the primary and secondary ions were used. The results are shown in Table 1.

Discussion

The reaction of Xe^+ with ethanol is a fast reaction and its rate constant practically equals to that for collisions of the particles. Molecular ions are not produced in the reaction. It indicates that the charge transfer takes place at large distances. In the present case the intersection of the term of reactants (Xe^+ + CH_3CH_2OH) takes place with highly excited terms of products (Xe + $CH_3CH_2OH^{+*}$) and the excitation energy of the product is higher than the dissociation threshold.

Table 1.

Rate constants of ion/molecule reactions in Xe^++ethanol system at 1 Torr pressure of He

	Reaction		k, 10^{-9} cm^3/s *
1	$Xe^+ + CH_3CH_2OH$	$\rightarrow$products	1.39±0.19
1a		$\rightarrow CH_3CHOH^+ + Xe + H$	0.35±0.05
1b		$\rightarrow CH_2OH^+ + Xe + CH_3$	1.04±0.14
2	(+He)	$\rightarrow$products	1.75±0.52
2a	$CH_3CHOH^+ + CH_3CH_2OH$	$\rightarrow CH_3CHOH^+ CH_3CH_2OH$	0.7±0.16
2b		$\rightarrow CH_3CH_2OHH^+ + CH_3CHO$	1.05±0.36
3	(+He)	$\rightarrow$products	1.18±0.51
3a	$CH_3CHOH^+ CH_3CH_2OH + Eth$	$\rightarrow CH_3CHOH^+ (CH_3CH_2OH)_2$	0.60±0.21 0.58±0.39
3b		$\rightarrow H^+(CH_3CH_2OH)_2 + CH_3CHO$	
4	$CH_3CHOH^+(CH_3CH_2OH)_2 + Eth$	$\rightarrow H^+(CH_3CH_2OH)_3 + CH_3CHO$	1.51±0.4
5	$CH_2OH^+ + CH_3CH_2OH$	$\rightarrow CH_3CH_2OHH^+ + CH_2O$	1.75±0.26
6	$CH_3CH_2OHH^+$+Eth +(He)	$\rightarrow (CH_3CH_2OH)_2H^+$	1.51±0.33
7	$(CH_3CH_2OH)_2H^+$ +Eth +(He)	$\rightarrow (CH_3CH_2OH)_3H^+$	0.77±0,17

* For termolecular association reactions the value of an "effective" binary rate coefficient is given.

The structures of the products of the reaction are ascribed to the protonated formaldehyde (CH_2OH^+) and protonated acetaldehyde (CH_3CHOH^+). A behavior of the kinetic dependence for the $C_2H_5O^+$ ions shows that there is no fraction of the ions with a different reactivity, which may correspond to the CH_2CHOHH^+ structure

An competition of a rather fast exoergic proton transfer reaction with the association process (at 1 Torr pressure of He) is not typical for ion/molecule reactions. The rate constant of loss of the protonated acetaldehyde in both channels is 1.75 10^{-9} cm^3/s and is close to the rate constant of collisions (1.91 10^{-9} cm^3/s [2]).

The rate constant of the proton transfer in the bath gas is smaller than that measured at a low pressure [3, 4]. Even at a low pressure the rate constant of the proton transfer is noticeably less (by 40%) than the rate constant of collisions. It may be due to a low exothermicity (1.9 kcal/mole [5]) of the reaction. At a long enough lifetime of the collisional complex (in the present case it really takes place, as the efficiency of the association is rather high) the energy relaxation process due to collisions with He may affect the rate of the proton transfer.

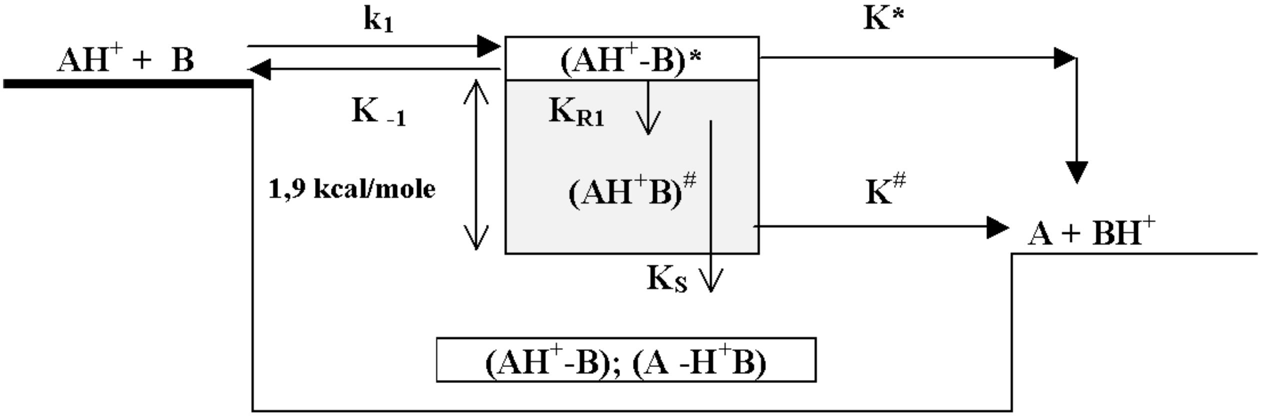

Fig. 4. A scheme of an evolution of the collisional $[CH_3CHOH^+C_2H_5OH]^*$ complex ($(AH^+\text{-}B)^*$) which involves a reverse and reactive decay, a production of $(AH^+\text{-}B)^\#$ complex due to a relaxation process (K_{R1}). For $(AH^+\text{-}B)^\#$ complex only relaxation (K_S) and reactive decay processes are thermochemically allowed.

A model describing an evolution of the collisional complex which involves the energy relaxation processes was suggested (see Fig.4). The model assumes that after the formation the collisional complex **$(AH^+\text{-}B)^*$** it may undergo a reverse or a reactive decay (with the rate coefficients **K_{-1}** and **K^*** respectively) or reduce its energy in collisions with He atoms (**K_{R1}** =

$\mathbf{k_{C1}[He]}$) producing the $\mathbf{(AH^+\text{-}B)^\#}$ complex. It is assumed that the $\mathbf{(AH^+\text{-}B)^\#}$ may undergo only a reactive decay or be stabilized by collisions with He forming the stable association products with the rate coefficients $\mathbf{K^\#}$ and $\mathbf{K_S = k_{C2}[He]}$ respectively. The basic assumptions of the model are:

The model assumes only "weak" deactivating collisions of the $\mathbf{(AH^+\text{-}B)^*}$ complex, i.e. the loss of the energy is less than 1.9 kcal/mole per a collision.

The model neglects the collisional activation of the $\mathbf{(AH^+\text{-}B)^\#}$ complex.

The rate of a reverse decay of the $\mathbf{(AH^+\text{-}B)^\#}$ complex is assumed negligibly low.

Two latter assumptions are made to present the model in an explicit way. A careful consideration can be made using sophisticated statistical approaches.

An application of the "steady state concentrations" method to the mentioned above scheme allowed to find the following relations between the rate coefficients:

$$\mathbf{K_{R1}/K^* = (k_1 / k_{-1(He)})(k_1 - k_{PT0}) / k_{PT0} - (k_1 / k_{PT0}) = 5{,}52}$$

$$\mathbf{K_S/K^\# = 1/\left[\frac{k_1}{k_A}\left(1 - \frac{k_{-1(He)}}{k_1 - k_{PT0}}\right) - 1\right] = 0{,}91},$$

where $\mathbf{k_1}$ is the calculated collisional rate constant, $\mathbf{k_{PT0}}$ is the rate constant of the proton transfer at a low pressure (taken from literature data), $\mathbf{k_A}$ is the rate constant of the association channel (measured in the present work at pressure of He buffer 1 Torr), $\mathbf{k_{-1(He)}} = \mathbf{k_1} - \mathbf{k_{45}}$, $\mathbf{k_{45}}$ is the rate constant of the total loss of $\mathbf{CH_3CHOH^+}$ in the proton transfer and the association channels (measured in the present work).

If the values of $\mathbf{K^*}$ and $\mathbf{K^\#}$ are assumed to be close the ratio of $\mathbf{K_{R1}}$ and $\mathbf{K_S}$ is about 6. The following interpretation of the result may be given. The transformation of the $\mathbf{(AH^+\text{-}B)^*}$ complex to the $\mathbf{(AH^+\text{-}B)^\#}$ state requires the dissipating of not large amount of energy. It may take place after one or a few collisions with He. The subsequent stabilization of $\mathbf{(AH^+\text{-}B)^\#}$ requires the loss of the energy equal to 1.9 kcal/mole and it takes place after a larger number of collisions. It may be shown that the portion of energy of the excessive excitation of the $[\mathbf{CH_3CHOH^+C_2H_5OH}]^*$ complex removed in each collision with He is about 25 meV or even less, so the assumption of "weak" deactivating collisions is valid.

The production of some amount of $\mathbf{CH_3CHOH^+(C_2H_5OH)_2}$ cluster indicates that the complicated exoergic rearrangement of particles (proton transfer, formation of the protonated dimer, switching of acetaldehyde) may also compete with the association process.

References

---

[1] P.S. Vinogradov, O.V. Dmitriev., *Khimiya Visokih Energiy* **24**, 483, 1990

[2] T. Su and M.T. Bowers., Gas Phase Ion Chemistry, Vol. 1., p.84, Academic Press, N.Y.-San Francisco-London (1979)

[3] L.W. Sieck, F.P. Abramson and J.H. Futrell, *J. Chem. Phys.* **45**, 2859 (1966)

[4] T.B. McMahon and J.L. Beauchamp, *J. Phys. Chem.* **81** 593(1977)

[5] E.P. Hunter, S.G. Lias, *J. Phys. Chem. Ref. Data* **27**, No 3, 413 656 (1998)

Measurements of Acetone Yields from the OH-initiated Oxidation of Terpenes by Proton-Transfer-Reaction Mass Spectrometry

Armin Wisthaler, and Werner Lindinger

Institut fürIonenphysik der Leopold-Franzens-Universität, Innsbruck, Austria

Niels R. Jensen, Richard Winterhalter, and Jens Hjorth

Environment Institute, Joint Research Centre, European Commission, Ispra, Italy

Introduction

Biogenic VOCs (Volatile Organic Compounds) are known to be emitted in large quantities from vegetation (1150 Tg C yr^{-1} globally [1] exceeding largely global emissions of anthropogenic VOCs [2]. Monoterpenes ($C_{10}H_{16}$) are important constituents of biogenic VOC emissions. The atmospheric oxidation of monoterpenes appears to be a potentially relevant source of acetone in the atmosphere. Acetone is present as a significant trace gas in the whole troposphere and influences in particular the atmospheric chemistry in the upper troposphere by substantially contributing to the formation of HO_x radicals and peroxyacetyl nitrate (PAN) [3]. Acetone is formed promptly, following attack by the OH-radical on the terpene, via a series of highly unstable radical intermediates. Several previous studies have quantified the prompt formation of acetone from the OH-oxidation of α-pinene and β-pinene [4]. Acetone is, however, also formed slowly via the degradation of stable non-radical intermediates such as pinonaldehyde and nopinone. In order to investigate the relative importance of these processes, the OH-initiated oxidation of α-pinene and β-pinene was investigated in a chamber study, where the concentrations of monoterpenes, acetone, pinonaldehyde and nopinone were monitored by Proton-Transfer-Reaction Mass Spectrometry (PTR-MS).

Experimental

The experiments were carried out in a 480 L Teflon coated reaction chamber made of glass and surrounded by 18 UV/VIS lamps ($\lambda \geq 300$ nm) to simulate sunlight. OH radicals were produced by the photolysis of CH_3ONO in the presence of NO at $\lambda \geq 300$ nm. The experiments were performed in zero air (750 ± 10 Torr; 297 ± 3 K). The mass spectrometer was connected to the reaction chamber through a heated fused silica tube. The analytical technique applied was PTR-MS which has been thoroughly reviewed elsewhere [5, 6]. Mass spectral data of α-pinene, β-pinene, acetone, pinonaldehyde and nopinone were obtained by adding the respective compounds to the reaction chamber filled with zero air (m/z; rel. intensity >1): α-pinene: 138^+(11), 137^+(100), 82^+(6), 81^+(89); β-pinene: 138^+(11), 137^+(100), 82^+(6.5), 81^+(100); acetone 60^+(3.5), 59^+(100); nopinone: 140^+(10), 139^+(100), 122^+(1), 121^+(10), 93^+(1), 83^+(3); pinonaldehyde: 170^+(1), 169^+(12), 152^+(11), 151^+(100), 123^+(9), 109^+(9), 108^+(5.5), 107^+(65.5), 99^+(8), 81^+(10), 72^+(1), 71^+(33), 43^+(9). PTR-MS sensitivity values were calculated using the procedure outlined in detail in [5, 6]. To obtain primary product yields the measured volume mixing ratios of acetone, pinonaldehyde and nopinone were corrected for wall losses/wall release, photolysis and further removal by reaction with OH radicals [7].

Results and Discussion

α-pinene + OH:

Fig. 1 shows typical variations of products and reactants as a function of time for the reaction between α-pinene and the OH radical in the presence of NO_x measured during the first 60 minutes after starting irradiation. A large production of pinonaldehyde and acetone was observed the first 10 min and after 15 min most of the α-pinene was consumed.

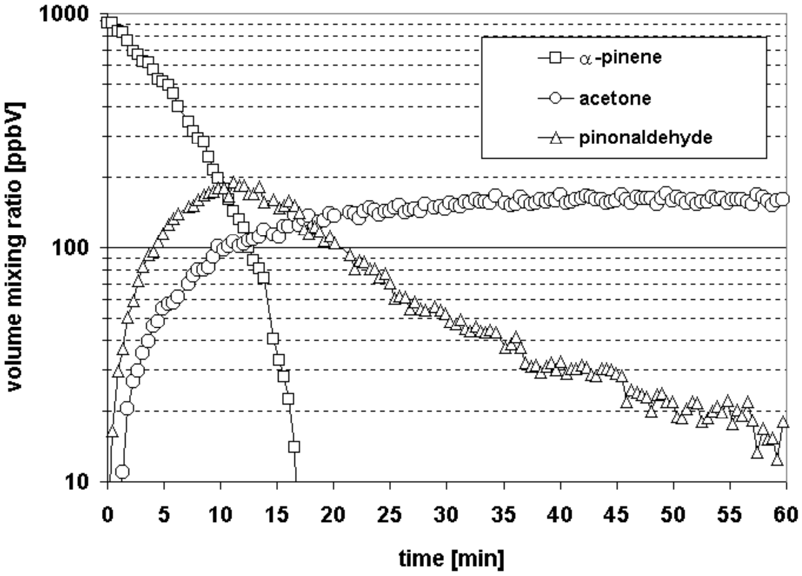

Fig. 1 Variations of products and reactants from the reaction between α-pinene and the OH radical as a function of time

The measured yields of acetone and pinonaldehyde from the reaction between α-pinene and the OH radical are shown in Fig. 2. During the initial phase of the reaction, the concentrations of acetone and pinonaldehyde were found to increase proportionally to the consumption of α-pinene. The yield of acetone was found to be 11 ± 2 % and that of pinonaldehyde was 34 ± 9 % on a molar basis (one σ uncertainty, 3 experimental runs).

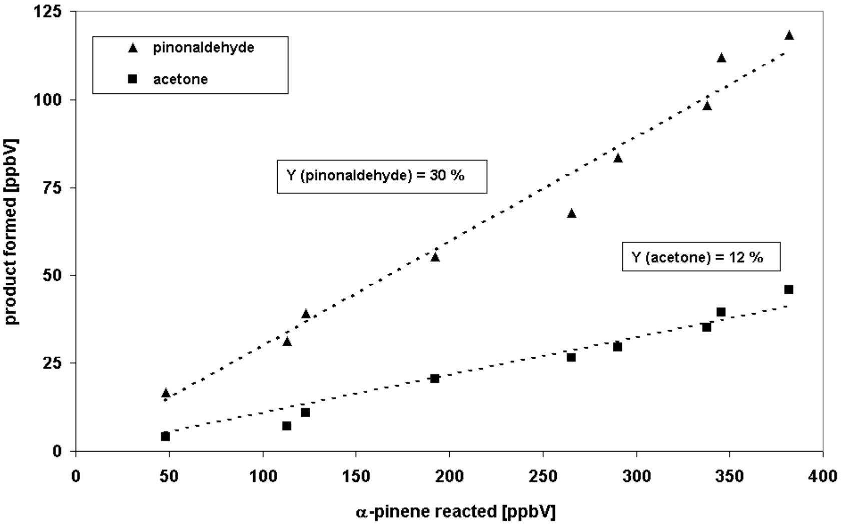

Fig. 2 Primary yields of acetone and pinonaldehyde from the reaction between α-pinene and OH radicals

In Fig. 3 it can be seen, that after all α-pinene had reacted, an additional formation of acetone was observed. The total amount of acetone formed after 60 min of irradiation was 15 ± 2 % (one σ) of the total α-pinene reacted.

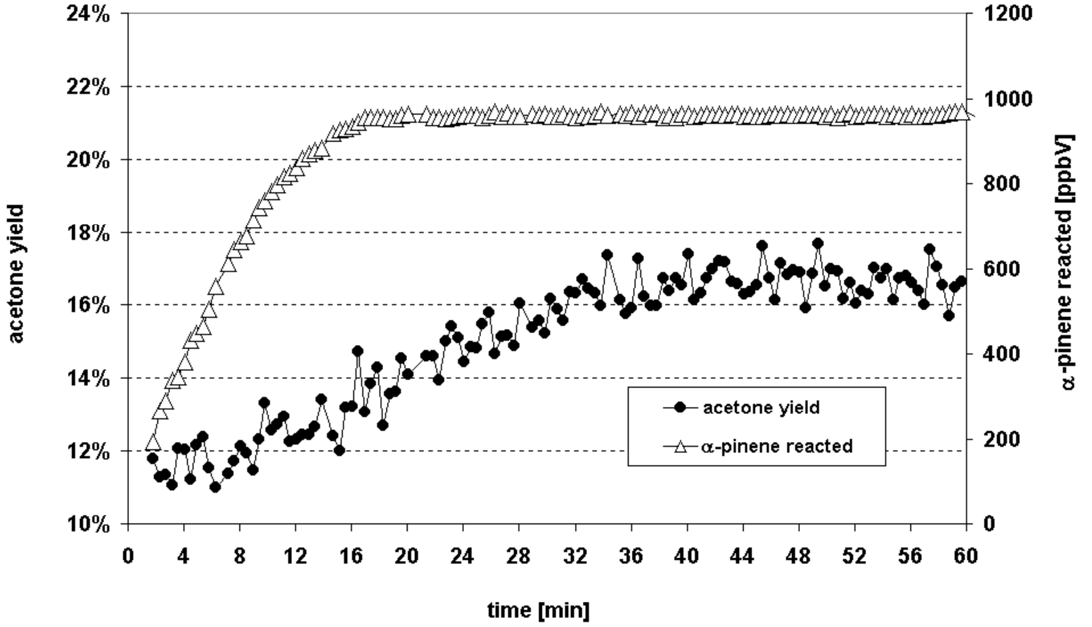

Fig. 3 Acetone yield and consumed α-pinene as a function of time

The secondary acetone yield is thus 4 % of the α-pinene consumed. With the primary pinonaldehyde yield of 34 ± 9 % an upper limit (other intermediates may also form acetone) of 12 ± 3 % for the acetone molar yield from the oxidation of pinonaldehyde can be established.

β-pinene + OH:

A large production of nopinone and acetone was observed during the first 15 minutes in which ≥ 90% of the β-pinene was consumed. The measured primary yields of acetone and nopinone from the reaction between β-pinene and the OH radical were 13 ± 2 % (one σ uncertainty, 8 experimental runs) and 25 ± 3 % on a molar basis (one σ uncertainty, 4 experimental runs). After all β-pinene had been consumed, an additional formation of acetone was observed. The total amount of acetone formed after 60 min of irradiation was 16 ± 2 % (one σ) of the total β-pinene reacted. The secondary acetone yield is thus 3 % of the β-pinene consumed. With the primary nopinone yield of 25 ± 3 % an upper limit (other intermediates may also form acetone) of 12 ± 2 % for the acetone molar yield from the oxidation of nopinone can be established

Atmospheric implications

The present study shows that significant amounts of acetone are formed directly, when α-pinene and β-pinene are oxidized by the OH radical, but also secondary chemistry (degradation of primary reaction products) gives a significant contribution to the formation of acetone from monoterpenes. It can be concluded that atmospheric oxidation of monoterpenes contributes a significant fraction to the global acetone source strength. A secondary biogenic source of acetone from the oxidation of monoterpenes of 11-13 Tg yr^{-1} (~15–25 % of the global acetone source strength) has been estimated assuming an acetone formation of 8.5 – 11.5 % from monoterpene oxidation [3] [8]. The investigation presented here suggests that these estimates may be somewhat (3–4 %) too low, because they only include the primary yield of acetone from monoterpenes and not secondary acetone formation from other primary oxidation products, which we have shown to produce significant amounts of acetone.

References

[1] Guenther, A., Hewitt, C. N., Ericson, D., Fall, R., Geron, C., Graedel, T., Harley, P., Klinger, L, Lerdau, M., Journal of Geophysical Research, 100, 8873-8892, 1995.

[2] Middleton, P., in *Composition, Chemistry, and Climate of the Atmosphere*, ed. by H. B. Singh, Van Nostrand Reinhold, New York, pp. 88-129, 1995.

[3] Singh, H., Chen, Y., Tabazadeh, A., Fukui, Y., Bey, I., Yantosca, R., Jacob, D., Arnold, F.,Wohlfrom, K., Atlas, E., Flocke, F., Blake, D., Blake, N., Heikes, B., Snow, J., Talbot, R., Gregory, G., Sachse, G., Vay, S., Kondo, Y., Journal of Geophysical Research, 105, 3795-3805, 2000; and Refs. therein.

[4] Orlando, J. J., Noziere, B., Tyndall, G. S., Orzechowska, G. E., Paulson, S. E., Rudich, Y., Journal of Geophysical Research, 105, 11561-11572, 2000; and Refs. therein.

[5] Lindinger, W., Hansel, A., Jordan, A., Chemical Society Reviews, 27, 347-354, 1998a.

[6] Lindinger, W., Hansel, A., Jordan, A., International Journal of Mass Spectrometry and Ion Processes, 173, 191-241, 1998b.

[7] Nozière, B., Barnes, I., Becker, K.-H., Journal of Geophysical Research, 104, 23645-23656, 1999.

[8] Reissell, A., Harry, Ch., Aschmann, S. H., Atkinson, R., Arey, J., Journal of Geophysical Research, 104, 13868-13879, 1999.

A Semi-Empirical Concept for the Calculation of Electron-Impact Ionization Cross Sections of Neutral and Ionized Fullerenes

H. Deutsch[1], P. Scheier[2], K. Becker[3], and T.D. Märk[2]

[1] *Institut für Physik, Ernst-Moritz-Arndt Universität, D-17487 Greifswald, Germany*
[2] *Institut für Ionenphysik, Leopold-Franzens Universität, A-6020 Innsbruck, Austria*
[3] *Department of Physics, Stevens Institute of Technology, Hoboken, NJ 07030, USA*

Abstract

We have developed a semi-empirical approach to the calculation of cross section functions (absolute value and energy dependence) for the electron-impact ionization of several neutral and ionized fullerenes C_{60}^{n+} (n = 0-3), for which reliable experimental data have been reported. In particular, we propose a modification of the simplistic assumption that the ionization cross section of a cluster/fullerene is given as the product of the monomer ionization cross section and a factor m^a, where "m" is the number of monomers in the ensemble and "a" is a constant. A comparison between our calculations and the available experimental data reveals good agreement for n = 0,1,3. In the case of the ionization of C_{60}^{2+} (n = 2) our calculation lies significantly below the measured cross section which we interpret as an indication that additional indirect ionization processes are present for this charge state.

Introduction

Electron-impact ionization cross section functions have been measured for nearly 100 molecules including free radicals, clusters, and fullerenes [1]. Calculation of absolute total single ionization cross sections for most molecules and their energy dependence using semi-rigorous methods such as the BEB method of Kim and co-workers [2,3] and the DM formalism [4] reveal reasonably good agreement (to within 20%) between measured and calculated data for the vast majority of molecules. Even in cases such as the fluorine containing free radicals CF_x and NF_x (x = 1-3), where earlier calculations revealed a significant disagreement between measured and calculated cross sections of up to a factor 2, the same 20% level of agreement has been achieved recently using a modified BEB approach [5].

The situation is distinctly different for clusters and fullerenes. Several theoretical models have been applied to the quantitative characterization of the ionization properties of clusters and fullerenes, i.e. to the calculation of their absolute ionization cross sections (see e.g. Deutsch et al. [6,7]). The various theoretical approaches (see also the more detailed discussion below) result in different absolute ionization cross sections both in terms of the absolute value and the cross section shape as a function of electron impact energy for a given target. However, none of the methods appears to succeed in reproducing the experimental data that are available for a few targets. In this context, we will not distinguish between "clusters" and "fullerenes". Both will be considered "ensembles of monomers" encompassing a large number of constituents and geometrical structures ranging from a hard sphere packing arrangement to a hollow cage structure.

In this paper, we introduce a semi-empirical approach to the calculation of cross section functions (absolute value and energy dependence) for the electron-impact ionization of several neutral and ionized fullerenes C_{60}^{n+} (n = 0-3), for which reliable experimental data have been reported. In particular, we want to test for these selected cases to what extent, if at all, the assumption holds that the ionization cross section of a cluster/fullerene is given as the product of the monomer ionization cross section and a factor m^a, where “m” is the number of monomers in the ensemble and “a” is a constant.

Results and Discussion

We derived a semi-empirical approach to the calculation of cross section functions (absolute value and energy dependence) for the electron-impact ionization of several neutral and ionized fullerenes C_{60}^{n+} (n = 0-3), for which reliable experimental data have been reported [8,9]. Our new method is based on a modified additivity rule

$$\sigma_{tot}(X_m) = m^{2\alpha} \cdot \sigma_{tot}(X) \tag{1}$$

and incorporates *ad hoc* two factors, a structure factor e^{-b} and an energy-dependent factor $F_{cage}(E)$.

$$\sigma_{tot}(X_m, E) = m^{2a} \cdot e^{-b} \cdot \sigma_{tot}(X, E^*) \cdot F_{cage}(E) \tag{2}$$

The influence of the low energy dependence F(E) on the cross sections can be realized by introducing an energy shift

$$E^* = E - \left[E_0 + \left(IP_{cluster-ion} - IP_{monomer}\right)\right] \tag{3}$$

where E^* denotes the effective energy of the primary electron within the cluster/fullerene, E is the kinetic energy of the primary electron, and E_0 the energy loss due to inelastic scattering. In the present work a constant value of 5 eV was used for E_0. The appropriate values for the ionization potentials (IPs) can be found in Refs. [9] and [10].

Our model allows us to predict the experimentally determined absolute cross section values and the cross section shapes for a variety of fullerene ionization processes. A comparison between our calculations and the available experimental data for C_{60}^{n+} (n= 0-3) reveals good agreement for n = 0,1,3, but indicates that additional indirect ionization processes are present in the case of n = 2 (see Figures 1-4).

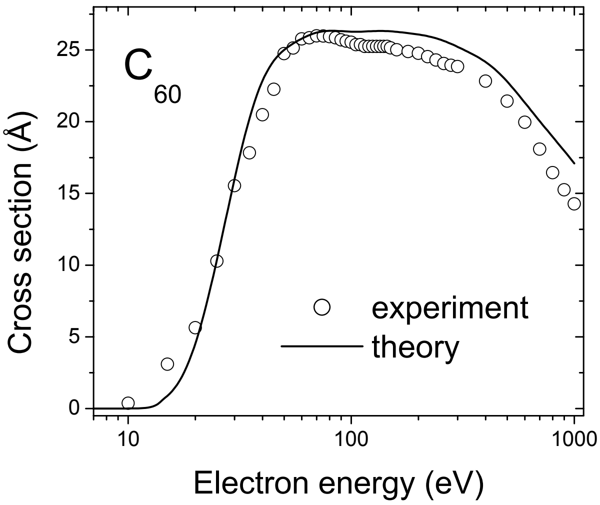

Fig. 1 Cross section for the formation of C_{60}^+ ions following electron impact single ionization of C_{60}. The experimental data (open circles) are from Ref. [8], the solid line represents the present calculation.

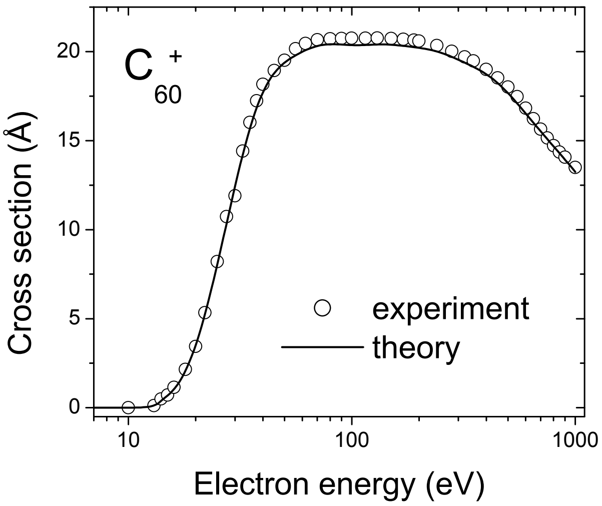

Fig. 2 Cross section for the formation of C_{60}^{2+} ions following electron impact single ionization of C_{60}^+. The experimental data (open circles) are from Ref. [9], the solid line represents the present calculation.

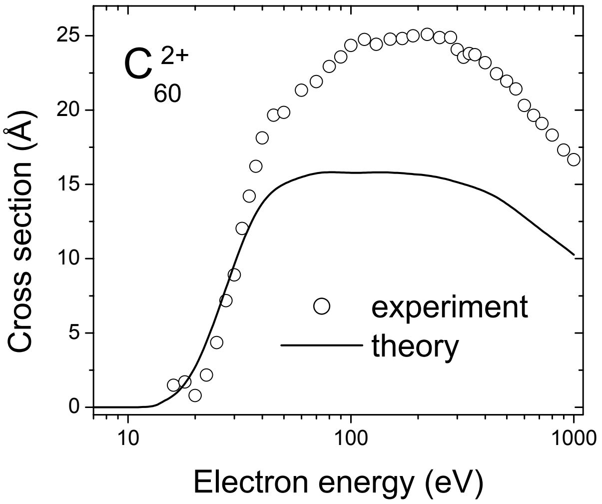

Fig. 3 Cross section for the formation of C_{60}^{3+} ions following electron impact single ionization of C_{60}^{2+}. The experimental data (open circles) are from Ref. [9], the solid line represents the present calculation.

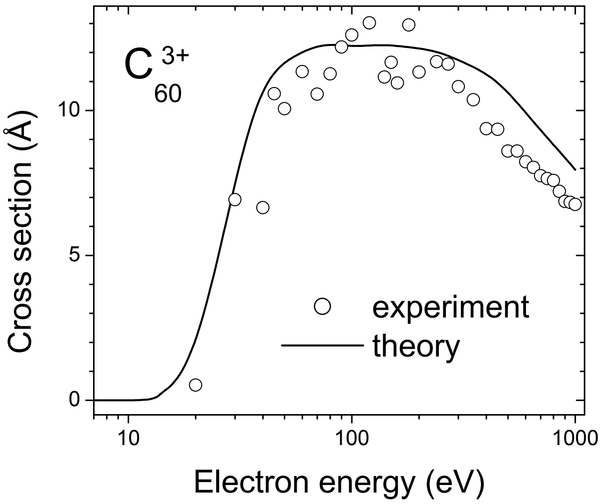

Fig. 4 Cross section for the formation of C_{60}^{4+} ions following electron impact single ionization of C_{60}^{3+}. The experimental data (open circles) are from Ref. [9], the solid line represents the present calculation.

Acknowledgments

This work was partially supported by the Österreichischer Fonds zur Förderung der Wissenschaftlichen Forschung, Wien, Austria and the EU Commission network programme, Brussels. One of us (K.B.) wishes to acknowledge partial financial support from the U.S. National Aeronautics and Space Administration (NASA) through award NAG5-8971.

References

[1] K. Becker, "Electron-Driven Ionization and Dissociation: From Experiments under Single Collision Conditions to Processes in High-Pressure Discharge Plasmas", in Proc. XXII. International Conference on Photonic, Electronic, and Atomic Collisions (ICPEAC), Santa Fe, NM, USA (2001), AIP Press, Woodbury, NY (2002), in press
[2] Y.-K. Kim and M.E. Rudd, Phys. Rev. A 50, 3954 (1994)
[3] W. Hwang Y.-K. Kim, and M.E. Rudd, J. Chem. Phys. 104, 2956 (1996)
[4] H. Deutsch, K. Becker, S. Matt, and T.D. Märk, Int. J. Mass Spectrom. 197, 37 (2000)
[5] W.M. Huo, V. Tarnovsky, and K. Becker, Chem. Phys. Letters, submitted for publication
[6] H. Deutsch, K. Becker, J. Pittner, V. Bonacic-Koutecky, S. Matt and T.D. Märk, *J. Phys. B* **29** (1996) 5175
[7] S. Matt, P. Scheier, T.D. Märk, and K. Becker, "Positive and Negative Ion Formation in Electron Collisions with Fullerenes", in "Novel Aspects of Electron-Molecule Collisions", edited by K. Becker, World Scientific Publishing, Seoul, South Korea (1998), p.1-69
[8] B. Dünser, M. Lezius, P. Scheier, H. Deutsch and T.D. Märk, *Phys. Rev. Lett.* **74** (1995) 3364
[9] R. Völpel, G. Hofmann, M. Steidl, M. Stenke, M. Schlapp, R. Trassl and E. Salzborn, *Phys. Rev. Lett.* **71** (1993) 3439
[10] E. Brook, M.F.A. Harrison and A.C.H. Smith, *J. Phys. B* **11** (1978) 3115

First experimental evidence of an electric dipole-quadrupole interference in the spin polarization of Xe 4p photoelectrons

T. Khalil, B. Schmidtke, M. Drescher, N. Müller and U. Heinzmann

Fakultät für Physik, Universität Bielefeld, D-33615 Bielefeld

We have measured the spin polarization of the Xe(4*p*)$^{-1}$ photoelectrons after ionization by circularly polarized EUV radiation from the helical undulator UE 56 at BESSY II in the photon energy region (150-190 eV) close to the ionisation threshold where a resonance effect due to quadrupole contributions has recently been predicted [1]. The longitudinal spin polarization component under the reaction angle of 90° (angle between the momenta of incoming radiation and outgoing photoelectrons) shows a value significantly different from zero indicating a quadrupole contribution in the order of 3%. This component of spinpolarization has to be zero for pure dipole transitions in this observation geometry. These are the first measurements showing a quadrupole effect in the spin polarization of photoelectrons. The cross comparison between experiment and theoretical prediction demonstrates the high sensitivity of this spin-polarization observable towards multi configuration interactions.

References

---

[1] N. Cherepkov and S. Semenov, *J. Phys. B* **34**, L 211 (2001)

Infrared spectra of the Cl^--H_2, Br^--H_2, and I^--H_2 anion complexes

D.A. Wild, Z.M. Loh, R.L. Wilson, & E.J. Bieske

School of Chemistry, University of Melbourne, Australia

Spectroscopic studies of complexes and clusters provide fundamental information on the interaction between atomic and molecular species [1]. So far, for anion complexes most of the available quantitative structural data have been derived from *ab initio* calculations [2]. Recently we have recorded infrared spectra of several simple complexes consisting of H_2 and D_2 molecules attached to halide anions (Cl^-, Br^-, I^-) that yield empirical structural data for anion-neutral interactions. The spectra, which are the first for negatively charged complexes displaying complete rotational resolution, provide data that should serve to benchmark *ab initio* computational methods for such species.

The spectroscopic studies are carried out in a tandem mass spectrometer. Infrared spectra are obtained by irradiating mass selected X^--H_2 complexes with tunable IR light in H-H stretch region while monitoring X^- fragment ions. The resulting spectra of the three species are shown in Figure1.

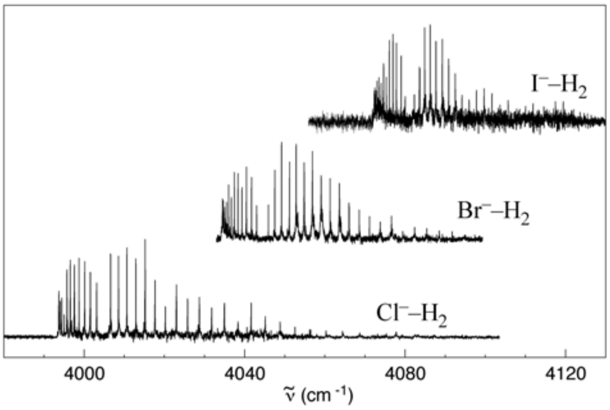

Figure 1: Infrared spectra of Cl^-–H_2, Br^-–H_2, and I^-–H_2 in the region of the H_2 stretch vibration. The spectra are obtained by monitoring production of halide anion photofragments as the infrared frequency is scanned.

The spectra each feature a single Σ–Σ band, containing well resolved P and R branch lines, that is red-shifted from the $Q_1(1)$ transition of the free H_2 molecule (4155 cm^{-1}). The spectra, which are of complexes containing *ortho* H_2, unambiguously demonstrate that the species possess linear equilibrium structures. Intermolecular separations and force constants for the intermolecular bonds are deduced from the rotational and centrifugal distortion constants. As well, radial potential energy curves describing the halide-hydrogen interactions are developed using the spectroscopic data.

Data derived from the spectra are summarised in the table below. Included are vibrational band shifts with respect to the $Q_1(1)$ transition of the free H_2 molecule ($\Delta\nu_o$), separations between the halide anion and the H_2 molecule centre-of-mass (R_{cm}''), and dissociation energies (D_o'').

	Cl^--H_2(*o*)	Br^--H_2(*o*)	I^--H_2(*o*)
ν_o (cm^{-1})	4004.84	4044.46	4081.11
$\Delta\nu_o$ (cm^{-1})	-150.4	-110.8	-74.1
R_{cm}'' (Å)	3.195	3.460	3.851
D_0''	488	365	253

References

[1] D. J. Nesbitt, *Chem. Rev.* 88, 843-70 (1988)
[2] E.J. Bieske and O. Dopfer, *Chem. Rev.*, 100, 3963 (2000)